BOEING

SCIENTIFIC RESEARCH LABORATORIES

CONTRACT NAS 7-489

# Stress Corrosion Cracking of Titanium Alloys: Studies of Cracks in Thin Specimens; SCC of Ti-6Al-4V in Chloride, Iodide and Fluoride Solutions; Stress Corrosion Cracking in Molten Salts; Electrochemistry of Freshly Generated Titanium Surfaces

T.R. Beck, M.J. Blackburn, W.H. Smyrl



THE BOEING COMPANY | AEROSPACE GROUP / SEATTLE, WASHINGTON

# BOEING SCIENTIFIC RESEARCH LABORATORIES

## Seattle, Washington 98124

CONTRACT NAS 7-489

# Stress Corrosion Cracking of Titanium Alloys: Studies of Cracks in Thin Specimens; SCC of Ti-6Al-4V in Chloride, Iodide and Fluoride Solutions; Stress Corrosion Cracking in Molten Salts; Electrochemistry of Freshly Generated Titanium Surfaces

T.R. Beck, M.J. Blackburn, W.H. Smyrl

## MATERIALS & STRUCTURAL SCIENCES LABORATORY

Quarterly Progress Report No. 20

for Period of

April 1 through June 30, 1971

and Summarizing work done from

January 1 through June 30, 1971

THE BOEING COMPANY | AEROSPACE GROUP / SEATTLE, WASHINGTON

CONTRACT NAS 7-489

# Stress Corrosion Cracking of Titanium Alloys: Studies of Cracks in Thin Specimens; SCC of Ti-6Al-4V in Chloride, Iodide and Fluoride Solutions; Stress Corrosion Cracking in Molten Salts; Electrochemistry of Freshly Generated Titanium Surfaces

Quarterly Progress Report No. 20
for Period of
April 1 through June 30, 1971
and Summarizing work done from
January 1 through June 30, 1971

Prepared by

T. R. Beck, M. J. Blackburn and W. H. Smyrl

Materials and Structural Sciences Laboratory

Boeing Scientific Research Laboratories
Seattle, Washington 98124

TABLE OF CONTENTS

## 1.0 SUMMARY

This is the final report to appear under this contract number. Some new data on stress corrosion cracking in acqueous solutions and molten salts and a unified picture of kinetics of new titanium surfaces conducted in the past five years are presented herein. Abstracts of the work in each area are given in each section of the report.

## 2.0 INTRODUCTION

This work describes part of a study of stress corrosion cracking of titanium alloys initiated in July 1965 (1) and continued under NASA sponsorship beginning July, 1966 (2). This is the twentieth Quarterly Report in the series (3, 4, 5, 6, 7, 8, 9, 10, 11, 12, 13, 14, 15, 16, 17, 18, 19, 20, 21) and covers the six-month period of January 1 through June 30, 1971. A short letter report (21) described work in progress in the period of January 1 through March 31, but did not present detailed results.

This is the final report to appear under this contract number. The bulk of the final period was devoted to cleaning up loose ends and preparing manuscripts for publication. Three main topics are presented in this report: 1. New experimental data on stress corrosion cracking in aqueous solutions; 2. Manuscript on first phase of work on stress corrosion cracking in molten salts; 3. Two manuscripts on work on electrochemistry of freshly generated titanium surfaces collected in one place from all the past quarterly reports and interpreted in a unifying perspective.

## 3.0 REFERENCES


1. T. R. Beck, Boeing Document D1-82-0554, July 1966.
2. T. R. Beck and M. J. Blackburn, Research Proposal D1-82-0467, August 1965.
3. T. R. Beck, Contract NAS7-489, Quarterly Progress Report No. 1, September 1966.
4. Ibid, No. 2, January 1967.
5. Ibid, No. 3, April 1967.
6. Ibid, No. 4, July 1967.
7. Ibid, No. 5, October 1967.
8. Ibid, No. 6, January 1968.
9. Ibid, No. 7, April 1968.
10. Ibid, No. 8, July 1968.
11. Ibid, No. 9, October 1968.
12. Ibid, No. 10, January 1969 (short letter report).
13. Ibid, No. 11, April 1969.
14. Ibid, No. 12, July 1969 (short letter report).
15. Ibid, No. 13, October 1969 (short letter report).
16. Ibid, No. 14, January 1970.
17. Ibid, No. 15, April 1970 (short letter report).
18. Ibid, No. 16, July 1970.
19. Ibid, No. 17, October 1970 (short letter report).
20. Ibid, No. 18, January 1971.
21. Ibid, No. 20, April 1971 (short letter report)

# 4.0 TECHNICAL DISCUSSION

## 4.1 Studies of Cracks in Thin Specimens

An attempt has been made to study some aspects of cracks in thin specimens of susceptible alloys utilizing transmission electron microscopy. A susceptible alloy Ti 10% Al was selected for this study and two heat treatment conditions were utilized, water quenched from 975°C to retain an (almost) disordered structure and quenched and aged at 750°C for 48 hours to produce particles of the $\alpha_2$ ($Ti_3$ Al) phase. Thin specimens were produced from these by conventional electropolishing techniques taking care to keep the temperature low enough to prevent hydride formation. These specimens which were thin enough for transmission electron microscopy were then treated in the following manner. The thin sections were immersed in 0.6 M KCl acidified with HCl to a pH ~1.0 under potentiostatic control. The specimen was then perforated with a sharp sapphire point near the thin edge. Such perforation produced cracking of the specimens which in some cases resembled SCC cracks at least during perforation. However on subsequent examination the cracks appeared to be a shear nature and thus may not have grown by a SCC mechanism. However, the cracks did form i.e., exposed fresh surface within an environment which resembled that within a SCC crack. The salient features observed in these experiments are shown in Figures 1, 2 and 3 from which the following points can be made.

- Cracking tended to be transgranular and crystallographic; the plane of cracking could not be measured accurately due to the distortion of foils but appeared to be near the basal $(0002)_\alpha$ plane in some cases. (It is obvious

from figure 2 that this is not true in all cases.)

- A high dislocation density is generated near the cracks and extends to at least the margin of the cracked grain. The dislocation density tends to be higher at the crack surfaces.
- Attempts to show that titanium hydride was present within the slip bands were unsuccessful-- no contrast or, more especially, no selected area diffraction evidence was obtained for hydride formation. In order to investigate regions near the crack surface, specimens which contained the $\alpha_2$ phase were used. Figure 3 shows that using dark field techniques no changes in the particles are observed adjacent to the crack surface even in sheared particles. This at least indicates that if hydride is formed on the fracture surface the layer must be extremely thin (i.e., $\ll 100$ Å).

The above results were obtained at applied potential of -500 mV and a limited number of tests were performed at other potentials. It was found that cathodic potentials -1500 mV resulted in hydride formation although results were erratic in that not all specimens formed hydride. Anodic polarization in acidified iodide solutions resulted in pitting e.g., Figure 4, and selective dissolution of slip bands. However, these effects have not been studied in detail.

These results are perhaps interesting but by no means conclusive. They do indicate that titanium hydride formation resulting from hydrogen absorbtion from aqueous solutions does not occur easily. The techniques will be extended and an attempt made to propagate SCC cracks through pre-

thinned regions although they may not prove feasible. Further attempts will also be made to produce thin foil specimens from actual SCC crack surfaces; previous experience has indicated that this is not easy.

## 4.2 SCC of Ti-6Al-4V in Chloride, Iodide and Fluoride Solutions

### Introduction

In the past quarterly reports the behavior of a number of titanium alloys in a variety of aqueous solutions have been described. The most important commercial alloy Ti-6Al-4V was not included among the alloys tested and complete velocity (V): stress intensity (K) relationships had not been determined under certain conditions. Thus, it was decided to study the behavior of this alloy in chloride, iodide and fluoride solutions at room temperature and fixed potentials.

Experimental The alloy was obtained in the form of 0.2" sheet and was in the mill annealled condition. Two factors contributed to the high degree of susceptibility of thin alloy, its high oxygen content and extreme transverse texture, as can be seen in Figure 5. DCB specimens, 0.2" wide were cut from the sheet in the WR orientation. Stress was applied to such specimens by driving a wedge into the notch and the K calculated from the standard equation for such specimens.

### Results

Aqueous Solutions

The results will be divided into three sections depending on the environment. Limited susceptibility was detected in room air and distilled water as may be seen in Figure 6 which also includes the V:K curves for 0.6 M chloride and 5.0 M iodide under open circuit conditions.

The influence of potential on crack growth rate in 0.6 M KCl is shown in the V:K curves in Figure 7, from which the following points can be made.

- $K_{ISCC}$ varies in a relatively complex way with potential rising with anodic and cathodic potentials. In this very susceptible alloy the variation is not as marked as may be observed in less susceptible material.
- The velocity of cracking at high K levels (region II) increases with potential although the increase is not a simple linear function over the complete potential range. [The variation is not exponential as has been observed in aluminum alloys.]
- The variation of cracking velocity at lower K levels (region IIa) is more complex and does not show a linear increase with potential.

A further observation was that at high anodic potentials ($\geq$1000mV) the crack tended to tunnel and a pale yellow green liquid ($TiOCl_2$ ?) was discharged from the crack. The fractography of material fractured at these high anodic potentials is under study at this time.

Behavior in 5M KI solutions is illustrated in Figure 8 from which it can be seen that a much simpler type of behavior is observed. The crack velocity increases with potential but again the increase is not a simple linear increase with potential (although more nearly so than the chloride results). $K_{ISCC}$ tends to fall with increasing potential but the rate of decrease is small at potentials >0 mV. An additional point of interest is then an apparent region I type behavior is exhibited in

this solution at potentials $\geq$1000 mV. This behavior is observed when the free iodine is generated within the crack. However, crack growth with velocities $<10^{-6}$ cm/sec has not been observed which may indicate a true threshold ($K_{ISCC}$) exists under these conditions or possibly that the iodine is exhausted in the crack. At cathodic potentials (-1500 mV) the V:K curve is displaced below that of distilled water although complete protection is not observed. The low cracking rates ($\sim 10^{-6}$ cm/sec) are the lowest observed in aqueous solution at this time and indicate that it may be possible to obtain very slow subcritical crack growth in alloys apparently immune to SCC in short time tests.

In previous reports it had been concluded that fluoride inhibited crack growth in titanium alloys, at least in concentrations $\sim$0.6 M. This result has been partially confirmed as may be seen in Figure 9, however, it is also evident from this figure that in high concentration (6 M) fluoride acts as an accelerator. The behavior is somewhat complex as the concentrated solution (6 M KF) produces higher velocities and a lower $K_{ISCC}$ than distilled water but lower concentrations produce both lower velocities and higher $K_{ISCC}$ levels. Preliminary potential studies have indicated that cathodic (-1400 mV) and anodic potentials (0 mV) inhibit crack growth in the 6 M KF solution.

The influence of β-heat treatments

It has been shown that acicular structures tend to have better SCC properties than equiaxed structures in α+β type alloys. This has been confirmed in this alloy by reheat treating mill annealled material in the β-phase field before the conventional mill annealling treatment. After these treatments the alloy was tested in 0.6 M KCl at open circuit.

It was found that testing was more difficult due to considerable crack branching with the attendant complexities of K and velocity measurements. However, the following points can be made (based partially on the assumption that crack branching is the result of a velocity plateau independent of the K level). The $K_{ISCC}$ value is increased to ~34 Ksi$\sqrt{in}$ and the velocity of cracking is reduced to $1.4 \times 10^{-3}$ cm/sec as shown in Figure 6. The $K_{IC}$ value (or in this case $K_Q$ as the plane strain criterion is not fulfilled in 0.2 inch material) is increased to ~80 Ksi$\sqrt{in}$ in β-processed material.

Discussion

These results suppliment the data reported previously and in most cases confirm in a more quantitative way that the earlier results were correct. The susceptibility in concentrated fluoride solutions completes a general picture of $K_{ISCC}$ variation which is shown schematically in Figure 10. Velocity variations with potential (and concentration) are more complex and further work is required to evaluate this influence quantitatively-- this will be attempted when the MTK model is modified (as such data will be required). The beneficial influence of acicular structures compared with equiaxed structure was confirmed, both $K_{ISCC}$ being increased and the velocity decreased. The tendency to form branched cracks could result in yet higher $K_{ISCC}$ levels in certain cases. The reason for this improvement is no doubt due to several factors which include a more random texture, a smaller α-plate or grain size and the presence of a thin film of the β-phase (non-susceptible) at the α-phase boundaries.

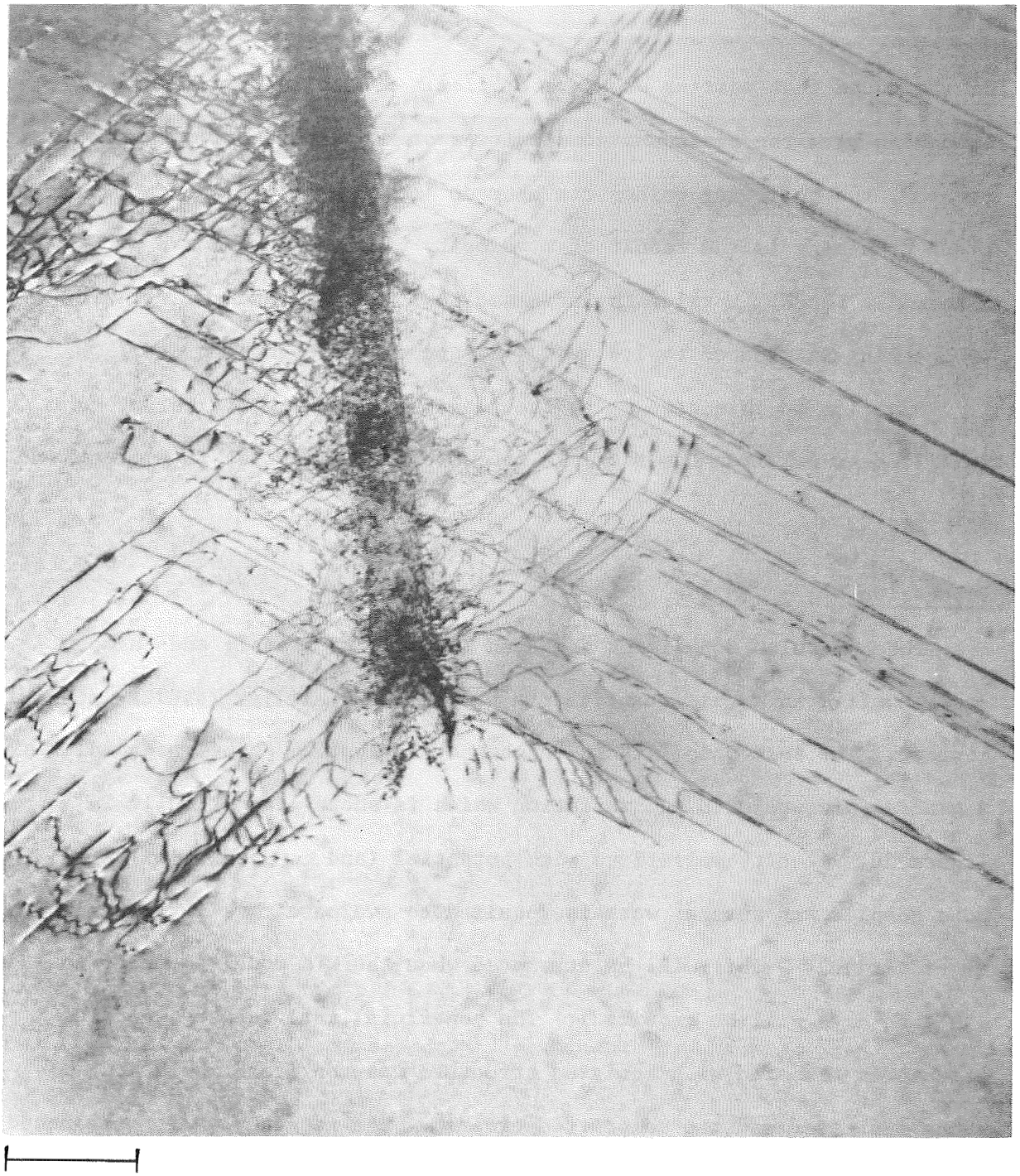

Figure 1

Ti-10% Al (975°C WQ) perforated thin foil showing dislocation distribution near the end of a crack. (Solution:acidified KCl - 500mV)

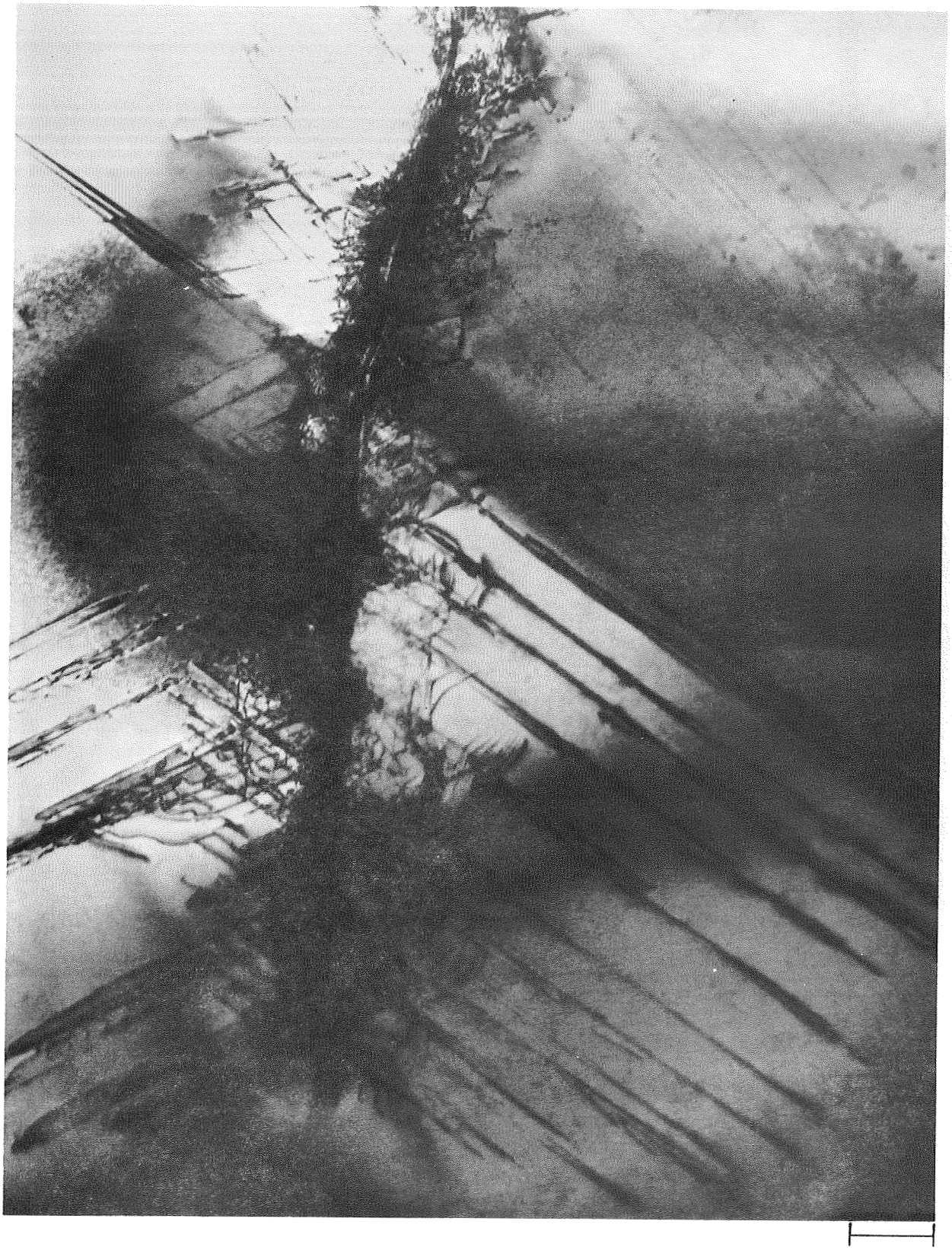

Figure 2

Ti-10% Al (975°C WQ) perforated thin foil showing cracks crossing grain boundary (Solution:acidified KCl - 500mV)

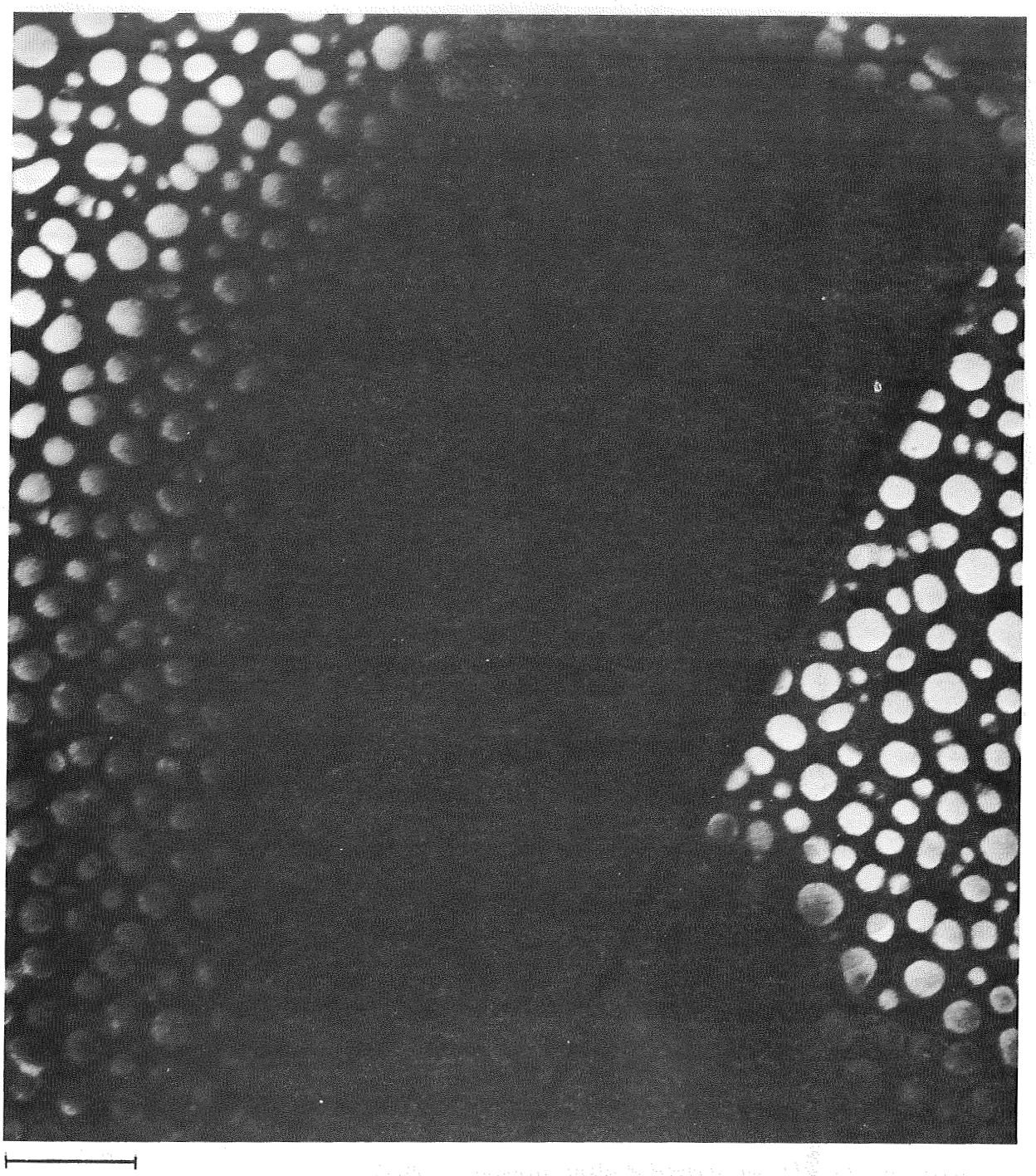

Figure 3

Ti-10% Al (950° WQ + 48 hrs. at 750°C) Dark field (g=[11$\bar{2}$0]) showing crack-note that $\alpha_2$($Ti_3Al$) particles are unchanged at crack surface (Solution: acidified KCl - 500 mV)

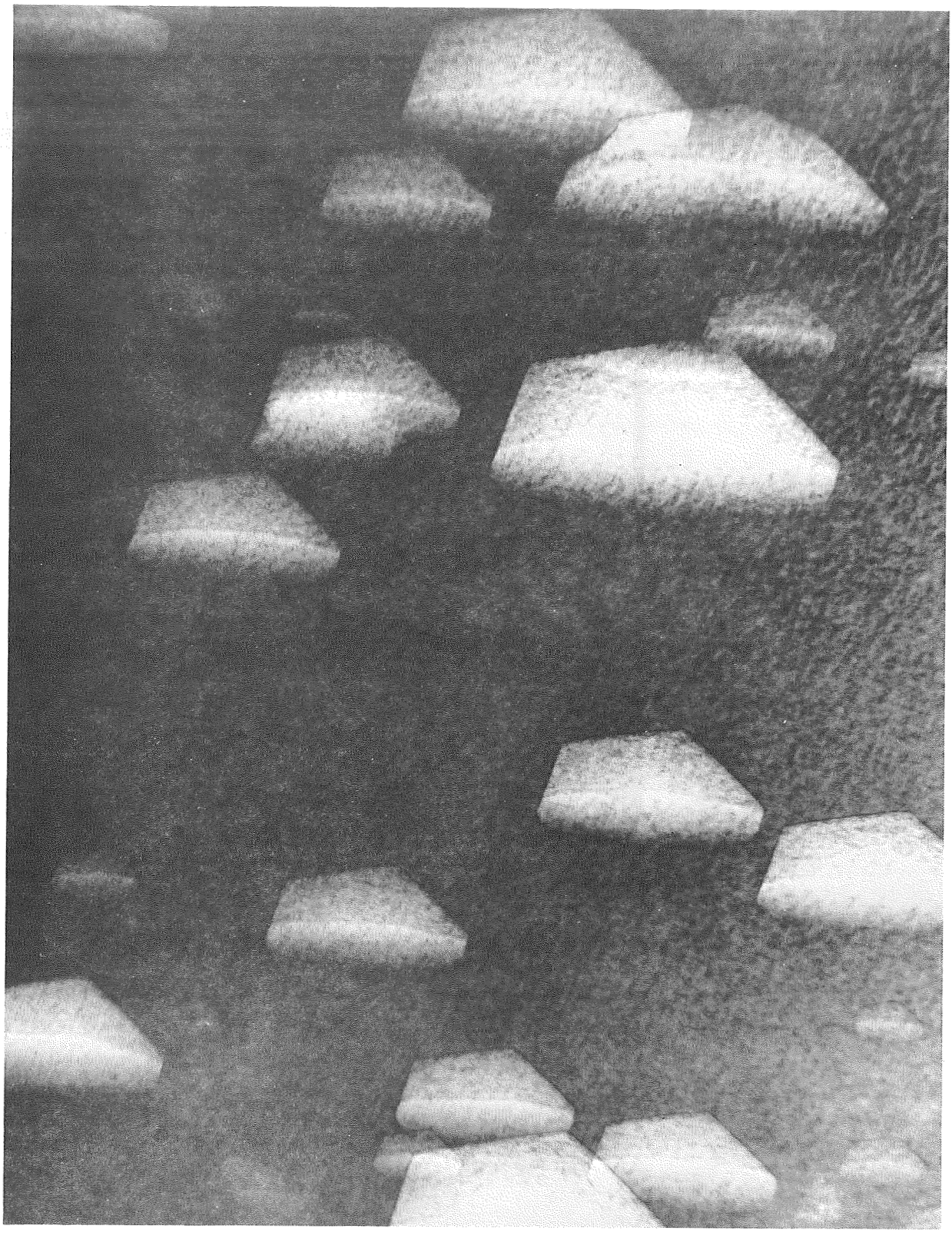

Figure 4
Ti-10% Al (950°C WQ) Pits developed in acidified KI at +1000 mV (note that pit boundaries apparently follow crystallographic planes)

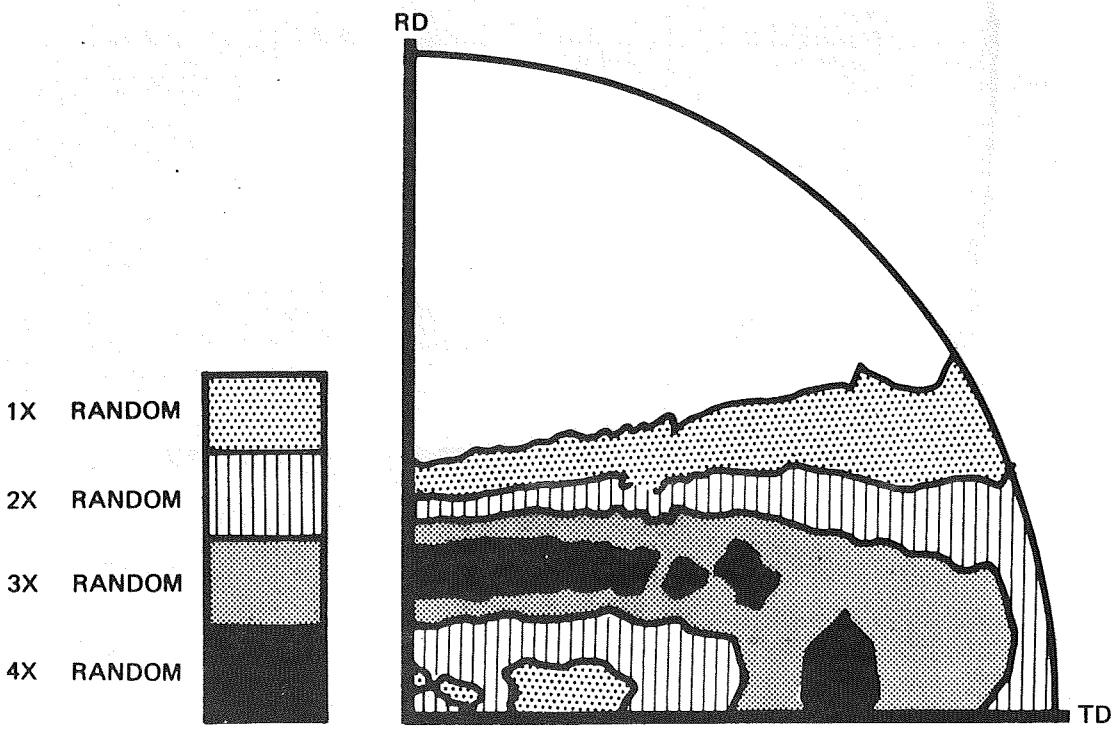


Figure 5
$(0002)_{\alpha}$ pole figure for Ti-6Al-4V(MA) used in this study

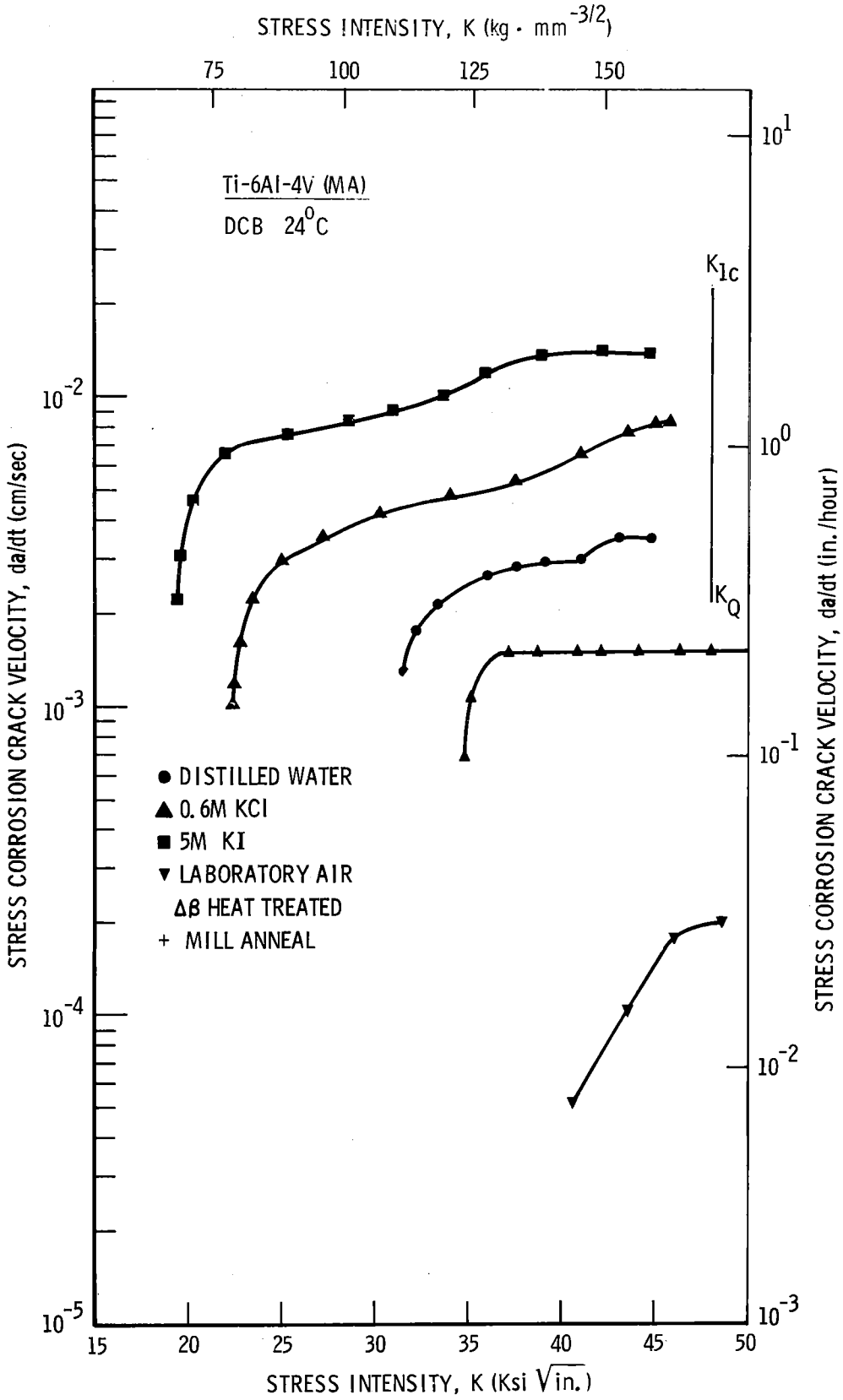


Figure 6

Velocity (V) vs stress intensity (K) for Ti-6Al-4V tested in air, distilled water, potassium-chloride and potassium-iodide environments. Note the influence of β heat treatment on the crack growth behavior in potassium chloride

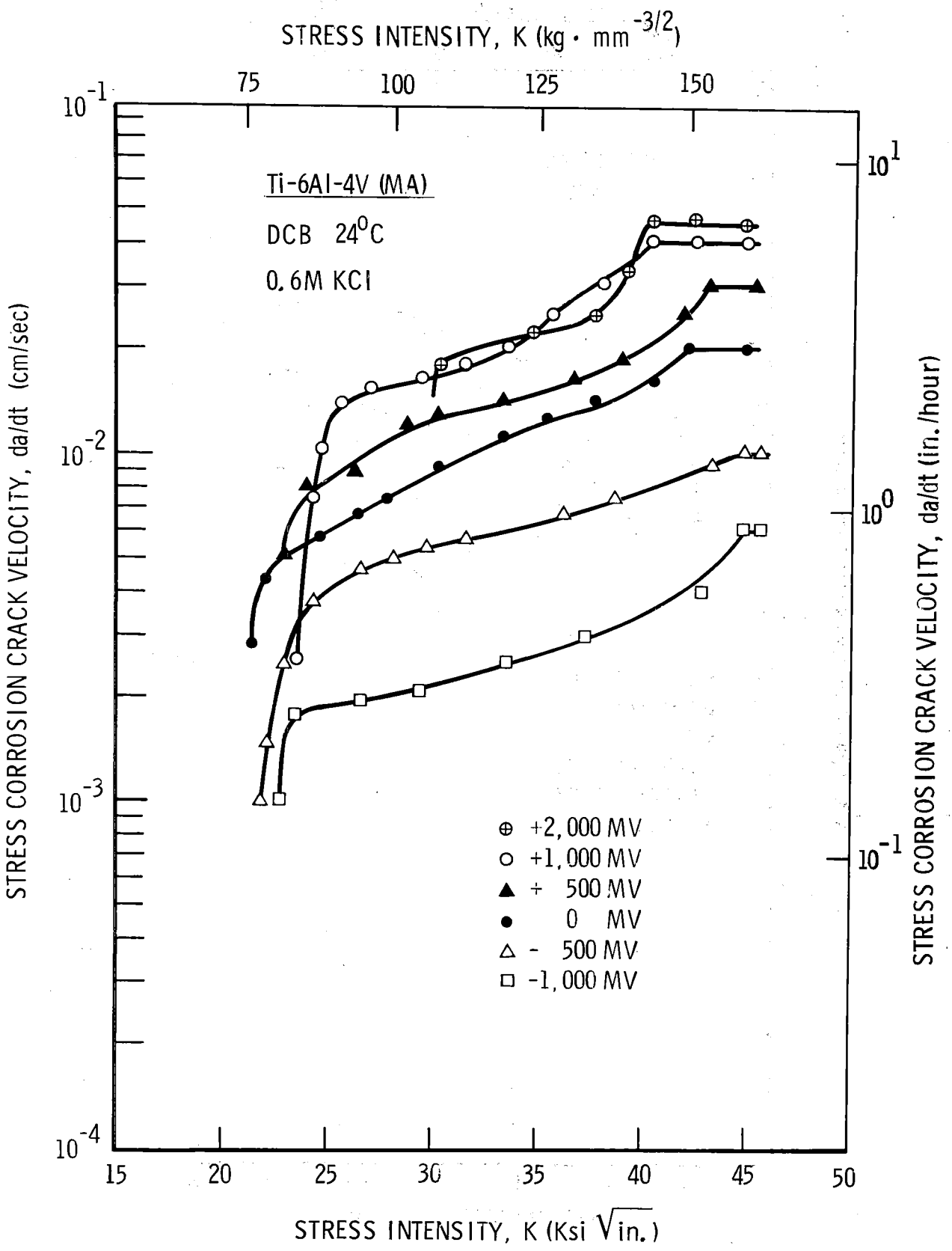


Figure 7

Velocity (V) vs stress intensity (K) relationships for Ti-6Al-4V tested in 0.6M KCL at room temperature and at several applied potentials

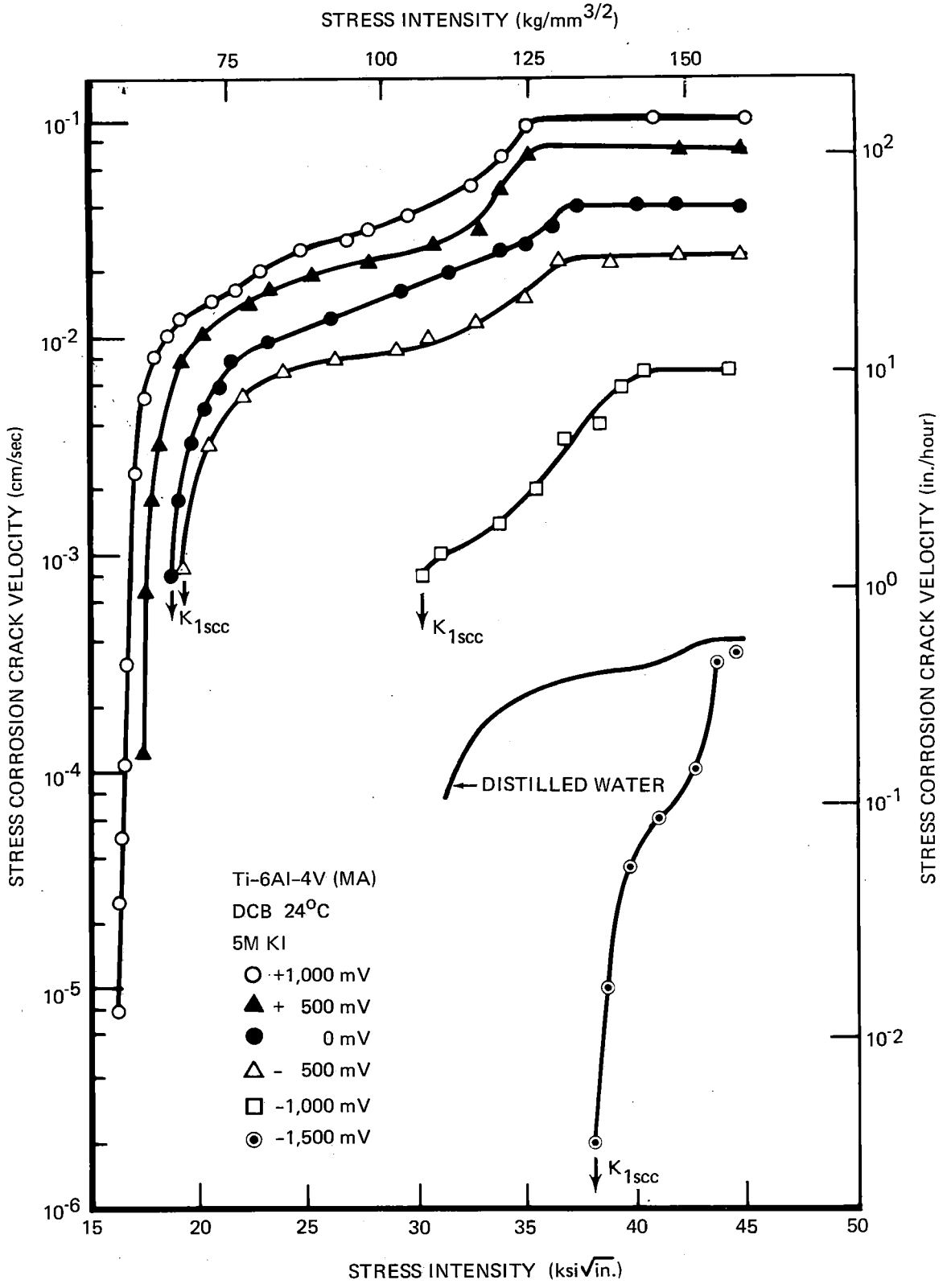


Figure 8

Crack Velocity (V) vs stress intensity (K) relationships for Ti-6Al-4V tested in 5.0 M KI at various potentials

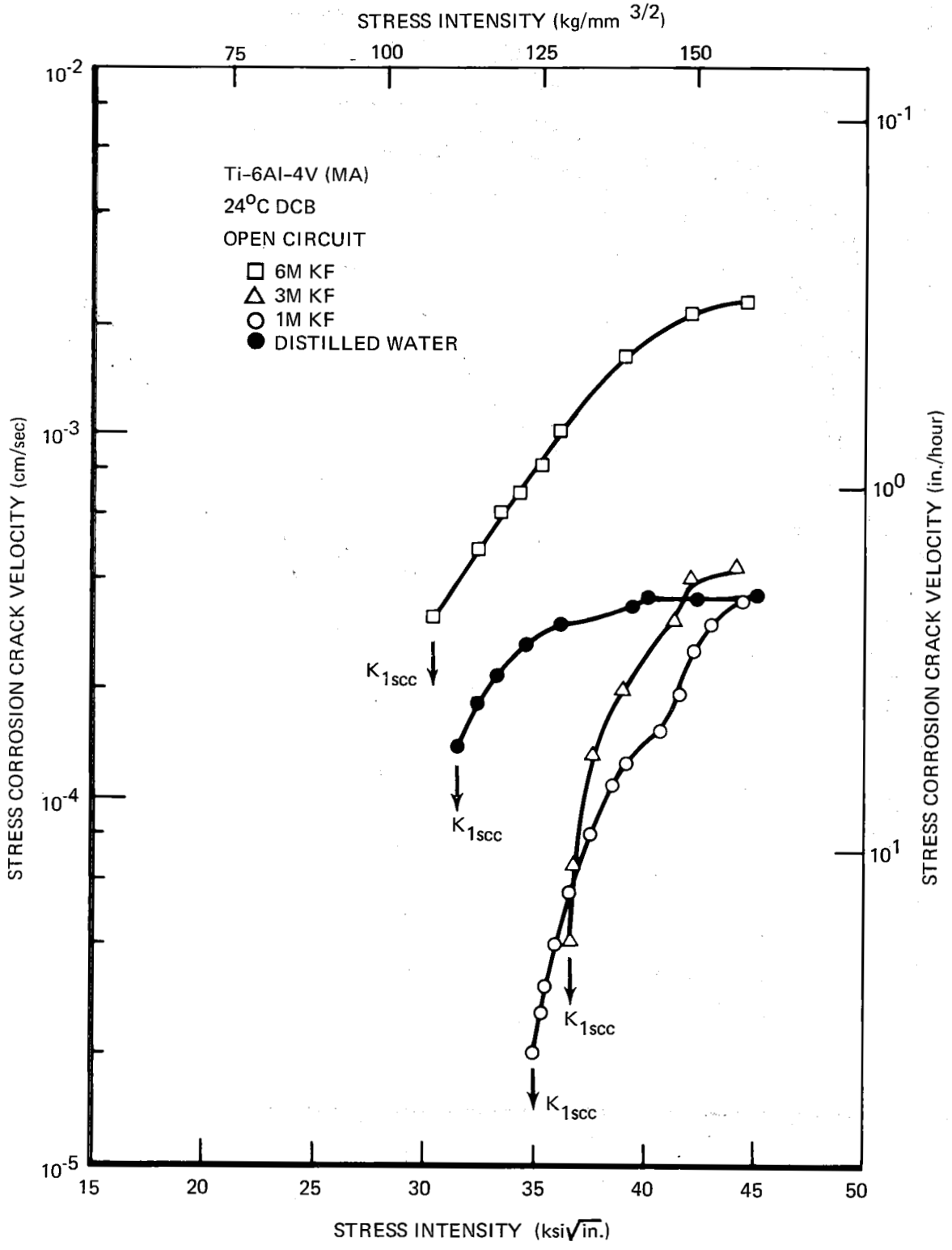


Figure 9

Velocity (V) vs stress intensity (K) relationships for Ti-6Al-4V(MA) tested in fluoride and distilled-water environments

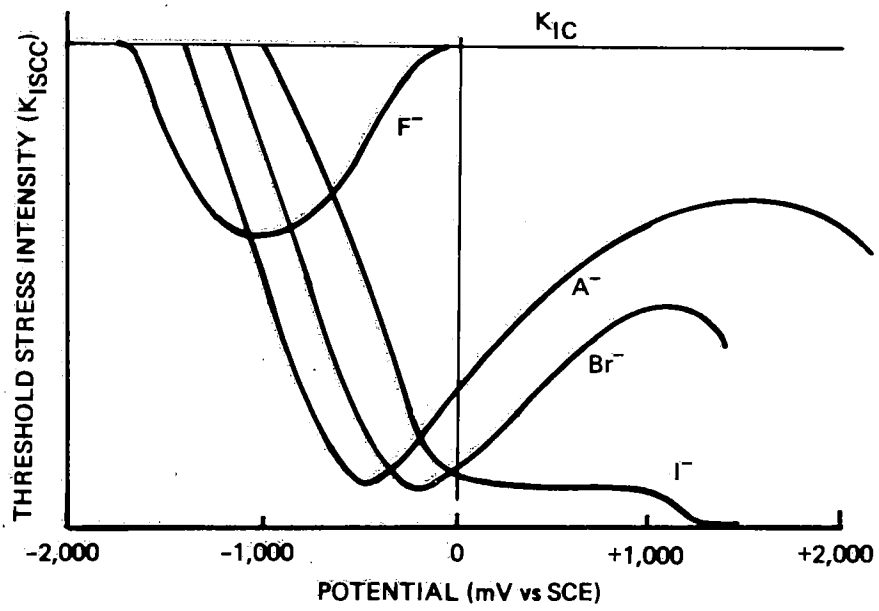


Figure 10

Schematic representation of the dependence of $K_{ISCC}$ on potential of a susceptible titanium alloy in concentrated aqueous halide solutions

## 4.3 STRESS CORROSION CRACKING IN MOLTEN SALTS

This report on the molten salt work is split into three parts. The first part is a description of the work in the LiCl-KCl melts, and except for slight changes is the same as a paper presented at the International Symposium on Stress Corrosion Mechanisms in Titanium Alloys held in Atlanta, on January 27-29, 1971. It will be published in the proceedings of that meeting. The second part, Appendix 1, is an analysis of the transport phenomena associated with precipitation of $K_2TiCl_4$ from KCl melts caused by anodic dissolution of titanium. The third part, Appendix 2, describes the recent results of testing in $AlCl_3$-NaCl-KCl melts.

LiCl-KCl Melts

## INTRODUCTION

The tendency for some titanium alloys to crack when exposed under stress at elevated temperatures in the presence of some halide salts was recognized in 1957. Since this date, a large number of laboratory investigations have confirmed that cracking occurs and have delineated several of the factors which control such cracking. As in many similar situations there was an almost immediate obsession with the mechanism of cracking in spite of the lack of any really quantitative data and this has continued to the present time. The controversy over which chemical species is responsible for hot salt cracking has resolved itself into the usual (at least in titanium SCC problems) pro-hydrogen and pro-halide ion factions, the arguments (again as usual) being remarkable for their volume rather than their scientific merit. Some of the confusion appears to arise from the variability of testing techniques used by various workers. Titanium alloys can be degraded by exposure at elevated temperatures under stress and in various environments in a variety of ways. These could be divided into

| | | |
|---|---|---|
| (a) | General corrosion | At temperature |
| (b) | Subcritical crack growth (SCC) | |
| (c) | Absorption of some degrading species (almost certainly hydrogen) | Usually measured in room temperature - tests after exposure |
| (d) | Metallurgical instability, e.g., an embrittling reaction such as ω-phase precipitation. | |

One of the controversial questions in hot salt SCC is if processes (b) and (c) are related.

An investigation of cracking of Ti:8%Al:1%Mo:1%V in molten salts was initiated as it was considered that such a study might provide a link between aqueous room-temperature SCC and hot-salt cracking. Such molten salt environments are useful both because of the wide temperture range available for study and because the composition variables can be controlled. In addition, very pure chloride melts should enable a critical test of whether hydrogen embrittlement or formation of an oxide plays a critical role in the propagation of a stress corrosion crack. Susceptibility to SCC has been reported for molten LiCl-KCl[1], where the failure of a stressed specimen was stated as "instantaneous".

Two factors are important in the selection of salt systems that can be used to study SCC behavior. These are: (1) the metallic ion in the salt must be higher in the electromotive series than titanium or the titanium will replace the ion, thus restricting the choice of salts to those of the alkali metals, the alkaline earth series, and Al, Zr, and Mn; (2) the melting point of the salt mixture should not be too high, say <450°C, in order to avoid changing the metallurgical structure.

These two restrictions result in a rather limited number of possibilities. For example, no systems based on $SO_4^{-2}$ or $PO_4^{-3}$ are possible, and it is difficult to produce high $F^-$ contents in solution. However, several low melting point eutectics are formed between the various alkali halides, and of

these, two have been used to date in this laboratory:

LiCl - KCl [58 mole % LiCl] mp. 352°C

LiBr - KBr [60 mole % LiBr] mp. 348°C

A second series of low melting point solutions of interest are the alkali nitrates. Three compositions that have been used to date are:

$LiNO_3$ - $KNO_3$ [44 mole % $LiNO_3$] mp. 125°C

$LiNO_3$ - $KNO_3$ [81 mole % $LiNO_3$] mp. 160°C

$NaNO_3$ - $KNO_3$ [50 mole % $NaNO_3$] mp. 223°C

It was found that high concentrations of $Cl^-$ (in the form of KCl) could be added to these melts if the temperature was above 300 - 350°C. Iodide additions were more difficult to make, especially to $LiNO_3$ melts, because reaction occurred. However, iodide could be added to the $NaNO_3$ - $KNO_3$ melts, although in rather low concentrations. A limited amount of work has been performed in hydroxide systems, but as these solutions produce rapid general corrosion, work with these melts has been discontinued.

Other melts that could be considered are cyanides and thiocyanates but these have not been investigated due to their high toxicity. Biphosphates, bisulfates, etc., have low melting points but we have been unable to melt such salts successfully, as dehydration occurs and the melt reverts to a solid.

Relatively recently, tests have been run in $AlCl_3$ - NaCl - KCl mixtures which have the advantage of very low melting points. These tests are of interest for two reasons. First, they should permit a direct comparison of aqueous and molten salt SCC at the same temperature. Secondly, it was found that neither aluminum alloys (7079 grade) nor stainless steel (304 grade)

exhibited cracking in this melt. In both cases there is quite strong evidence that a small amount of water is essential for the occurrence of SCC in these materials.[2,3] Ti8-1-1, on the other hand, is susceptible to SCC in this melt. See Appendix 2 for further discussion.

A table is presented below which summarizes the systems investigated to date, the SCC behavior found, and the conditions of the tests.[4] The results of more extensive work on the nitrate-chloride melts have been discussed previously,[4] and the remainder of the present report will be devoted to the LiCl - KCl eutectic results.

TABLE I

STRESS CORROSION CRACKING BEHAVIOR IN VARIOUS MELTS

| System | Cracking Behavior | Conditions |
|---|---|---|
| LiCl-KCl | Fast cracking | 375°C, dry box |
| $LiNO_3$-$KNO_3$-KCl | Cracking occurs | 375°C, open air |
| LiBr-KBr | Similar to LiCl-KCl | 400°C, dry box |
| KI-$I_2$ | Fast cracking | 80°C, open air |
| $NaNO_3$-$KNO_3$-KCl | Cracking occurs | 300°C, open air |
| $NaNO_3$-$KNO_3$-KBr | Similar to analogous $Cl^-$ system | 300°C, open air |
| $NaNO_3$-$KNO_3$-NaI-Ki | Similar to analogous $Cl^-$ system | 300°C, open air |
| $LiNO_3$-$KNO_3$-KBr | Similar to analogous $Cl^-$ system | 310°C, open air |
| NaOH-NaI | Slow crack growth (also general corrosion | Open air |
| $NaNO_3$-$KNO_3$ | No growth in two days | 450°C, open air |
| $LiNO_3$-$KNO_3$ | No growth in 20 hours | 450°C, open air |
| $NaNO_3$-$KNO_3$-LiF | No growth in 10 hours | 375°C, open air |
| LiCl-KCl-$AlCl_3$ | Fast cracking | 120°C, dry box |

The thermodynamics of the electrochemical reactions of interest in this work are summarized in the table below. The data are taken from Plambeck.[5]

TABLE II

Electromotive Force Series in LiCl - KCl Eutectic at 450°C

| Couple | $E_m^\circ$ (volts) |
|---|---|
| $Li(I) + e^- = Li(s)$ | -2.561 |
| $\frac{1}{2} H_2(g) + e^- = H^-$ | -2.057 |
| $Al(III) + 3e^- = Al(s)$ | -1.019 |
| $Ti(II) + 2e^- = Ti(s)$ | -0.997 |
| $Ti(III) + 3e^- = Ti(s)$ | -0.857 |
| $Ag(I) + e^- = Ag(s)$ | 0.0 |
| $HCl(g) + e^- = \frac{1}{2} H_2(g) + Cl^-$ | +0.049 |
| $\frac{1}{2} Cl_2 + e^- = Cl^-$ | +1.065 |

We arbitrarily chose Ag(I) (melt)/Ag(s) as the reference for the table since this was the reference electrode used in the tests.

EXPERIMENTAL

The LiCl-KCl eutectic used in these studies was obtained from the Anderson Physics Laboratory, and specified to contain less than 1 ppm hydrogen as $OH^-$. The material was handled only in the dry box.

The alloy Ti-8Al-1Mo-1V was selected for the investigation for several reasons. Considerable data had been generated on this alloy in this laboratory in the form of velocity:stress intensity relationships for several environments and thus formed a useful basis for comparison.[6] This alloy has been tested extensively under hot salt SCC conditions, again a useful comparative basis.[7] Further, Ti-8Al-1Mo-1V exhibits several properties which are advantageous to the experimentalist, a wide range of SCC susceptibility with heat treatment and a preferred orientation with the basal planes lying parallel to the rolling direction allowing the utilization of DCB specimens. Three sheets of Ti8Al-1Mo-1V have been utilized in this program, two sheets showing the texture shown in Fig. 1 while the third sheet showed a less pronounced texture. Three heat treatments have been studied to date which are

(a) 800°C for 1 hours, step cooled to 500°C over 72 hours (S.C.)

(b) 800°C for 2 hours, water quenched (D.A.)

(c) 1100°C for 1/2 hour, water quenched (M)

A typical DCB specimen used in this study is shown in Fig. 1 together with sheet and preferred orientation information. These specimens were stressed using a wedge made of a Ti-Mo alloy heat treated to a strength level of 190 Ksi. The stress intensity values were calculated from the

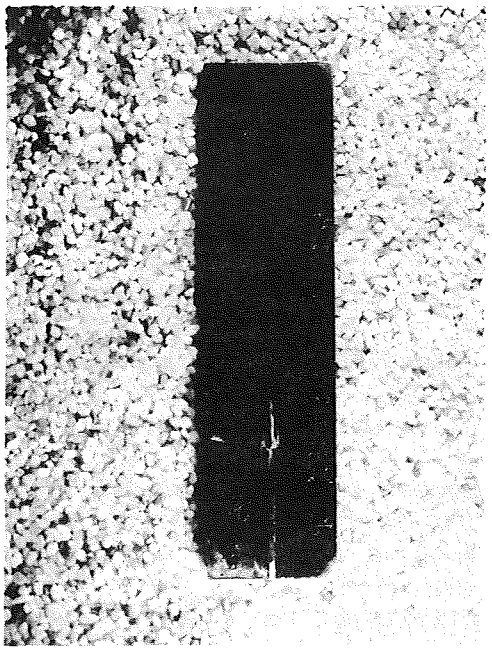

(a) DCB Specimen

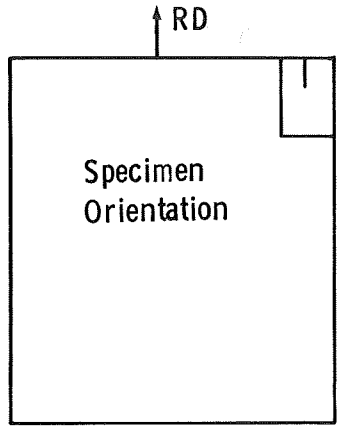


(b) Orientation of WR DCB-Specimens Used

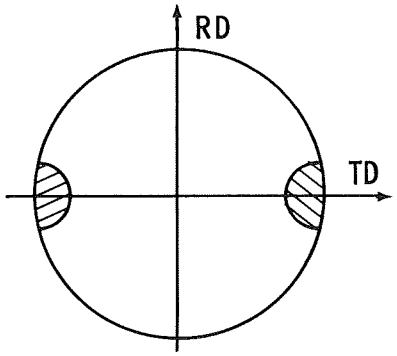


(c) Idealized $(0002)_\alpha$ Pole Figure for Sheet

Fig. 1. Specimens and preferred orientation information for the Ti8-1-1 used in the study

standard equation relating crack length to deflection. The advantages of such specimens are their simplicity and the ease of loading and testing as no external loading system is required nor are any dissimilar metals introduced into the molten salt.

The tests were conducted in a dry box which maintained the argon atmosphere at about 10 ppb water and about 10 ppm oxygen and nitrogen. The melts were contained in a pyrex cell. The temperature of the metal was maintained at the desired level to $\pm$ 5°C, as measured by a thermocouple.

All the tests were performed under potentiostatic control. The reference electrode used was a silver rod partially immersed in a melt of AgCl in the LiCl-KCl eutectic inside a pyrex tube closed on one end. The closed end was immersed in the bulk melt, and the conductivity of the glass made electrical contact possible. The potential of this reference electrode differed from the standard electrode Ag/Ag(I)(melt) listed in Table II by about 200 mV. The specimen was inserted into the melt under potential control, with the specimen at -1800 mV with respect to the Ag(s)/Ag(I) reference electrode. The rest potential (with zero net current) of the specimen was about -1175 mV versus the reference electrode.

Fast cracking was followed by using motion picture photography, while visual observation was adequate for slower propagation. The crack length was recorded as a function of time. This made it possible to calculate velocities of cracking, at a particular stress intensity. These data will be reported below.

RESULTS

A. Effect of Stress Intensity on Crack Propagation Velocity

Data on the velocity of cracking is given in Figs. 2, 3, and 4. For both the step-cooled and duplex-annealed heat treatments, the propagation velocities may be divided into two regions. As in other environments, the velocity of cracking is strongly stress dependent at low crack tip stress intensities, and becomes independent of stress at higher K. The magnitude of the velocity is very similar for both heat treatments, at a particular value of stress intensity, and the curves become identical for velocities below $10^{-2}$ cm/sec. The behavior in "wet" melts is also included in the figures, as noted, for water contents of 10-50 ppm. No significant differences can be noted between the velocities in these "wet" melts and those with about 1 ppm water. The relative amounts of water in these melts were estimated from the relative (limiting) currents measured at -1800 mV. A more systematic investigation of the influence of water, and at higher concentrations, is planned for the near future. The maximum water content attainable is about 130 ppm, before significant degradation of the glass occurs.[8]

B. Influence of Temperature on Crack Velocity

The influence of temperature on crack velocities, in step-cooled Ti 8-1-1, in region II, is presented in Fig. 5. The activation energy of about 3 kcal is compatible with a diffusion-limited process.

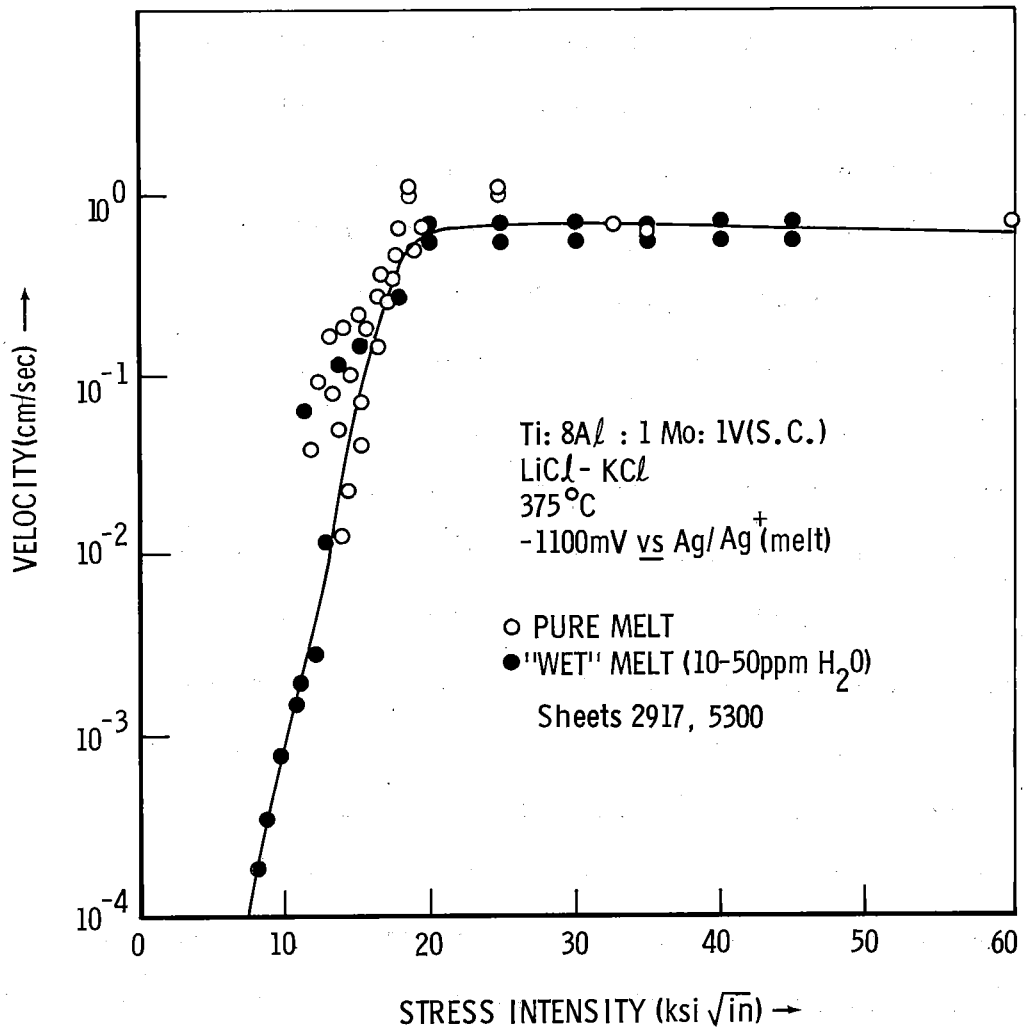


Fig. 2. Log velocity as a function of stress intensity for step-cooled Ti8-1-1 in LiCl-KCl eutectic at 375°C

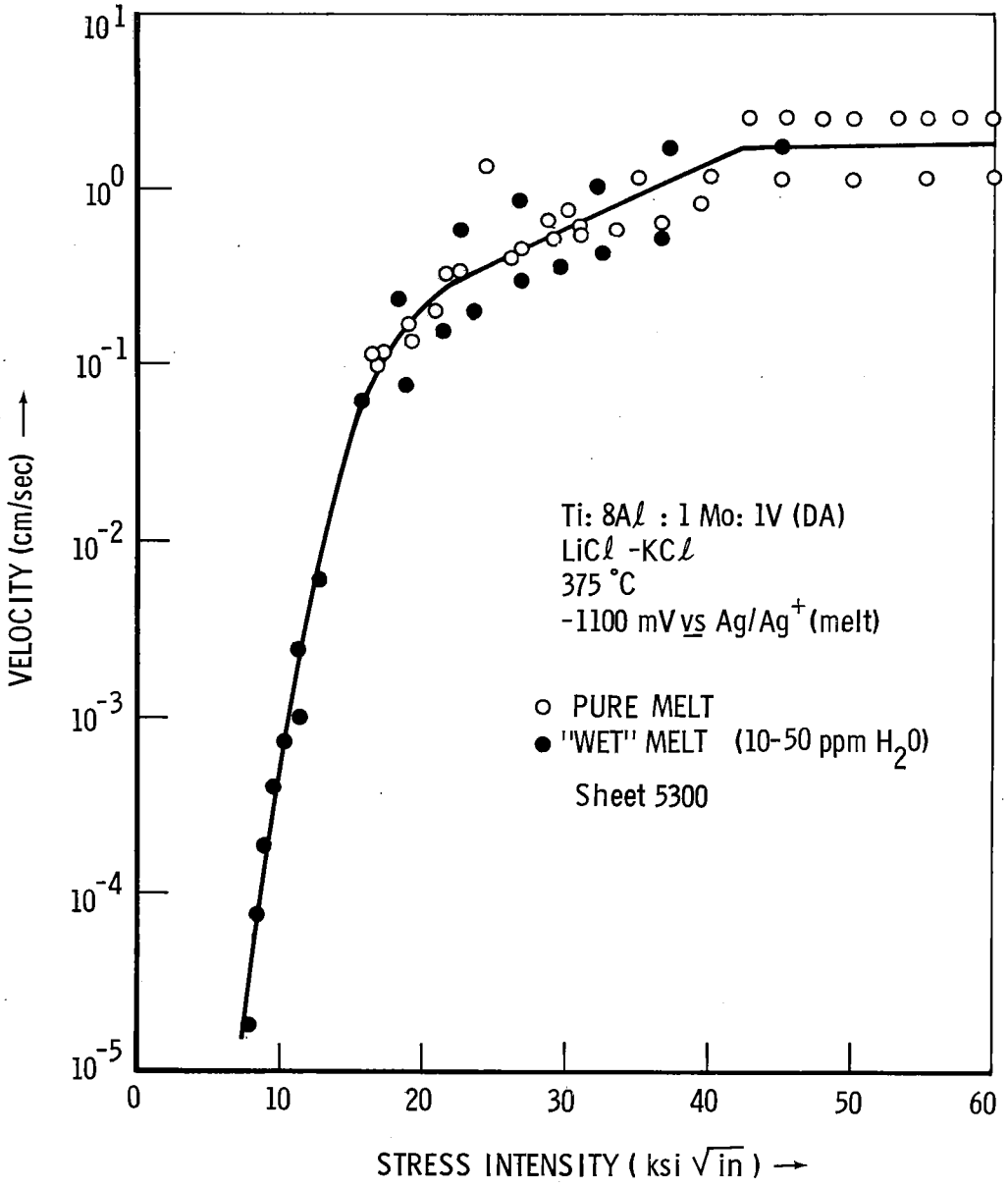


Fig. 3. Log velocity as a function of stress intensity for duplex annealed Ti8-1-1 in LiCl-KCl eutectic at 375°C

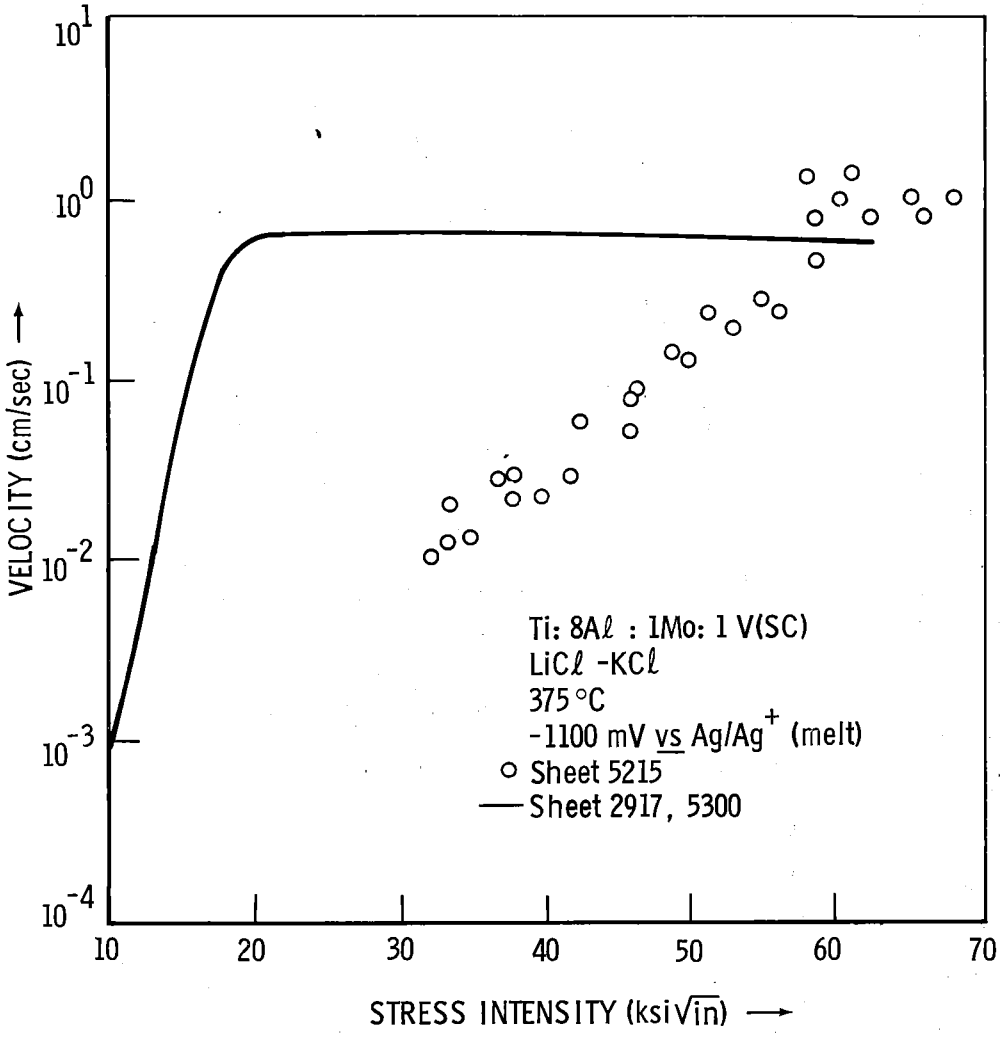


Fig. 4. Log velocity as a function of stress intensity for three sheets of step-cooled Ti8-1-1 in LiCl-KCl eutectic at 375°C

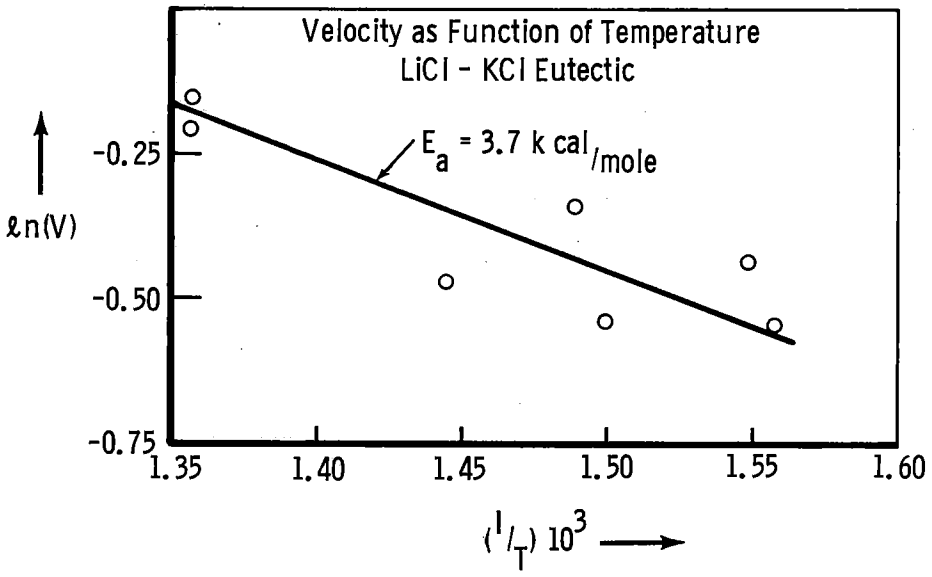


Fig. 5. Velocity as function of temperature for step-cooled Ti8-1-1 in LiCl-KCl eutectic, in Region II, at -1100 mV (vs $Ag/Ag^+$ melt)

C. Effect of Metallurgical Parameters on Crack Velocity

Two metallurgical parameters have been investigated to a limited extent in this investigation - heat treatment and preferred orientation. The heat treatments studied are listed in the experimental section and the phase structures produced are essentially $\alpha+\alpha_2(Ti_3Al)$ (SC), $\alpha+\beta$(DA) and martensitic $\alpha'$(M). Changes in phase structure at the test temperature for SC and DA material can probably be neglected as the testing times especially for region II type growth studies are relatively short. However, some decomposition (tempering) of the martensitic (M) structures are possible, although this has not been investigated at this time. From Figs. 2, and 3, it can be seen that there is little difference between the V:K curves for SC and DA material although slight differences in the transition region from region II to region I growth are observed, this region being more marked in DA material. Problems were encountered with the measurement of V:K curves for SC and DA material although slight differences in the transition region from region II to region I growth are observed, this region being more marked in DA material. Problems were encountered with the measurement of V:K curves for M-Material due to crack branching which caused the crack to deviate from the center plane of the specimen. Thus neither velocity nor stress intensity could be measured with any degree of accuracy. Results obtained indicate that cracks propagate more slowly in M-type specimens-crack velocities of $\sim 8 \times 10^{-2}$ cm/sec at K values from 50-70 being observed.

The second metallurgical factor studied is that of texture within the various sheets of Ti8-Al-1Mo-1V tested. The influence of this parameter may be seen by comparing the V:K curves shown in Fig. 4. from which it can be seen

that both the transition region velocities and the region I velocities are displaced to higher K levels for sheet 5215, as compared to sheets 2917 and 5300. Differences in texture between these two materials are shown in Figure 6 which consist of the three faces of the sheet material which have been color etched (such a procedure delineates the basal planes of the hexagonal phase which appear as yellow regions - white in these photographs)[9]. It can be seen that the more random texture (Figure 6(b)) exhibits V:K curves displaced to higher K levels.

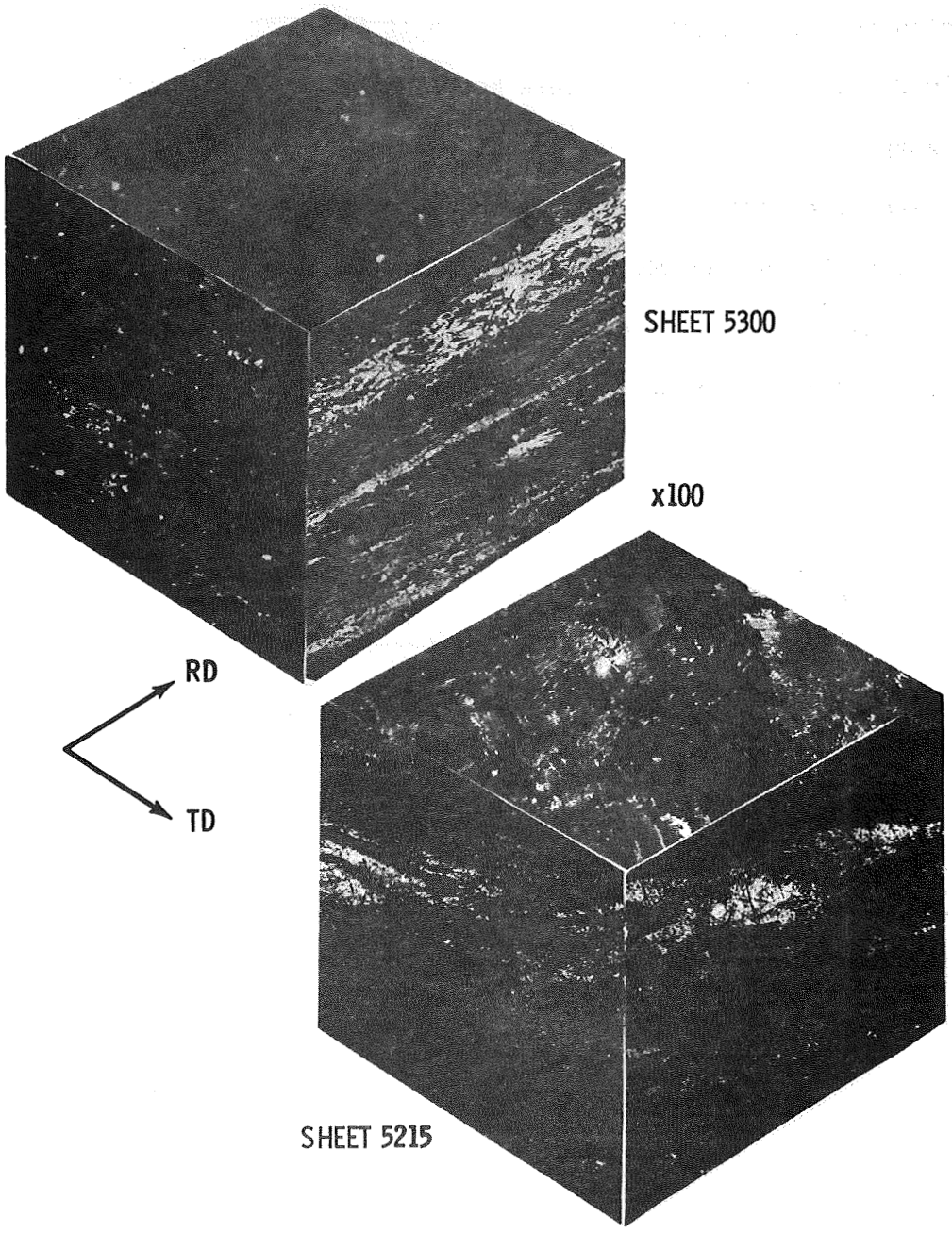


Fig. 6. The texture of two sheets of Ti8-1-1 used in the study

D. Effect of Electrical Potential on Crack Growth Rates

The discussion of the effects of potential will be divided into two parts, namely the cathodic protection effects, and the quantitative effect on the V:K curves.

The cathodic protection effects are the key to the successful tests which we have made in this melt. A specimen was usually placed in the melt (after being preheated to the temperature of the melt) at a potential of -1800 mV vs the reference electrode. This protected the specimen for as long as desired, that is, there was no crack propagation observable during this protection period. The rest potential of the specimen was usually about -1175 mV, as mentioned earlier. In order to propagate a crack, the potential was switched quickly to the desired value (e.g., -1100 mV) and maintained there for the duration of the test. Crack propagation was initiated almost immediately, usually within five seconds. The crack could be stopped immediately by switching the potential back to -1800 mV. It was more difficult to initiate cracking at potentials more negative than -1250 mV, as will be discussed below, but the cracking could always be stopped by switching the potential back to -1800 mV. This indicates that potentiostating the specimen at -1800 mV was effective in protecting against crack propagation as well as crack initiation.

The results of the effect of potential on propagation velocity will be discussed by comparison with the results at -1100 mV, as reported in figure 3. All these results were obtained on duplex-annealed specimens

at 375°C. For potentials more positive than -1200 mV, the velocity in region II is not influenced by the electrical potential. It is not clear at this time whether or not this is also true for potentials more negative than this. Some data at -1400 mV and -1475 mV indicate a lower velocity in region II than at -1100 mV, but the uncertainty in the data is too large to make a more definite statement. One reason for the uncertainty in the data is that poor movies have been obtained for the few tests run at these negative potentials. Another reason is the difficulty associated with initiating cracks at potentials more negative than -1200 mV. It has not been possible to initiate cracks at -1400 for example, by switching the potential directly from -1800 mV. The technique of switching from -1800 mV at -1100 mV to initiate the cracks, and then to the potential of interest (say -1400 mV) has been partially successful, but leads to some difficulty in interpreting the data obtained during the switching. More testing will undoubtedly resolve this uncertainty.

The effect of potential in region I is generally to produce a higher velocity the more positive the potential, at a particular value of the stress intensity. Another way of saying this is that the velocity of $10^{-5}$ cm/sec is achieved at lower values of the stress intensity, the more positive the potential. Potentials more positive than -1100 mV lead to V:K curves above (higher velocity at same stress intensity) and roughly parallel to that for -1100 mV. The curves tend to merge at about 20 ksi$\sqrt{\text{in}}$ and higher for these potentials. Potentials more negative than -1100 mV lead to V:K curves

shifted not only downward, but also to the right, in comparison to figure 3. This is shown by the values of stress intensity at which the velocity was found to be $10^{-5}$ cm/sec. That is at -900 mV the stress intensity was about 4 ksi$\sqrt{in}$, at -1100 mV about 7 ksi$\sqrt{in}$, at -1200 mV about 14 ksi$\sqrt{in}$, at -1350 mV about 25 ksi$\sqrt{in}$, at -1400 mV about 32 ksi$\sqrt{in}$, and at -1475 mV about 36 ksi$\sqrt{in}$. The full V:K curves are not reported here because of poor reproducibility at the more negative potentials, but the trends described here are always found. These results are quite consistent with the cathodic protection effects mentioned above.

Several tests were also run in which the potential was changed slowly from -1800 mV to more positive values. Cracking occurred only when the potential was in the neighborhood of -1200 mV to -1150 mV. The current flowing into the specimen was cathodic at -1800 mV (and small), but was anodic ( 1 mA /$cm^2$ of bulk surface) when crack propagation occurred. The sharp anodic current increase associated with cracking is shown in figure 7. The time scale on this figure is such that all the rapid propagation in region II, and much of that in region I, took place in the time spent at the current peak. The sharp decrease in current from the peak must represent passivation of the crack surface, perhaps by precipitation of a solid such as $K_2TiCl_4$ (see below for further discussion).

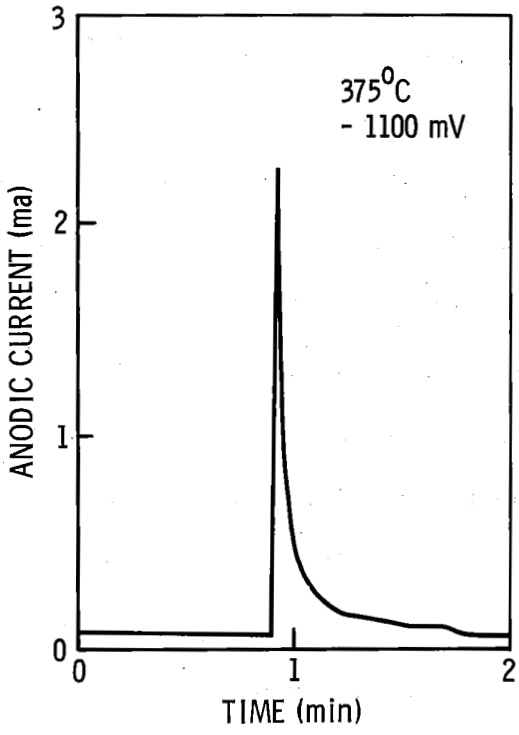


Fig. 7. Current as a function of time at initiation of cracking (Ti8-1-1 in LiCl-KCl eutectic)

E. Influence of Added $H_2O$ and LiH

Results have been obtained from experiments designed to reveal the influence of water, and in particular hydrogen. The data in Figures 2 and 3 as already mentioned, revealed no effect of changing the water content of the melts. The cathodic protection results, presented above also indicate that neither $H^+$ nor $H_2$ is important, since it is in this region of potential that any influence should be found. We have also performed experiments in which water was introduced into a melt with a specimen under cathodic conditions, and noted that the cathodic current increased (as expected) by a factor of 10. Associated with this increase of current was the evolution of gas (assumed to be $H_2$) from the specimen surface, and no cracking was observed. We also used a specimen in which a crack had been propagated for several millimeters in distilled water, in the open laboratory. This specimen, still stressed, was introduced into the dry box, inserted into the melt under cathodic control, and no cracking was observed.

Experiments were also conducted in which LiH was added to a melt, to a concentration of about 0.1 M. For potentials more positive than -2100 mV, $H^-$ was oxidized to $H_2$ gas which was evolved from the speciman surface. A limiting current of 10 $mA/cm^2$ on the specimen was attained at about -1800 mV and was constant at this level out to -1100 mV, where Ti began to dissolve anodically. No cracking was observed for potentials more negative than -1100 mV, but cracking occurred at this potential, with an attendant increase of anodic current. The velocity of cracking could not be determined accurately because of the opacity of the inert container (BN) used to hold the melt, but it was about 0.5 cm/sec.

G. Mode of Cracking

Region II and the transition region crack fracture surfaces exhibit cleavage-like features as shown in Fig. 8(a). Fracture surfaces produced during region I type growth indicate that separation occurs by a mixture of cleavage and intergranular separation, Fig. 8(b). Such behavior is typical of Ti-8Al-1Mo-1V and other $\alpha+\beta$ type alloys tested in a variety of environments, e.g. methanolic solutions and liquid mercury.[6] The crystallography of the cleavage plane in molten salts has not been investigated directly; however, the influence of preferred orientation and the similarity of its effect on SCC in both aqueous and molten salt solutions indicate that the plane must lie near the basal plane.

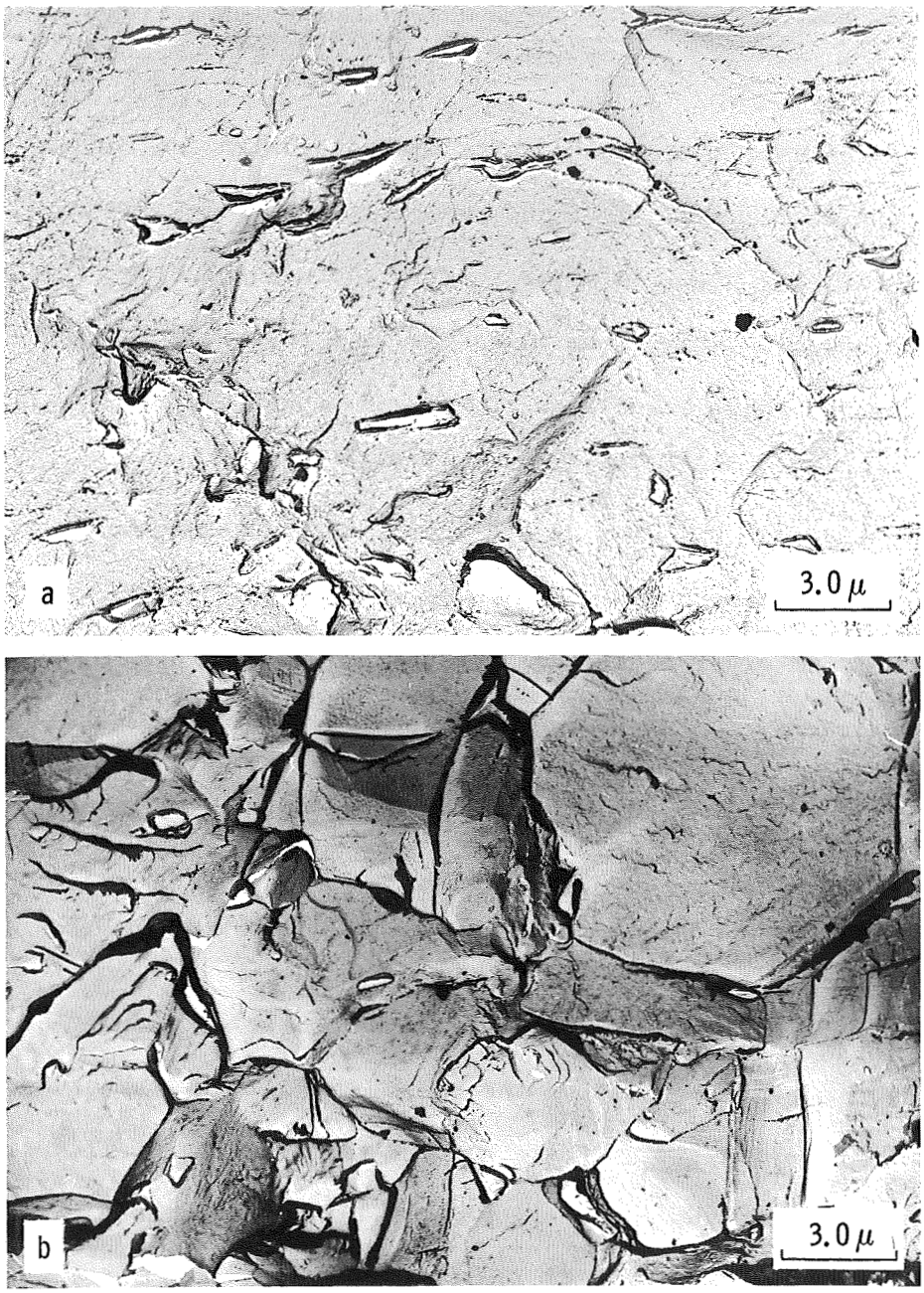


Fig. 8. Crack fracture surfaces in (a) Region II, and (b) Region I

DISCUSSION

Our data indicate that the presence of hydrogen in the form of $H^+$, $H_2$ or $H^-$ has no influence on the cracking behavior of Ti 8-1-1 in the LiCl-KCl eutectic, and plays no major role in the mechanism for crack extension. In addition, the velocity of the fast cracks is too large to be caused by the small quantities of hydrogen available in the pure melts. This may be shown by a simple calculation.[10]

One may calculate the flux of hydrogen ions reduced to $H_2$ at a limiting current by solving the equation of continuity. In the presence of a large excess of other current carriers (i.e., the $Li^+$, $K^+$, and $Cl^-$ ions) and under steady-state, stagnant conditions (i.e., the solution is pulled along with the crack), the equation of continuity becomes

$$\nabla^2 C_{H^+} = 0$$

For a wedge-shaped, sharp crack, with hydrogen ions being reduced at the limiting current along the walls of the crack, the flux of these ions to the crack tip is exactly zero. For a rounded tip (for the small angle cracks of interest here the exact shape is of little importance), with hydrogen ions also being reduced at limiting current at the crack tip, and the flux of current into the crack of

$$\frac{i_{lim}}{FD_{H^+}} ,$$

The flux of hydrogen ions to the crack tip is now

$$\left(\frac{8}{\pi}\right)\left(\frac{i_{lim}}{FD_{H^+}}\right)\left(10^{-3}\right)^{\pi/\theta_1-1}$$

For a crack angle of 2°, i.e., $\pi/\theta_1 = 90$, the flux is not zero, but is certainly small. Therefore, we conclude that only a small velocity of cracking could be supported by hydrogen ion reduction in molten LiCl-KCl.

Having eliminated, we believe, a mechanism of cracking involving hydrogen, we may also eliminate one involving oxygen by referring to the same data. Those mechanisms which seem most consistent with our data are anodic dissolution, or adsorption of a damaging species at the crack tip.

If anodic dissolution were solely responsible for crack extension, current densities at the crack tip of the order of $10^4$ A/cm$^2$ would be required for velocities of 1 cm/sec in titanium. Furthermore, the current density on the walls of the crack would have to be much lower than at the tip or blunting of the crack would occur. If the same reaction were occurring on the walls of the crack and at the tip, and there were no passivating processes involved, the theoretical current distribution is completely opposite to this. That is, Wagner[11] and Cheh[12] have shown that the current density decreases with distance down a notch, and is zero at the crack tip in the limit of a current determined solely by ohmic resistance in the electrolytic solution. Therefore, the effect of having clean crack walls would be to distribute the current away from the tip, producing a blunted crack. One moderates this by including the activation polarization effects but these are expected to be

small in this molten salt system. This conflict between what is theoretically allowable and what is required in order to have crack extension by anodic dissolution, could be resolved by one of three possibilities:

(1) a passivation process occurs on the crack walls, thus reducing the current density there, and allowing more current to flow to the tip;

(2) aluminum is preferentially dissolved from the material, thus exhausting aluminum from the surface of the crack wall, and lowering the current density, away from the crack tip, or;

(3) stress effects are such as to cause greater dissolution at the crack tip than on the walls.

A passivation reaction in LiCl-KCl could be the formation of $TiCl_2$ films, or a mixed chloride such as $K_2TiCl_4$. A phase diagram of $TiCl_2$-KCl-LiCl is not available in the literature, although the binary systems have been investigated. $TiCl_2$ forms a continuous series of solid solutions with LiCl, but forms both $K_2TiCl_4$ (a peritectic) and $KTiCl_3$ (a congruent solid) with KCl (24). It is worthwhile to analyze the level of Ti dissolution current that would be needed to precipitate $K_2TiCl_4$ from a $TiCl_2$-KCl melt, to determine if the current required is reasonable for the system under investigation. From the results in Appendix 1, we see that at steady state, a current of **168** $mA/cm^2$ could precipitate $K_2TiCl_4$ from a melt of $TiCl_2$-KCl. Since we are not even sure that this solid

would precipitate from melts containing LiCl, nor are we certain what the melt composition would have to be to precipitate the solid if it did, it is not possible to draw a very definite conclusion from this result. But we can say that it is reasonable to expect that a solid of some composition could be produced at the current levels (up to $10^4$ A/cm$^2$) appropriate in a propagating crack.

With regard to the second possibility, chemical analysis of a bulk melt after a stress corrosion test revealed the presence of both aluminum and titanium, but this is not believed to be indicative of the concentrations in the crack. However, some slight preferential dissolution of Al might be expected in view of the data presented in Table II. This type of attack has been found in several other systems, and Harrison and Wagner[13] present data for preferred dissolution effects (not SCC) for an alloy in one molten salt system.

The final possibility has been discussed by several people (e.g., Despic, et al[14]), but no quantitative data are available for oxide-free surfaces.

If aluminum is anodically dissolved in the melt, Al (III) will be formed, but the high vapor pressure of $Al_2Cl_6$ will limit the amount which can be retained in the melt at the temperatures of interest here. The dissolution of titanium is more complex, with both Ti(II) and Ti(III) formed. The Ti(II) species will predominate for potentials more negative than about -0.86 volts. At equilibrium, with Ti, Ti(II), and Ti(III) all present, the ratio of Ti(II) to Ti(III) may be calculated from

$$K_{eq} = \frac{[Ti(II)]^3}{[Ti(III)]^2} \approx 10^6 ,$$

where $K_{eq}$ is here the equilibrium constant.

An adsorption mechanism might be viewed as:

(1) a damaging species arriving at the crack tip;

(2) adsorbing on the atoms there, thus weakening the inter-metallic bonds, and;

(3) finally leading to separation of these atoms and crack extension.

The requirements for such a mechanism are that there should be a damaging species, and that it should be supplied in such quantities as would be required to promote bond-breaking. In addition, our data indicates that the adsorption process would have to be strongly potential-dependent. The function of stress in such a mechanism would be the creation of vulnerable sites, localized in this case at the crack tip.

The present data just do not allow any decision to be made concerning which of these mechanisms (or some other) is appropriate for our system. More experiments will have to be performed before further discussion is

warranted. However, the simple nature of this LiCl-KCl system should make it possible to perform definitive experiments which will reveal much about the basic mechanism. In particular, the multiplicity of reactions and species found in aqueous solutions is reduced in this melt, so that more careful control of variables is possible.

Much further work is also required to evaluate the influence of heat treatment on the SCC behavior of titanium alloys in molten salts. The similarity of the V:K curves for DA & SC type material found in this investigation is different from the quite large change observed in these heat treatments on testing in aqueous and other solutions at room temperature. However this difference may be attributed to the similarity in mechanical properties of these materials at elevated temperatures.[15] The gradual convergence of such properties may also reflect similar deformation substructure (dislocation arrangements) a factor which has been correlated with SCC at room temperature. However, confirmation of such speculation must await direct analysis of deformation substructures. The influence of texture is similar in both molten salt and aqueous environments, the $K_{1SCC}$ values for the two sheets shown in Fig. 4 were determined as 34 Ksi $\sqrt{in}$ (sheet 5215) and 17 Ksi $\sqrt{in}$ (sheet 4300).

In the introduction it was stated that this work was performed apart from any intrinsic merit to bridge, possibly, the gap between hot salt SCC and aqueous SCC at ambient temperatures. It is obvious that certain features of molten salt cracking show strong similarities with SCC in several environments at ambient temperatures. The shape of the V:K relationships and the fracture path are two such correlations.[6]

In regard to the relation of these molten salt experiments to hot salt SCC the following points can be made. The rates of cracking in molten salt are many orders of magnitude higher than the limited data reported for hot salt SCC. However, most reported rates could become equivalent in region I type growth in molten salts. It may be significant that the predominant fracture mode reported for $(\alpha+\beta)$ alloys in hot salt SCC is intergranular which therefore may correlate with region I. The present investigation has also shown that $Cl^-$ is sufficient to cause cracking in Ti-8Al-1Mo-1V at elevated temperatures. It has never been unambiguously shown that hot salt cracking occurs in the absence of water and thus hydrogen. Recent tests by Gray and Johnson[16] have demonstrated that cracking may occur at very low water contents of the dynamic air stream used in the tests. However, the authors, who attribute cracking to hydrogen, point out that the applied salt layer may contain some water. One question that must be answered if the $Cl^-$ ion is responsible for hot salt cracking is how it is transported to the crack from the solid NaCl crystals. The observations of Kirchner and Ripling[7] that solid or liquid films are formed during exposure at elevated temperatures which migrate on the specimen surface may indicate that some lower melting point mixture is created by reaction of the NaCl, oxide layer and metal.

## SUMMARY

This report has given data on stress corrosion cracking of Ti8-1-1 in LiCl-KCl melts at different temperatures, and for three different heat treatments. Experiments were conducted to determine the influence of hydrogen, with results which indicated no importance of $H^+$, $H_2$, or $H^-$ in the cracking mechanism. Finally, the implications of an anodic dissolution mechanism and an adsorption mechanism have been discussed.

## APPENDIX 1

The fundamental equation for transport phenomena in molten salts is,[17]

$$C_i \nabla \mu_i = \sum_j K_{ij} (\underline{v}_j - \underline{v}_i) \qquad (1)$$

where

$C_i$ is the concentration of species i in $\left(\frac{\text{moles}}{\text{cm}^3}\right)$

$\nabla \mu_i$ is the gradient of electrochemical potential of i in(calories/cm$^-$ mole)

$K_{ij}'$ are friction coefficient in $\left(\frac{\text{joule-sec}}{\text{cm}^5}\right)$

$\underline{v}_i, \underline{v}_j$ are macroscopic velocities in $\left(\frac{\text{cm}}{\text{sec}}\right)$.

Laity[18,19] and Klemm[20,21] have used similar equations for molten salts, and Onsager[22] has suggested a similar equation for aqueous solutions. This equation has also been applied to aqueous solutions, in investigations of the potential of cells with liquid junction.[23] The concentration dependence of each $K_{ij}$ is largely accounted for by the relationship

$$K_{ij} = RT \frac{C_i C_j}{C_T D_{ij}}$$

where $C_T$ is the total concentration

$$C_T = \sum_i C_i \quad ,$$

and the $D_{ij}$'s are diffusion coefficients for binary interactions. Also, $K_{ij} = K_{ji}$.

For a system of n components, there are (n-1) independent equations of the form of (1). The system of interest here is composed of $K^+$, $Cl^-$, and $Ti^{+2}$ ions.[24] If we choose $Ti^{+2}$ and $Cl^-$ to be the two independent species, we may write

$$C_1 \nabla \mu_1 = K_{12}(\underline{v}_2 - \underline{v}_1) + K_{13}(\underline{v}_3 - \underline{v}_1) \qquad (2)$$

$$C_3 \nabla \mu_1 = K_{13}(\underline{v}_1 - \underline{v}_3) + K_{23}(\underline{v}_2 - \underline{v}_3) \qquad (3)$$

and a similar equation for species 2 is redundant because of the Gibbs-Duhem relation. Here species 1 is $Ti^{+2}$, species 2 is $K^+$, and species 3 is $Cl^-$. The other relationships which we need are the electroneutrality equation

$$\sum_i z_i C_i = 0$$

and the current equation

$$\frac{\underline{i}}{F} = \sum_i z_i \, C_i \underline{v}_i .$$

From thermodynamics

$$\mu_A = \nu_1^A \mu_1 + \nu_3^A \mu_3$$

and

$$\mu_B = \nu_2^B \mu_2 + \nu_3^B \mu_3$$

where $\mu_A$ and $\mu_B$ are the chemical potential of $TiCl_2$ and KCl respectively.

We are interested in a steady-state situation where solid $K_2TiCl_4$ is just precipitated by dissolution of Ti metal. We are interested in the current level at which precipitation just begins. At this current level, which we shall call the solubility current, the flux of $K^+$ and $Cl^-$ first become non-zero. That is, below the solubility point, flux of both are zero, and the flux of $Ti^{+2}$ is wholly responsible for the current at the surface.

The equations (2) and (3) may be inverted[23] to give the fluxes in terms of the driving forces. This inversion gives

$$\underline{v}_1 - \underline{v}^* = L_1^A \nabla\mu_A + L_1^i \underline{i} \qquad (4)$$

$$\underline{v}_3 - \underline{v}^* = L_3^A \nabla\mu_A + L_3^i \underline{i} \qquad (5)$$

where the molar-average velocity $\underline{v}^*$ $(= \frac{1}{C_T} \sum_i C_i \underline{v}_i)$ has been chosen as the reference velocity. An equation can also be written for species 2,

$$\underline{v}_2 - \underline{v}^* = - (C_1 L_1^A + C_3 L_3^A) \nabla \mu_A$$

$$- (C_1 L_1^i + C_3 L_3^i)\, \underline{i} \quad .$$

The gradient of chemical potential of $A(TiCl_2)$ and the current have been chosen as the two independent driving forces although other choices are possible. The coefficients may be shown to have the following relationships to the $K_{ij}$'s, i.e.,

$$L_1^A = \frac{-(z_3 - z_2)C_3}{\frac{\nu_1^A}{z_3} D}$$

$$L_3^A = \frac{(z_1 - z_2)C_1}{\frac{\nu_1^A}{z_3} D}$$

$$L_1^i = - \frac{\left\{ \frac{K_{12}}{C_1 C_2} z_3 C_3 + \frac{K_{13} z_2 C_2}{C_1 C_3} + \frac{K_{23} z_1 (C_1 - C_T)}{C_2 C_3} \right\}}{F D}$$

$$L_3^i = - \frac{\left\{ \frac{K_{12} z_3 (C_1 + C_2)}{C_1 C_2} + \frac{K_{13} z_2 C_2}{C_1 C_3} + \frac{K_{23} z_1 C_1}{C_2 C_3} \right\}}{F D}$$

where

$$D = C_T \left\{ \frac{K_{12}}{C_1 C_2} z_3^2 C_3 + \frac{K_{13}}{C_1 C_3} z_2^2 C_2 + \frac{K_{23}}{C_2 C_3} z_1^2 C_1 \right\} .$$

Also, the coefficients $L_1^i$ and $L_3^i$ are related to the transference numbers as

$$t_1^* = z_1 C_1 F L_1^i$$

$$t_3^* = z_3 C_3 F L_3^i$$

where the superscript $^*$ indicates that these are transference numbers where the molar-average velocity is the reference velocity. A different choice of the reference velocity (such as the mass-average velocity) would lead to different transference numbers.

From the current equation,

$$\frac{i}{F} = \sum_i z_i C_i \underline{v}_i = z_i C_1 \underline{v}_1$$

where we have used the boundary conditions discussed above (i.e., $v_2=v_3=0$). Therefore,

$$C_1 \underline{v}_1 = C_1 L_1^A \nabla \mu_A + C_1 L_1^i \underline{i} + C_1 \underline{v}^*$$

$$= C_1 L_1^A \nabla \mu_A + C_1 L_1^i \underline{i} + \frac{C_1}{C_T} (C_1 \underline{v}_1)$$

which leads to

$$\frac{i}{F}\left[1 - z_1C_1FL_1^i - \frac{C_1}{C_T}\right] = z_1C_1L_1^A \nabla\mu_A \qquad (6).$$

This gives the desired connection between the current and the gradient of the chemical potential of A. Rearranging,

$$\frac{i}{F} = \frac{z_1C_1L_1^A \nabla\mu_A}{\left[1-t_1^* - \frac{C_1}{C_T}\right]}$$

and introducing the definitions for $L_1^A$ and $t_1^*$,

$$\frac{i}{F} = \frac{z_1C_T\left[-(z_3-z_2)C_3\right]\nabla\mu_A}{\left(\frac{C_T}{C_1} - 1\right)D - \frac{C_T}{C_1}\left\{-\frac{z_1\nu_1^AC_1}{z_3}\left(\frac{K_{12}}{C_1C_2}^{z_3C_3} + \frac{K_{13}}{C_1C_3}^{z_2C_2} + \frac{K_{23}}{C_2C_3}^{z_1(C_1-C_T)}\right)\right\}}$$

$$= -\frac{z_1C_1^2\nabla\mu_A}{K_{12}\nu_1^A - K_{13}\nu_1^A\frac{z_2C_2}{z_3C_3}}$$

$$= -\frac{z_1C_1^2\left(\frac{\nu^A}{\nu_1^A}\right)\frac{RT}{C_A}\left[1 + \frac{d\ell nf_A}{d\ell nC_A}\right]\nabla C_A}{K_{12} - K_{13}\frac{z_2C_2}{z_3C_3}}$$

where $f_A$ is the mean molar activity coefficient of A. By introducing the definition for the $K_{ij}$'s,

$$\frac{i}{F} = - \frac{z_1 \nu^A z_3 D \nabla C_A}{(z_3 - z_2)} \qquad (7)$$

where

$$D = \frac{\frac{C_T}{C_2}(z_3 - z_2) D_{12} D_{13}}{z_3 D_{13} - z_2 D_{12}} \left[ 1 + \frac{d\ell n f_A}{d\ell n C_A} \right] .$$

If we assume that D is independent of concentration, the equation may be integrated. The boundary condition that the concentration of A goes to zero at some distance $\delta$ from the surface leads to the equation,

$$C_A + \frac{i}{F} \frac{(z_2 - z_3)}{z_1 z_3 \nu^A D} (y - \delta) \qquad (8)$$

The concentration of A at the surface is fixed by the assumption of precipitation of $K_2TiCl_4$, i.e.,

$$C_A^\circ = - \frac{i\delta}{F} \frac{(z_2 - z_3)}{z_1 z_3 \nu^A D} \qquad (9)$$

By assuming that the melt in contact with the solid is of the same composition as the solid, and using the density of molten Kcl as the density of the melt,

$$C_A^\circ = 5.6 \times 10^{-3} \text{ gms}/_{\text{cm}^3}$$

we may now calculate the current necessary to just precipitate the solid from (9). We assume

$$D = 10^{-5} \text{ cm}^2/\text{sec}$$
$$F = 10^5 \text{ coulombs}/_{\text{equivalent}}$$
$$\delta = 10^{-1} \text{ cm}$$

and use

$$z_1 = 2$$
$$z_2 = 1$$
$$z_3 = -1$$
$$\gamma^A = 3$$

to obtain

$$\underline{i} = 168 \text{ mA}/_{\text{cm}^2} \qquad (10)$$

## APPENDIX 2

Tests have been run in $Al\ Cl_3$ (64 mol %) - Na $Cl$ (20 mol %) - K$Cl$ (16 mol %) melts at 120°C. The melt was purified by contacting it with aluminum powder for several days. The resulting liquid was colored slightly yellow - indicative of some remaining iron contamination. Cyclic voltammograms of the melt revealed an anodic peak at +400 mV vs. the $Al$ reference electrode which is the appropriate voltage for ferrous ion oxidation. No other peaks were obtained between +400 and +1600 mV. The melt was handled only in the dry box.

The tests were largely unsuccessful in that it was not possible to cathodically protect the specimen. Cracks propagated at $3 \times 10^{-3}$ cm/sec for K levels between 17 and 24 ksi $\sqrt{in}$, and were independent of potential between -300 mV and +300 mV, both with respect to an aluminum reference electrode. The inability to protect the specimen cathodically is consistent with the potential series reported by Yntema, et.al. (25), i.e., Ti is reported to be more negative than that of $Al$ in $Al\ Cl_3$-NaCl-K$Cl$ melts (and thus not measurable). Further testing in this melt will be fruitful only if a technique may be found to protect the specimen against such propagation until observation can be made.

Nomenclature

| | |
|---|---|
| $C_{H^+}$ | concentration of hydrogen ions (moles/$cm^3$) |
| $\underline{i}$ | current density (A/$cm^2$) |
| $\underline{i}_{lim}$ | diffusion-limited current (A/$cm^2$) |
| F | Faraday's constant (coulombs/equivalent) |
| $D_{H^+}$ | diffusion coefficient of hydrogen ions ($Cm^2$/sec) |
| $\theta_1$ | crack angle |
| K | stress intensity (ksi $\sqrt{in}$ ) |
| $K_{eq}$ | equilibrium constant |
| $\nabla u_i$ | gradient of electrochemical potential of species i (calories/cm-mole) |
| $K_{ij}$ | friction coefficient (joule-sec/$cm^5$) |
| $U_i$ | macroscopic velocity of species i (cm/sec) |
| R | gas constant (calories/°K-mole) |
| T | temperature (°K) |
| $D_{ij}$ | diffusion coefficient for binary interaction |
| $z_i$ | charge number of ionic species (1/mole) |
| $\nu_i$ | number of rations or anions produced by dissociation of one mole of electrolyte |
| $\underline{V}^*$ | molar average velocity (cm/sec) |
| $C_T$ | total concentration (moles/$cm^3$) |
| $t_i^*$ | transference number of i with respect to the molar average velocity |

REFERENCES

[1] Logan, H.L., Proceedings of Conference on Fundamental Aspects of Stress Corrosion Cracking, R.W. Staehle, A.J. Forty and D. Von Rooyen, Eds., p. 662 (1967).

[2] Speidel, M.O., Paper to be presented at the International Conference on "Theories of Stress Corrosion Cracking in Alloys," Portugal, 1971.

[3] Rhodes, P.R., *Corrosion* 25, 462 (1969).

[4] Blackburn, M.J., and Smyrl, W.H., Paper presented at Spring, 1970, meeting of the Electrochemical Society, Abstract 281.

[5] Plambeck, J.A., *J. Chem. Engr. Data* 12, 77 (1967).

[6] Blackburn, M.J., Feeney, J.A., and Beck, T.R., Monograph Review of the State-of-the-Art of SCC in High Strength Alloys. To be published.

[7] Stress Corrosion Cracking of Titanium, American Society For Testing and Materials, Special Technical Publication 397, (1966).

[8] Burkhard, W.J. and Corbett, J.D., *J. Amer. Chem. Soc.* 79, 6361 (1957).

[9] Smith, Diane, The Boeing Company, to be published.

[10] Hildebrand, F.B., Advanced Calculus for Applications, Prentice-Hall, Inc., Englewood Cliffs, New Jersey, 1962, Chapter 9.

[11] Wagner, C., *J. Electrochem. Soc.* 98, 116 (1951).

[12] Cheh, H.Y., *J. Electrochem. Soc.* 117, 609 (1970).

(13) Harrison, J. D., and Wagner, C., *Acta Metallurgica* 7, 722 (1959).

(14) Despic, A. R., Raicheff, R. G., and Bockris, J. O'M., *J. Chem. Phys.* 49, 926 (1968).

(15) Aircraft Designer's Handbook for Titanium and Titanium Alloys. Technical Report AFML-TR-67-142.

(16) Gray, H. R., and Johnson, J. R., Hot-Salt Stress Corrosion of a Titanium Alloy in a Dynamic Air Environment," *Metallurgical Transactions*, Vol. 1, 1970, p. 3101.

(17) Newman, J., *Advan. Electrochem. Electrochem. Eng.*, 5, 87 (1967).

(18) Laity, R. W., *J. Phys. Chem.*, 63, 80 (1959).

(19) Laity, R. W., *J. Chem. Phys.*, 30, 682 (1959).

(20) Klemm, A., *Z. Naturforsch.*, 8a, 397 (1953).

(21) Klemm, A., *Z. Naturforsch.*, 17a, 805 (1962).

(22) Onsager, L., *Ann. N. Y. Acad. Sci.*, 46, 241 (1945).

(23) Smyrl, W. H., and Newman, J., *J. Phys. Chem.*, 72, 4660 (1968).

(24) Ehrlich, P., and Kühnl, H., *Z. Anorg. u. allgem. Chem.*, 292, 148 (1957; and Ehrlich, P., and Schmitt, R., *Z. Anorg. u. allgem. Chem.*, 308, 91 (1961).

(25) Verdieck, R. G., and Yntema, L. F., *J. Phys. Chem.*, 48, 268 (1944).

# 4.4 Electrochemistry of Freshly-Generated Titanium Surfaces, I. Scraped-Rotating-Disk Experiments

T. R. Beck

Boeing Scientific Research Laboratories
Seattle, Washington 98124

## ABSTRACT

Experiments were conducted in which a rotating disk of titanium was scraped with a sapphire cutter in HCl solution. The amount of titanium going into solution determined chemically and by oxidation of $Ti^{3+}$ to Ti(IV) at a gold ring accounted for a large fraction of the anodic current to the scraped surface. The data are consistent with a revised potential - pH diagram taking into account the simultaneous formation of $Ti^{3+}$ and a mestastable passivating oxide. Oxidation of $Ti^{3+}$ to Ti(IV) on gold was highly irreversible even in 6M HCl. Ring-disk transient behavior was analyzed.

## INTRODUCTION

A mass-transport-kinetic (MTK) model developed to describe the electrochemical events in a propagating stress corrosion crack[1] required that kinetic data for newly generated surfaces of titanium be determined. New surfaces of titanium were generated by fast fracture under potentiostatic conditions in aqueous solutions[2] and current transients were interpreted in terms hydrogen ion reduction and formation of oxide. During the development of the MTK model it became

evident that these two reactions were insufficient to explain events in a stress corrosion crack and the simultaneous formation of $Ti^{3+}$ ion was suspected.[1]

The purpose of the work described in the present papers was to determine if $Ti^{3+}$ is formed simultaneously with oxide and to determine the kinetics of formation of $Ti^{3+}$ and the initial passivating oxide layer. The first paper describes identification and quantitative determination of $Ti^{3+}$ in scraped rotating disk experiments. The second paper is concerned with fast fracture experiments in aqueous solutions and fitting of models for simultaneous hydrogen ion reduction and formation of $Ti^{3+}$ and titanium oxide to the data.

Electrochemistry of freshly generated metal surfaces has received increasing attention in recent years. Andersen and Eyring[3] in a series of papers describe a continuous scraping technique using a sapphire bit to determine the point to zero charge of noble metals. Titanium and aluminum were too reactive to determine the point of zero charge by this method. Hagyard and Earl[4] studied reactions of new aluminum surfaces generated by rapid shear with a ruby cutter in KCl solution and presented some kinetic interpretations. Tomashov and Vershinina[5] abraded a number of metals with a corundum grinding wheel and determined relative reactivity to unabraded specimens for hydrogen ion and oxygen reduction and for metal dissolution. Anodic current densities for titanium were observed to increase by 3-4 orders of magnitude by scraping. They attributed the increased current to dissolution and to repassivation, although they made no quantitative separation and it is doubtful that a separation could be made for their surface condition.

Numerous studies[6] have been made of current transients with stretched wires which presumably crack or thin the passivating oxide layers leading to a repassivation, but only qualitative interpretations have been made.

## EXPERIMENTAL

Two sets of experiments were conducted for the purpose of determining the presence and the amount of soluble $Ti^{3+}$ formed in parallel with formation of oxide on new titanium surfaces in acid solution. The first was with a rotating titanium disk that was scraped with a sapphire cutting tool and the soluble titanium was determined colorimetrically using the hydrogen peroxide method[7]. The second set of experiments was with a titanium disk that was scraped with a sapphire cutter and soluble $Ti^{3+}$ formed was determined by oxidation to $TiO^{2+}$ at a gold ring.

### *Rotating Disk Experiments*

The geometry of the rotating disk experiments is illustrated in Figure 1. The 99.9% purity iodide-titanium rod (A. D. Mackay, New York) was bored out so that the area of the scraped face would not change as titanium was removed. The outside diameter was 0.6 cm and the inside diameter 0.4 cm. The Teflon cell was 2.5 cm inside diameter and 2.5 cm deep. A minimum volume of electrolyte ($\sim$20$m\ell$) was used so that a measurable concentration could be built up with a reasonable amount of scraping on the titanium. A 0.38 cm diameter sapphire rod was ground on the end to a square-nose tool with a 0.20 cm wide cutting edge, a negative rake angle of 17 degrees and a relief angle of 14 degrees. It was bonded in a hole in the aluminum base plate with

epoxy resin. A drill-press table holding the cell and cutter was equipped with a motor drive for advancing the cutter into the rotating titanium tube at various controlled rates. A Wenking Model 6379 TR potentiostat was used to hold the titanium tube at constant potential in respect to a saturated calomel reference electrode. All potentials were measured in respect to the saturated calomel electrode or silver/silver chloride electrode and converted to the standard hydrogen electrode scale by adding 0.24 volts or 0.12 volts respectively. (The Ag/AgCl electrode in 6 M HCl was measured to be -118 mV to SCE.)

Soluble titanium was determined by the hydrogen peroxide method described in Kolthoff and Elving[7] using a Cary Model-14 Recording Spectrophotometer. A calibration curve was made using Bakers reagent grade $TiO_2$ as standard. In the determinations, the soluble $Ti^{3+}$ was oxidized to $TiO^{2+}$ by the hydrogen peroxide to form a yellow-colored complex with the excess of hydrogen peroxide.

At the completion of each run the electrolyte was immediately poured out of the cell into a graduated cylinder, 3 $cm^3$ of 3% $H_2O_2$ was added and the total volume recorded. A portion of this solution was examined in the spectraphotometer. Rapid transfer of the solution was necessary because the metal cuttings continued to react as evidenced by visible hydrogen evolution. The cuttings had a higher reactivity as compared to massive titanium probably due to cold working and increased surface area. The solution prior to $H_2O_2$ addition had a light violet color indicative of $Ti^{3+}$.

*Ring Disk Experiments*

The design of the ring-disk electrode is shown in Figure 2. The

gold ring and titanium rod with exposed end forming the disk were mounted in a Teflon body, in turn fastened to the rotating shaft through a screw fitting. Disk material was iodide titanium as in the scraped disk experiments and the ring was gold of 99.9% purity. Leads from the disk and ring were connected through a Huttinger Baldwin Messtechnik SK-6 slip-ring assembly to the external circuit. Four slip rings were connected to the disk and two slip rings were connected to the gold ring.

The electrode was immersed in electrolyte filled to 6 cm depth in a square Plexiglas cell with internal dimensions 10 x 10 x 8 cm. The disk was potentiostated, the saturated calomel reference electrode at the edge of the Teflon body and the platinum counter electrode at the side of the cell as indicated in Figure 3. A silver sheet anodized in chloride solution with 3 1/2 cm by 18 cm immersed area (per side) was used as reference and counter electrode for the gold ring. A bias voltage was applied to the gold ring with a 100 ohm potentiometer across two series mercury cells, and a 10 ohm shunt was used for measuring current. The disk was scraped by a sapphire cutter of similar shape to the foregoing, bonded in a titanium holder attached to the bottom of the cell.

Before the scraping experiment could be interpreted a number of preliminary experiments and calibrations were made. These included measurement of polarization curves for oxidaticn of $Ti^{3+}$ on gold, determination of ring efficiency for oxidation of $Ti^{3+}$ formed by reduction of Ti(IV) from solution on disk, determination of the ring efficiency by reduction of iodine generated at the disk, determination

of ring current for hydrogen generated at the disk and study of ring-disk transients.

1. Polorization curve for $Ti^{3+}/Ti(IV)$ on gold

The irreversibility of the $Ti^{3+}/TiO^{2+}$ couple in polarography on a mercury surface is well known[8]. A similar irreversibility was observed in the present work on gold and platinum electrodes. The couple is so irreversible that no oxidation current was measured with a 0.1M $TiCl_3$ solution between the potentials of hydrogen and oxygen evolution, whereas the standard reversible potential of the couple given by Latimer[9] is about + 0.1 V.

In agreement with the polarographic work[8], an oxidation current was found with a stationary gold electrode in a strongly acid solution of 0.1M $TiCl_3$ in 6M HCl as indicated in Figure 4. Curve A is for 6M HCl and the anodic current at $\sim$+0.9V represents dissolution of gold. According to Latimer[9] the standard potential for formation of the $AuCl_4^-$ complex is + 1.0 volt. The equilibrium potential should be approximately 60 mV less positive in 6M HCl and further with no gold in solution. The cathodic current at 0 V is presumed to be for hydrogen ion reduction. The anodic part of curve B is for oxidation of $Ti^{3+}$. At a potential above + 0.5V the current becomes limited at least in part by mass transport in solution as evidenced by an increase in current when the electrolyte was stirred. The steady-state limiting current density, however, was $\sim 2 \times 10^{-4}$ Amp/cm$^2$ compared to a calculated value of $2 \times 10^{-3}$ Amp/cm$^2$ for a diffusivity of $10^{-5}$ cm$^2$/sec for $Ti^{3+}$ and a diffusion layer thickness of $5 \times 10^{-2}$ cm for a one-electron reaction. It would appear that there remains a high degree of irreversibility in spite of the high concen-

tration of HCl. The irreversibility for oxidation of $Ti^{3+}$ is also manifested in the small increase in current with potential up to 0.5V. The reversible potential for the $Ti^{3+}/TiO^{2+}$ couple appears to be between 0.1 and 0.18V in approximate agreement with the value of 0.1V from Latimer[9] but the value is influenced to some extent by a mixed potential resulting from hydrogen ion reduction.

2. Ring efficiency for oxidation of $Ti^{3+}$

The efficiency of the ring for oxidation of $Ti^{3+}$ produced at the disk was determined by reducing $TiO^{2+}$ from solution on the disk and reoxidizing it at the ring. The electrolyte was approximately 0.4 M $TiO^{2+}$ in 6 M HCl, produced by dissolving Bakers reagent-grade $TiCl_4$ in concentrated HCl and diluting the HCl to 6M. The titanium disk was held at 0 V for reduction of $TiO^{2+}$ and the gold ring potential was varied from 0.2 to 0.9V. Hydrogen overvoltage is greater on titanium than on gold so essentially all of the current to the disk at 0 V went to reduction of $TiO^{2+}$.

Efficiency of $Ti^{3+}$ oxidation versus potential at the ring is given in Table 1 and plotted in Figure 5 for a rotational velocity of 400 RPM. Efficiency was calculated from

$$N = \Delta I_R / I_D \qquad 1.$$

where $\Delta I_R$ is the change in ring current (anodic) and $I_D$ the cathodic disk current for reduction of Ti(IV). It may be noted that a high degree of irreversibility for oxidation of $Ti^{+3}$ at the ring is indicated

by the low efficiencies compared to the value extrapolated from the Albery and Bruckenstein model[10] for the ring and disk dimensions given in Figure 2. Furthermore, at a given ring potential the efficiency decreased with time indicating a poisoning of the surface. The efficiency increased after the ring had been to a potential of 0.92V where gold dissolution occurred and the surface was evidently partially cleaned of the poisoning agent.

3. Ring efficiency for oxidation of hydrogen

The ring current and efficiency were determined for oxidation of hydrogen generated at a negative potential on the disk because of the possibility of error in the scraping experiments due to oxidation at the ring of hydrogen generated on the new surface and on the cuttings. The data shown in Table 2 indicate a very low current and current efficiency at the ring for oxidation of dissolved hydrogen compared to the values for oxidation of $Ti^{3+}$ shown in Table 1. It is therefore assumed that oxidation of dissolved hydrogen can be neglected at the ring in the scraping experiments.

4. Ring efficiency for $I_2$ reduction

Because the ring efficiencies observed in the oxidation of $Ti^{3+}$ were low compared to theory, it was desirable to experimentally check the system with a more reversible couple. The $I^-/I_2$ couple in neutral 0.6M KI solution was used; iodide ion was oxidized to $I_2$ at the disk and the $I_2$ was reduced at the ring. Data are presented in Table 3. The average ring efficiency of 0.44 at 400 RPM is close to the value of 0.46 from Albery and Bruckenstein[10]. Ring efficiency was essentially independent of disk and ring currents and of ring potential from 0.2V

to nearly 0.62V showing that the ring current was indeed under diffusion control. The decrease in efficiency at a ring potential of 0.70V was due to kinetic control of the reduction of $I_2$ near the reversible potential of the $I^-/I_2$ redox couple as indicated by the high background anodic current on the ring. It may be noted that at the same potential the anodic disk current decreased in successive experiments due to the increasing oxide thickness on the titanium. Scraping the disk restored the higher current. Moving the sapphire scraper near the disk but not touching it had a negligible effect on the ring efficiency for these experiments, indicating that the presence of the sapphire tool did not inordinately upset the hydrodynamic conditions. Decrease in ring efficiency with increase in RPM is an anomoly; Levich[11] and Albery and Bruckenstein[10] show that N should be independent of rotation speed.

5. Ring-disk transients

During the scraping experiments it was observed that although a general increase in anodic ring current occurred during scraping, there appeared to be no correlation between current fluctuation peaks on the disk and ring when investigated on an expanded time scale. An explanation is that there was a delay time for transport of $Ti^{3+}$ from disk to ring and that this delay time was variable depending on the radial position of transiently scraped patches of metal on the disk. Measurements made of the transport delay time from disk to ring with the $I_2/I^-$ system were consistent with this hypothesis.

A strip-chart record of disk and ring transient currents accompanying step changes in disk potential in 0.6M KI solution from an essentially zero $I^-$ ion oxidation current to about 0.4 mA is shown in Figure 6.

It may be noted that at the instant the potential was switched on the disk, denoted by $\tau_p$, there was a slight change in the ring current due to a change in IR drop in the solution near the electrode face. There was then a delay time denoted by $\Delta\tau_d$, between this time $\tau_p$, and the onset of change in ring current due to reduction of $I_2$. The latter time was determined by extrapolating the initial-current slope back to the intersection with the pre-potential-step current. (That $\Delta\tau_d$ is approximately equal to the time difference in the two pen positions is a coincidence in this experiment.) The same value of $\Delta\tau_d$ was found for the potential step to the zero disk current and from zero to a finite disk current.

A plot of delay time versus the period of revolution for three speeds in Figure 7 shows a linear relation passing through the origin. The delay time at 400 RPM, at which most of the ring-disk scraping experiments were done, is about 0.25 sec. This is for a gap between ring and disk of 0.05 cm (Figure 2). The radial distance between the boundaries of the scraped zone on the disk and the inner radius of the ring was in the range of about 0.1 to 0.25 cm. Assuming constant radial velocity across this portion, the disk would therefore give delay times of 0.5 to 1.25 seconds, which would explain the lack of correlation of ring and disk current peaks at a high resolution of time. The actual delay times would be longer than these because radial velocity of solution is a function of radius as discussed in the Appendix.

## RESULTS AND DISCUSSION

### *Thermodynamics*

A review of the thermodynamics of the titanium-water system is

appropriate before discussing the experimental results. The potential - pH diagram gives a convenient display of fields of thermodynamic stability for the various species.

The potential - pH diagram of Pourbaix[12] for titanium is modified here in light of recent data. A communication by Pourbaix[13] points out that titanium hydride equilibria should also be considered. Using a free energy of formation for $TiH_2$ of -25 kcal/mole[14] gives for the reaction

$$Ti + 2H^+ + 2e \rightarrow TiH_2; \quad \phi_e = 0.54 - 0.059\ pH.$$

Titanium hydride should therefore form spontaneously on new titanium surfaces in aqueous solutions. Further, the data and analysis of Oliver and Ross[15] show that the standard potential for the $Ti^{3+}/Ti^{2+}$ couple is -2.3V rather than -0.37V as used by Latimer[9] and by Pourbaix[12]. Such a negative potential for this couple would require that titanium be oxidized directly to $Ti^{3+}$ instead of to $Ti^{2+}$,

$$Ti \rightarrow Ti^{3+} + 3e, \text{ and } \phi_e = -1.21,$$

for a free energy of formation of -83.6 kcal[9] for $Ti^{3+}$. Oxidation of titanium hydride would give

$$TiH_2 \rightarrow Ti^{3+} + 2H^+ + 5e; \quad \phi_e = -0.51 - 0.024\ pH.$$

The phase boundary between hydride and $TiO_2$ (rutile) is

$$TiH_2 + 2H_2O \rightarrow TiO_2 + 6H^+ + 6e; \quad \phi_e = -0.47 - 0.059\ pH$$

for a free energy of formation of -203.8 kcal for $TiO_2$[9]. This turns out to be above the $Ti_2O_3/TiO$ and $TiO_2/Ti_2O_3$ equilibrium lines[12], so the $TiO_2/TiH_2$ equilibrium prevails. The phase boundary between $Ti^{3+}$ and $TiO_2$,

$$Ti^{3+} + 2H_2O \rightarrow TiO_2 + 4H^+ + e; \quad \phi_e = -0.30 - 0.236\ pH$$

completes the basic diagram as illustrated in Figure 8a. Similar considerations lead to the diagram for the hydrated oxides in Figure 8b. The dashed lines a and b are for the reversible hydrogen and oxygen electrode respectively[12].

Under nonequilibrium conditions (as for freshly generated titanium surfaces) metastable phases may form when the kinetics for their formation is favorable but the kinetics for their reaction to the stable phase in that field is slow. An example of such a metastable phase field boundary that will be considered in the oxidation of freshly generated titanium surfaces is:

$$Ti + 2H_2O \rightarrow TiO_2 + 4H^+ + 4e; \quad \phi_e = -0.98 - 0.059\ pH$$

The $Ti^{3+}/Ti$ equilibrium is also metastable for a fresh titanium surface. These two equilibria for the bare titanium surface are illustrated in Figures 8a and b. The $TiO^{++}/Ti^{3+}$ equilibrium[12] has a range of stability in strongly acid solutions for the hydrated oxide system (Figure 8b) but is completely metastable for the anhydrous oxide system (Figure 8a).

The significance of the modified potential - pH diagrams to the present experiments is as follows: 1. At a mixed potential for new titanium surfaces in acid solution of $\sim -0.6V$, $Ti^{3+}$, $TiO_2$ and $TiH_2$ should form simultaneously. Experimental results for scraped titanium surfaces in this paper and for fractured surfaces in the following paper will be interpreted on this basis. 2. At the $TiO^{++}/Ti^{3+}$ equilibrium potential $TiO^{++}$ is metastable in respect to $TiO_2$. The high degree of irreversibility for this couple and the poisoning of the gold electrode surface noted in Figures 4 and 5 could therefore be attributed to an

insulating layer of $TiO_2$ being formed on the surface.

*Rotating Disk Experiments*

Data for the scraped rotating disk experiments are given in Table 4. The weight of metal that would be dissolved if all of the charge passed produced $Ti^{3+}$ is $W_1$. The weight of metal in solution corresponding to the spectrophotometric analysis is $W_2$. It may be noted in all cases that the metal pickup was greater than could be accounted for by the anodic current to the new surface, indicating contributions from spontaneous dissolution of the cuttings and the disk surface. After the first run, each was the same length in an effort to give a uniform amount of spontaneous dissolution.

The data on dissolution of titanium are plotted in Figure 9. The dashed curve is based on an assumed constant average spontaneous dissolution of $1.4 \times 10^{-4}$ gm and a linear increase in dissolution of the disk with potential of $0.8 \times 10^{-4}$ gm/V from a mixed potential of - 0.6V.

$$\left(W_1/W_2\right)_{calc.} = \frac{W_1}{W_1+1.4} = \frac{(\phi+0.6)(0.8)}{(\phi+0.6)(0.8)+1.4} \qquad 2.$$

It was concluded from these experiments that a large fraction of the current to a new titanium surface goes to form soluble $Ti^{3+}$ in acid solution but that more sensitive experiments would have to be devised to separate the component of current going to oxide formation.

Before proceeding to the ring-disk experiments some other scraped disk correlations are presented. Measured current versus potential from Table 4 is plotted in Figure 10 and the line drawn through the data was determined in an independent experiment by varying the potential at the same constant advance rate on the cutter.

This current is about 1/6 the value calculated from fast-fracture kinetics data for oxidation of new titanium surface in 12M and 3M HCl

$$I_c = \frac{AQ}{\tau_r} \qquad 3.$$

where A = scraped area of disk (0.16 $cm^2$), $\tau_r$ = time between cuts (0.060 sec at 1000 RPM), and $Q = \int_0^{\tau_r} i d\tau$ determined from the fast fracture kinetics experiments (from Reference 2 and the following paper). It turns out that in the kinetics experiments the current decayed rapidly and became negligible after about 0.015 sec so the value of Q became essentially constant for a given potential. Values of Q found in 12M and 3M HCl at a potential of 0.24V were $7.6 \times 10^{-3}$ and $6.0 \times 10^{-3}$ Coul/$cm^2$ respectively with an average value of $6.8 \times 10^{-3}$ Coul/$cm^2$. The integral also varied linearly with potential, going to zero at the mixed potential of $\sim$-0.6V. The current in the scraping experiments was low compared to Eq. 3 presumably because the depth of cut was small compared to the radius of the cutting edge, resulting in a stick-slip condition which gave only a fraction of bare surface.

The effect of tool advance rate and rotational velocity on current was therefore examined and data are presented in Table 5. The data are correlated in Figure 11 by plotting the fraction of calculated current

$$f = I_M/I_c = \frac{60}{AQ}\left(\frac{I_M}{RPM}\right) \qquad 4.$$

as a function of the depth removed per turn, d = advance rate /RPM. It is seen that f varies as $\sim d^{1/2}$ apparently becoming asymptotic to unity

for a removal depth equal to the ~1μ radius of the cutting edge of the sapphire tool. Values of f less than unity are therefore attributed to stick-slip condition which was also evidenced by audible tool chatter and erratic current.

*Ring-Disk Experiments*

Ring and disk currents for the scraping experiments in 6M HCl are presented in Table 6. Based on the preliminary experiments, it was assumed that the ring current was essentially all for oxidation of $Ti^{3+}$ to $TiO^{2+}$. The equivalent current at the disk to form the $Ti^{3+}$ is therefore

$$I = \frac{3\Delta I_{Ring}}{N} \qquad 5.$$

The ratio of this value to the change in disk current with scraping should give the fraction of the disk current to form soluble $Ti^{+3}$. Some continuous background cathodic current for hydrogen ion reduction occurred at the disk potentials in Table 6, thus the use of $\Delta I_{Disk}$. In the first two experiments shown in Table 6 in which a relatively high tool advance rate was used, it appears that most of the disk current went to soluble $Ti^{3+}$. The value of N used from Figure 5 is very approximate due to the poisoning of the ring so the experimental results are not very precise, but the experiments demonstrated that a large fraction of the current to a new titanium surface in acid solution goes to form soluble $Ti^{3+}$.

In the last three experiments shown in Table 6 a lower but successively increasing tool advance rate was used. The ring current increased more with tool advance rate than the disk current suggesting

that at low tool advance rates $TiO_2$ is scraped off preferentially and most of the current goes to grow more oxide on the thinned oxide. Only a limited number of scraping experiments was conducted with the ring disk system because the disk was damaged and had to be resurfaced after each experiment.

## CONCLUSIONS

The following conclusions are drawn from electrochemical experiments in which a rotating-disk of titanium was scraped by a sapphire cutter in 6 M HCl solution and in which $Ti^{3+}$ was oxidized to Ti(IV) at a gold ring.

1. A large fraction of the current to a scraped titanium surface is accounted for by formation of $Ti^{3+}$.
2. A relatively small charge density effectively passivates the new titanium surface.
3. Oxidation of $Ti^{3+}$ to Ti(IV) on gold is very irreversible.

## NOMENCLATURE

A = area, $cm^2$

d = depth of cut, cm

D = diffusivity, $cm^2/sec$

f = fraction of expected current (Eq. 4), dimensionless

i = current density, $A/cm^2$

I = current, Amps

N = ring efficiency, dimensionless

Q = charge density, $Coul/cm^2$

r = radius, cm

v = velocity, cm/sec

W = weight, gm

y = normal distance from disk, cm

$\delta$ = diffusion layer thickness, cm

$\nu$ = kinematic viscosity, $cm^2/sec$

$\tau$ = time, sec

$\phi$ = potential, Volts

$\omega$ = rotational velocity, $sec^{-1}$

Subscripts

C - calculated

d = delay

D = disk

e = equilibrium

m = mixed potential

M = measured

p = potentiostat

r = rotation, radial

R = ring

## REFERENCES


1. T. R. Beck and E. A. Grens II, J. Electrochem. Soc., 116, 177 (1969).

2. T. R. Beck, J. Electrochem. Soc., 115, 890 (1968).

3. e.g., T. N. Andersen, J. L. Anderson and H. Eyring, J. Phys. Chem. 73, 3562 (1969).

4. T. Hagyard and W. B. Earl, J. Electrochem. Soc., 114, 694 (1967).

5. N. D. Tomashov and L. P. Vershinina, Electrochimica Acta, 15 , 501 (1970).

6. e.g., T. P. Hoar and J. C. Scully, J. Electrochem. Soc., 111, 348 (1964).

7. I. M. Kolthoff and P. J. Elving, "Treatise on Analytical Chemistry," Part II, Vol. 5, pp 51-52, Interscience, New York, 1961.

8. J. J. Lingane and J. M. Kennedy, Analytica Chimica Acta., 15, 294 (1956).

9. W. M. Latimer, "Oxidation Potentials," 2nd Ed., Prentice Hall, Englewood Cliffs, New Jersey, 1952.

10. W. J. Albery and S. Bruckenstein, Trans. Faraday Soc., 62, 1920 (1960).

11. V. G. Levich, "Physicochemical Hydrodynamics," Prentice Hall, Englewood Cliffs, New Jersey, 1962.

12. M. Pourbaix, Atlas of Electrochemical Equilibria," Pergamon Press, New York, 1966.

13. M. Pourbaix, Presentation at CITCE Meeting, Istanbul, September 1967.

14. JANAF Interim Thermochemical Tables, Dow Chemical Co., Midland, Michigan, 1960.

15. J. W. Oliver and R. W. Ross, J. Am. Chem. Soc., 85, 2565 (1963).

# APPENDIX

It is of interest to examine the significance of the ring-disk delay time to the hydrodynamic equations for the rotating disk electrode. It can be shown from Levich[11] that the radial velocity in the solution near the disk can be approximated by

$$v_r = 0.51\ \omega r \left(\frac{\omega}{\nu}\right)^{\frac{1}{2}} y \qquad 6.$$

where $\omega$ = rotational speed, radians/sec; $r$ = radial position on disk where the velocity $v_r$ is determined; $\nu$ = kinematic viscosity; and $y$ = distance into solution normal to disk. Because the radial solution velocity is zero at the disk surface, the delay time is the sum of the time for disk products to diffuse from $r_1$ (Figure 2) to a position in the fluid $y_d$ with finite velocity and be transported from $r_1$ to $r_2$ and finally to diffuse back to the ring at $r_2$. The value of $y_d$ must be between zero and $\delta$, the diffusion layer thickness.

The diffusion layer thickness[11] is given by

$$\delta = 1.61\left(\frac{D}{\nu}\right)^{1/3}\left(\frac{\nu}{\omega}\right)^{\frac{1}{2}} \qquad 7.$$

where $D$ = diffusivity of transported species. The ratio of $y/\delta$ from equations 6 and 7 is

$$y/\delta = \frac{v_r}{(0.82)\ \omega r\left(\frac{D}{\nu}\right)^{1/3}} \qquad 8.$$

The value of $v_r$ is given approximately by

$$v_r \geq \frac{r_2 - r_1}{\Delta\tau_d} \qquad 9.$$

the value of $v_r$ being larger than the right hand side because $\Delta\tau_d$ contains the diffusion times as well as the convection time from $r_1$ to $r_2$ . Empirically it is found from Figure 7 that

$$\Delta\tau_d = 1.60 \left(\frac{60}{RPM}\right) \qquad 10.$$

Letting

$$\omega = 2\pi \left(\frac{RPM}{60}\right) ,$$

$$r \approx \frac{r_2 + r_1}{2}$$

and

$$\left(\frac{D}{\nu}\right)^{1/3} \approx \left(\frac{10^{-5}}{10^{-2}}\right)^{1/3} = 10^{-1}$$

gives

$$\frac{y_d}{\delta} \geq 2.42 \left(\frac{r_2 - r_1}{r_2 + r_1}\right) \qquad 11.$$

which for the dimensions in Figure 2 gives

$$\frac{y_d}{\delta} \geq 0.22 ,$$

a constant, independent of RPM.

## ACKNOWLEDGEMENT

The many helpful discussions with Dr. M. J. Blackburn and Dr. W. H. Smyrl are gratefully acknowledged. Mr. Robert L. Lee conducted many of the experiments. This work was supported by NASA Headquarters Contract NAS 7-489.

| $E_{Ring}$ (Volts SHE) | $I_{Disk}$ (ma) (cathodic) | $\Delta I_{Ring}$ (ma) (Anodic) | N |
|---|---|---|---|
| 0.22 | 3.20 | 0.11 | 0.035 |
| 0.22 | 3.22 | 0.078 | 0.024 |
| 0.22 | 2.55 | 0.050 | 0.020 |
| 0.22 | 3.30 | 0.056 | 0.017 |
| 0.32 | 2.50 | 0.102 | 0.041 |
| 0.32 | 3.00 | 0.112 | 0.037 |
| 0.42 | 3.30 | 0.267 | 0.081 |
| 0.42 | 3.00 | 0.188 | 0.062 |
| 0.52 | 3.00 | 0.373 | 0.124 |
| 0.52 | 3.00 | 0.340 | 0.113 |
| 0.62 | 3.50 | 0.650 | 0.185 |
| 0.72 | 3.50 | 0.950 | 0.272 |
| 0.82 | 3.50 | 1.20 | 0.343 |
| 0.92 | 4.00 | 0.475 | 0.119 |
| 0.72 | 4.00 | 1.55 | 0.388 |
| 0.52 | 4.00 | 1.04 | 0.260 |
| 0.32 | 4.47 | 0.330 | 0.074 |

Table 1

Disk and Ring Current and Ring Efficiency for Oxidation of $Ti^{3+}$ Generated at Disk by Reduction of $TiO^{2+}$ (0.4 M $TiO^{2+}$ in 6 M HCl)

| $I_{Disk}$ (ma) (cathodic) | $\Delta I_{Ring}$ (ma) (anodic) | N |
|---|---|---|
| 140 | 0.07 | 0.0005 |
| 150 | 0.04 | 0.0003 |

Table 2

Ring Efficiency for Oxidation of Hydrogen Generated At Disk (6 M HCl, Ring at +0.62V, Disk at - 1.16V, ~ 1000 RPM)

| RPM | $E_{Disk}$ (V SHE) | $E_{Ring}$ (V SHE) | $I_{Disk}$ (ma) (anodic) | $I_{Ring}$ (ma) (cathodic - anodic +) | $\Delta I_{Ring}$ (ma) (cathodic) | N |
|---|---|---|---|---|---|---|
| 400 | 0.90 | 0.12 | 4.30 | -0.15 | 1.85 | 0.430 |
| 400 | 0.82 | 0.12 | 1.85 | -0.15 | 0.825 | 0.445 |
| 400 | 0.76 | 0.12 | 0.85 | -0.15 | 0.375 | 0.440 |
| | | | | | | 0.438 Avg. |
| 1000 | 0.89 | 0.12 | 3.45 | -0.15 | 1.44 | 0.417 |
| 1000 | 0.84 | 0.12 | 1.95 | -0.15 | 0.835 | 0.428 |
| 1000 | 0.79 | 0.12 | 1.05 | -0.15 | 0.440 | 0.418 |
| | | | | | | 0.421 Avg. |
| 100 | 0.90 | 0.12 | 3.16 | -0.15 | 1.49 | 0.471 |
| 100 | 0.84 | 0.12 | 1.70 | -0.15 | 0.82 | 0.482 |
| 100 | 0.79 | 0.12 | 0.95 | -0.15 | 0.45 | 0.474 |
| | | | | | | 0.476 Avg. |
| 400 | 0.90 | 0.02 | 2.75 | -0.78 | 1.21 | 0.440 |
| 400 | 0.84 | 0.02 | 1.50 | -0.78 | 0.675 | 0.450 |
| | | | | | | 0.445 Avg. |
| 400 | 0.90 | 0.32 | 2.50 | +0.04 | 1.075 | 0.430 |
| 400 | 0.84 | 0.32 | 1.40 | +0.04 | 0.625 | 0.445 |
| | | | | | | 0.438 Avg. |
| 400 | 0.90 | 0.42 | 2.43 | +0.07 | 1.075 | 0.442 |
| 400 | 0.90 | 0.62 | 2.32 | +0.35 | 1.00 | 0.431 |
| 400 | 0.90 | 0.70 | 2.27 | +2.38 | 0.725 | 0.320 |

Table 3.

Calibration of Ring Efficiency in 0.6M KI Solution

| Run | 1 | 2 | 3 | 4 | 5 |
|---|---|---|---|---|---|
| Potential (V) | 0.24 | 0.24 | 1.24 | 0.C. (-0.56 to -0.64) | -0.61 |
| Time (sec) | 64 | 124 | 124 | 125 | 125 |
| Avg. Current (ma) | 4.08 | 4.05 | 5.64 | 0 | Cathodic |
| Q (amp sec) | 0.261 | 0.502 | 0.700 | 0 | - |
| $W_1$ (gm x $10^4$) | 0.43 | 0.83 | 1.16 | - | - |
| Soln. vol. ($cm^3$) | 20.0 | 23.0 | 19.5 | 16.8 | 20.3 |
| ppm $Ti^{+4}$ | 10. | 11.4 | 11.1 | 6.3 | 9.0 |
| $W_2$ (gm x $10^4$) | 2.0 | 2.62 | 2.17 | 1.06 | 1.83 |
| $W_2 - W_1$ (gm x $10^4$) | 1.57 | 1.79 | 1.01 | 1.06 | 1.83 |
| Ratio $W_1:W_2$ | 0.274 | 0.316 | 0.535 | 0 | 0 |

Table 4

Data for Scraped Ti Disk Experiments (~1000 RPM, Tool Advance Rate ~ 50 μ/min)

| RPM | Advance rate (μ/min) | Disk current (ma) | d (μ/rev) | f |
|---|---|---|---|---|
| 400 | 90 | 3.7 | 0.225 | 0.51 |
| | 90 | 4.0 | 0.225 | 0.55 |
| | 600 | 7.5 | 1.50 | 1.03 |
| 1000 | 50 | 3.5 | 0.050 | 0.19 |
| | 85 | 6.0 | 0.085 | 0.33 |
| | 85 | 4.9 | 0.085 | 0.27 |
| | 125 | 6.1 | 0.125 | 0.34 |
| | 125 | 5.0 | 0.125 | 0.28 |
| | 310 | 7.3 | 0.310 | 0.40 |
| 3000 | 85 | 10.0 | 0.028 | 0.18 |

Table 5

Effect of RPM and Tool Advance Rate on Disk Current (6M HCl, $\phi_D = 0.24V$)

| $E_{Disk}$ (V SHE) | $E_{Ring}$ (V SHE) | $\Delta I_{Disk}$ (ma) (anodic) | $\Delta I_{Ring}$ (ma) (anodic) | N (Figure 9) | $\frac{3\Delta I_{Ring}}{N}$ (ma) | $\frac{3\Delta I_{Ring}}{N\Delta I_{Disk}}$ |
|---|---|---|---|---|---|---|
| -0.26 | 0.82 | 9.5 | 0.85 | 0.35 | 7.3 | 0.77 |
| -0.26 | 0.82 | 6.5 | 0.84 | 0.35 | 7.2 | 1.11 |
| | | | | | | 0.94 Avg. |
| -0.06 | 0.62 | 8 | 0.05 | 0.19 | 0.8 | 0.10 |
| -0.06 | 0.62 | 12 | 0.15 | 0.19 | 2.4 | 0.20 |
| -0.06 | 0.62 | 18 | 0.6 | 0.19 | 9.5 | 0.53 |

Table 6

Ring and Disk Currents in Scraping Experiments (6 M HCl, 400 RPM)

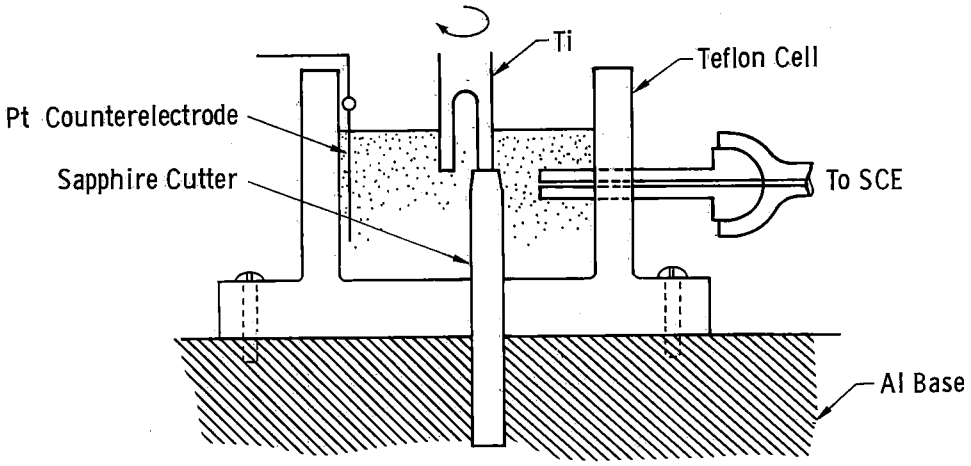


Figure 1

Scraped titanium disk experiment

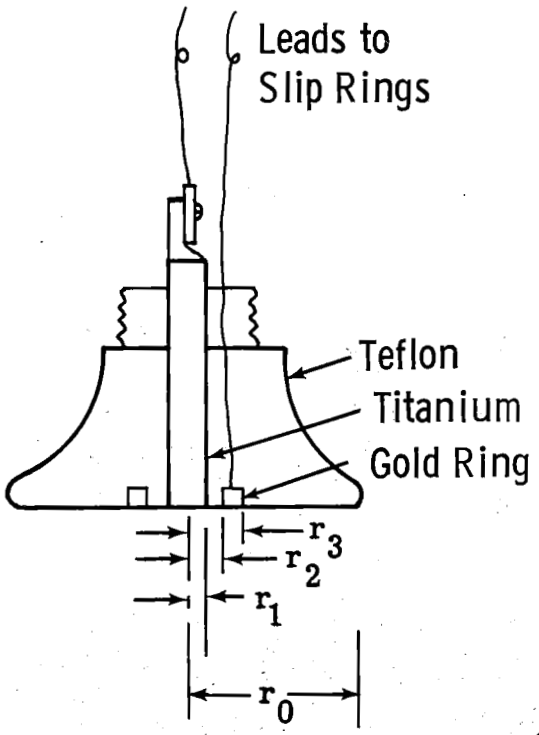


$r_1 = 0.25$ cm

$r_2 = 0.30$ cm

$r_3 = 0.45$ cm

$r_0 = 2.0$ cm

Figure 2

Design of ring-disk electrode

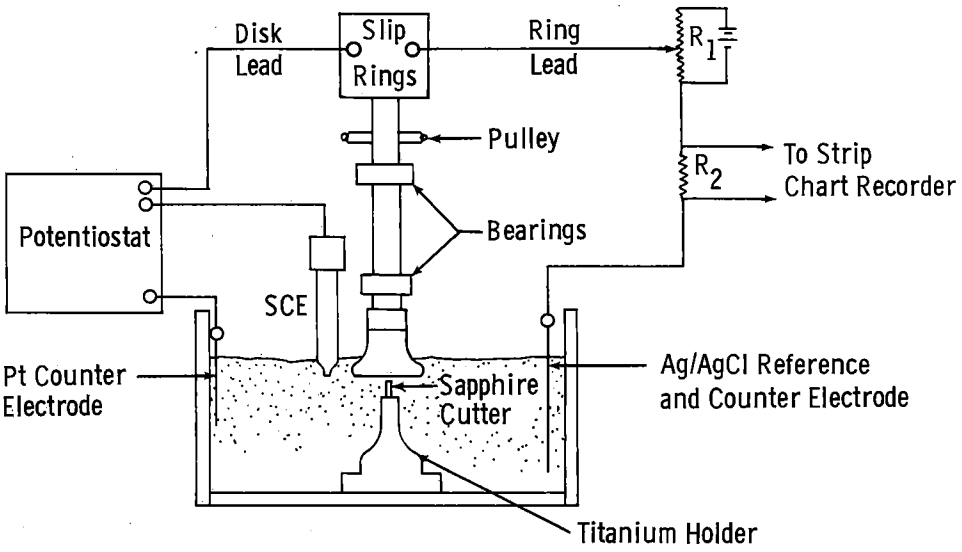


Figure 3

Physical arrangement of ring-disk cell and electrical circuits

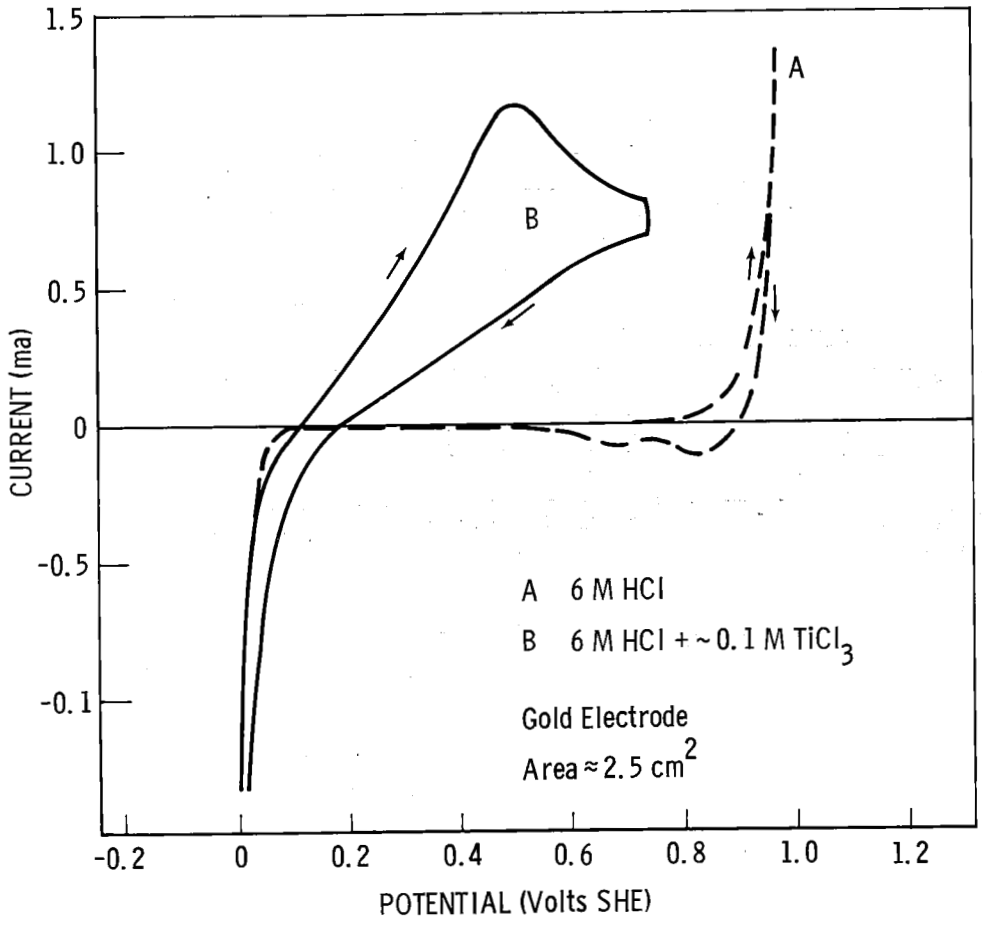


Figure 4

Polarization curve of gold electrode in 6M HCl and in 6M HCl + 0.1M $TiCl_3$ (sweep speed 624 mV/min.)

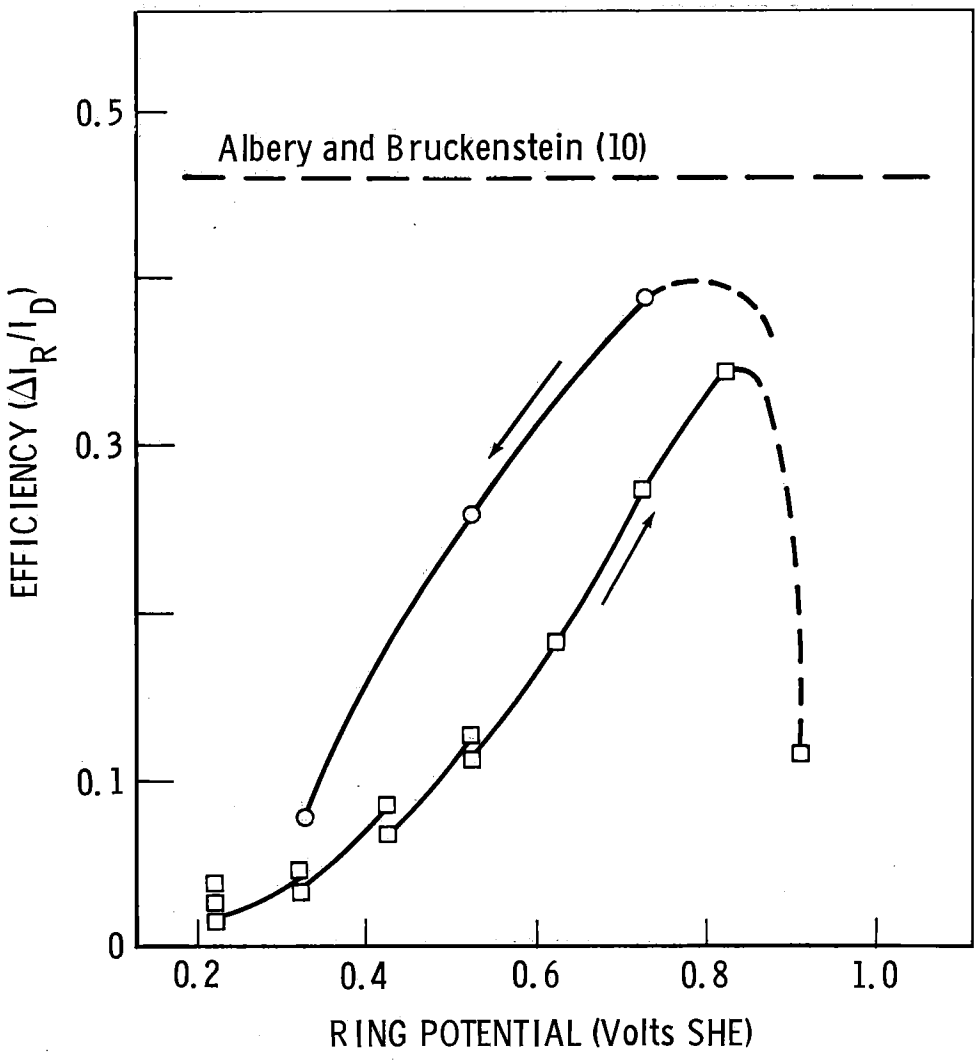


Figure 5

Ring efficiency for oxidation of $Ti^{+3}$ generated at disk by reduction of $TiO^{2+}$ (0.4 M $TiO^{2+}$ in 6M HCl, 400 RPM)

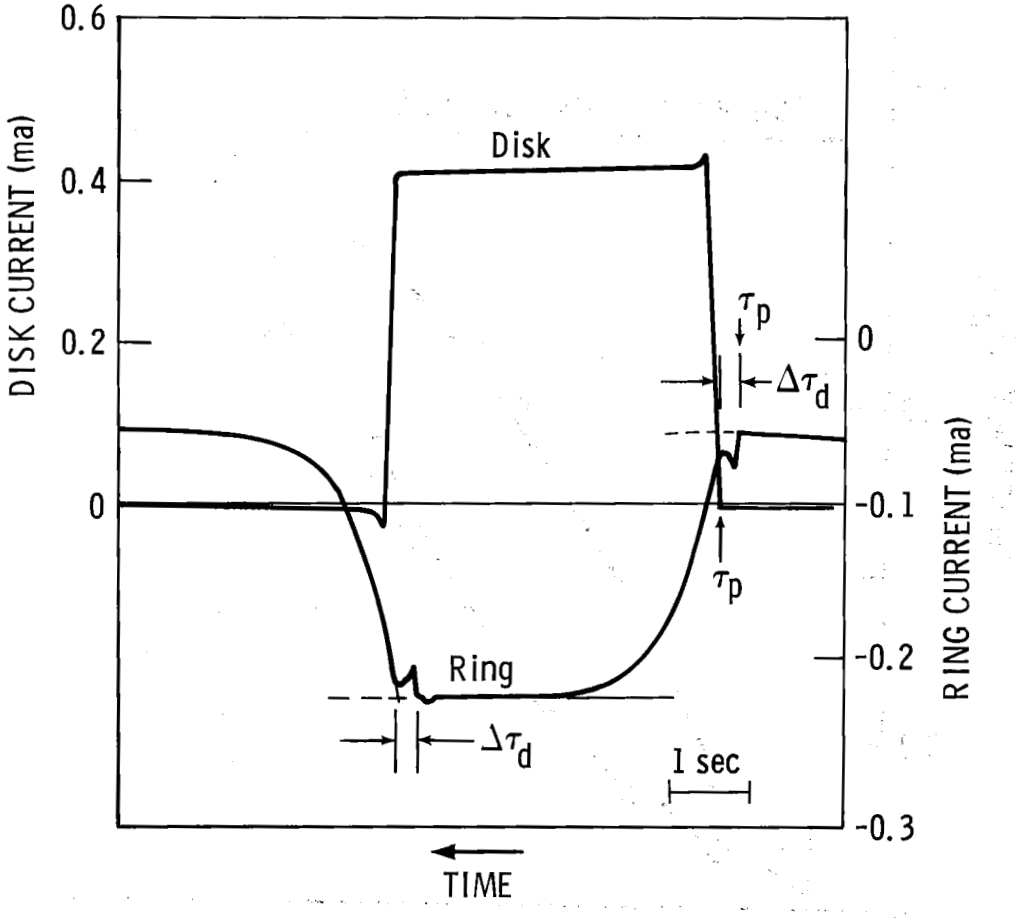


Figure 6

Strip chart recording of disk and ring transient currents for step change in disk potential in 0.6M KI solution (400 RPM)

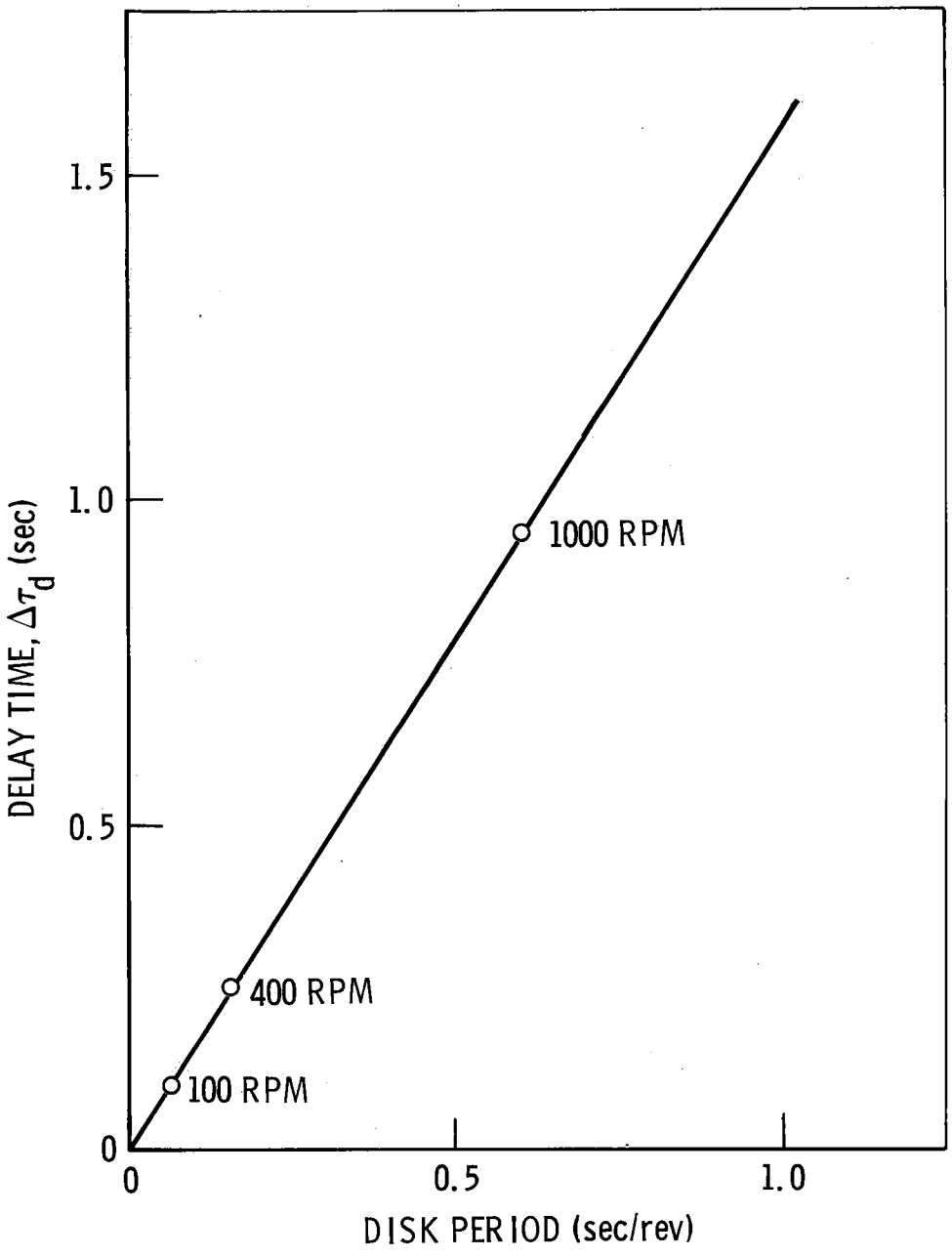


Figure 7

Plot of delay time, $\Delta\tau_d$, versus period of revoltuion

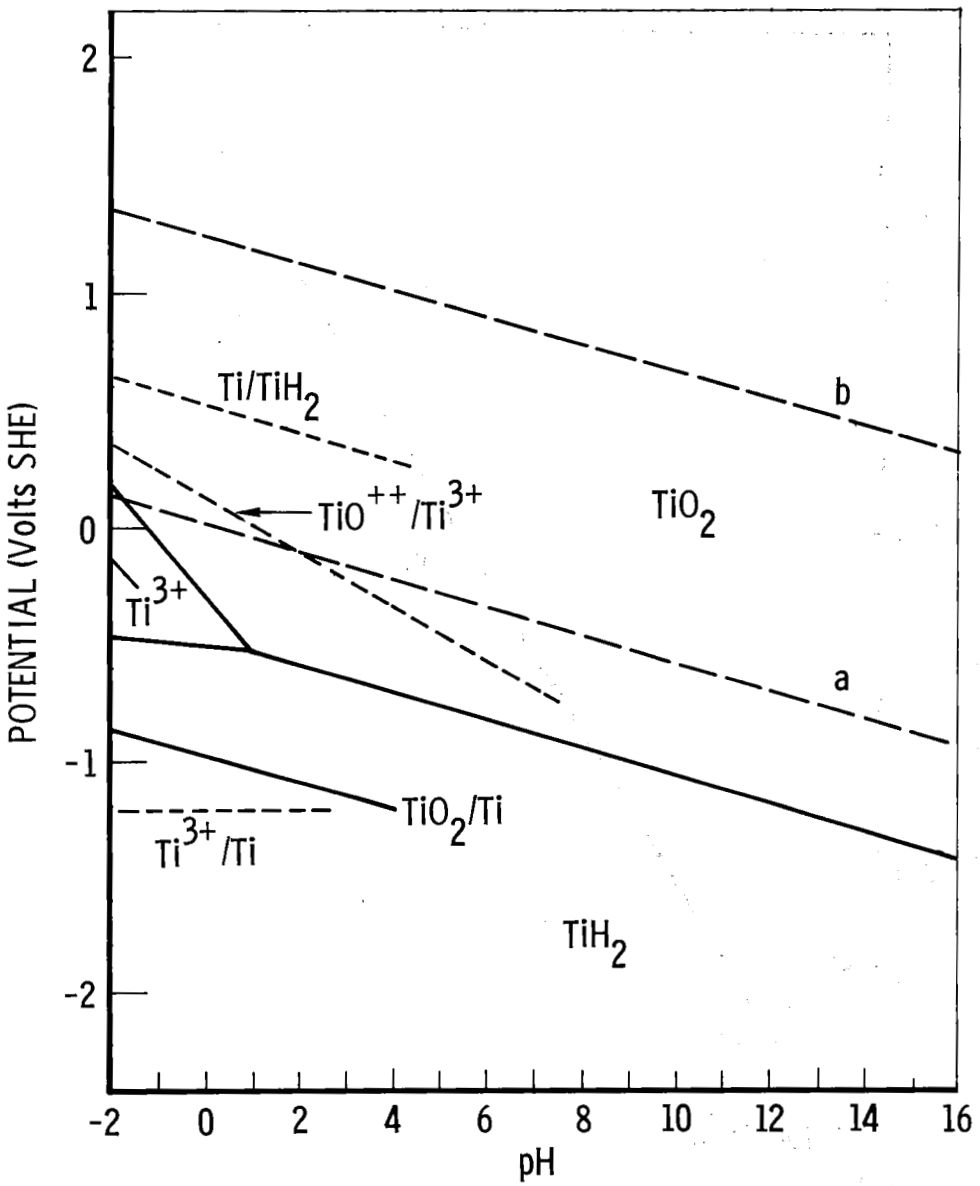


Figure 8a

Potential-pH equilibrium **diagram** for the system titanium-water, at 25°C., based on anhydrous oxides. **(Modified** re $TiH_2$ and $Ti^{3+}$).

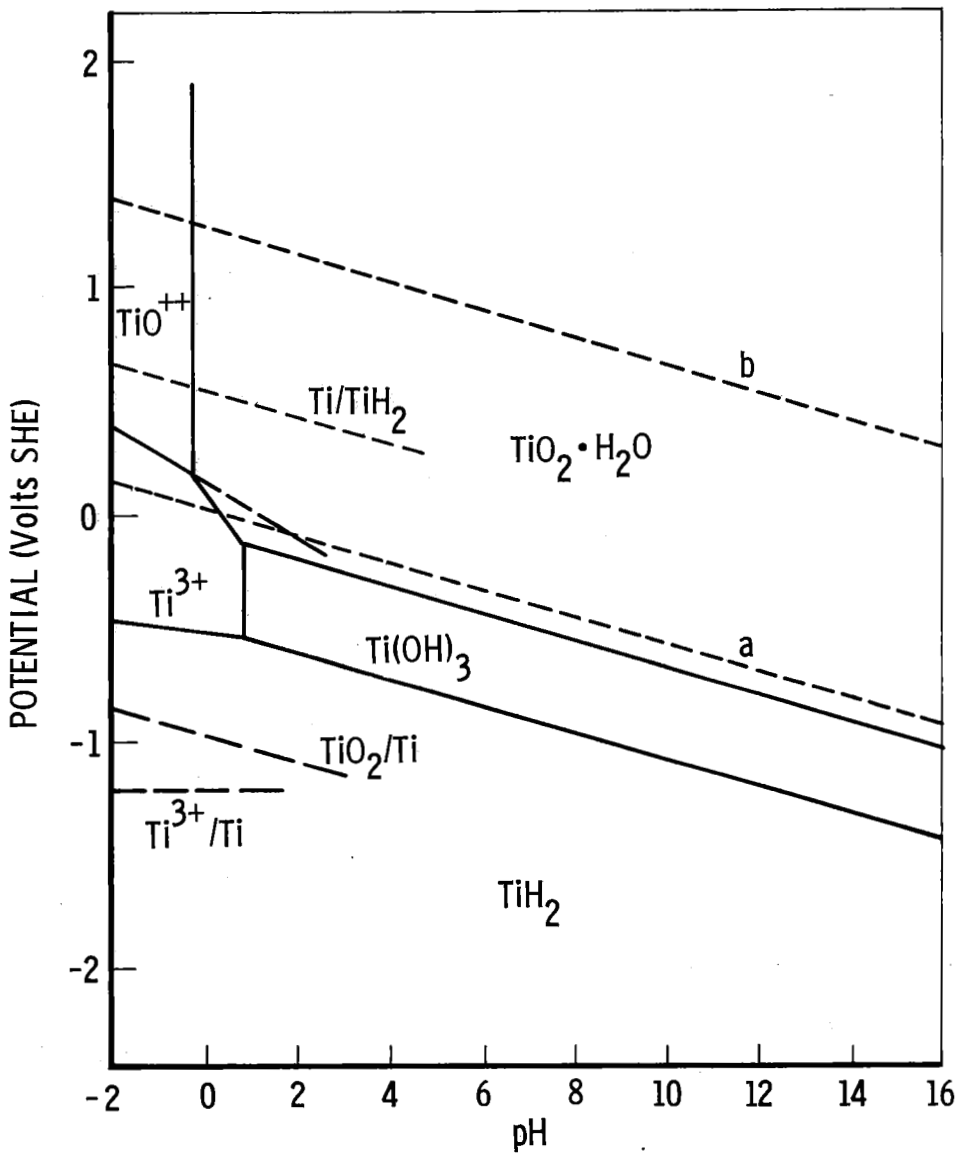


Figure 8b

Potential-pH equilibrium diagram for titanium in water at 25°C based on hydrous oxides (modified re $TiH_2$ and $Ti^{3+}$)

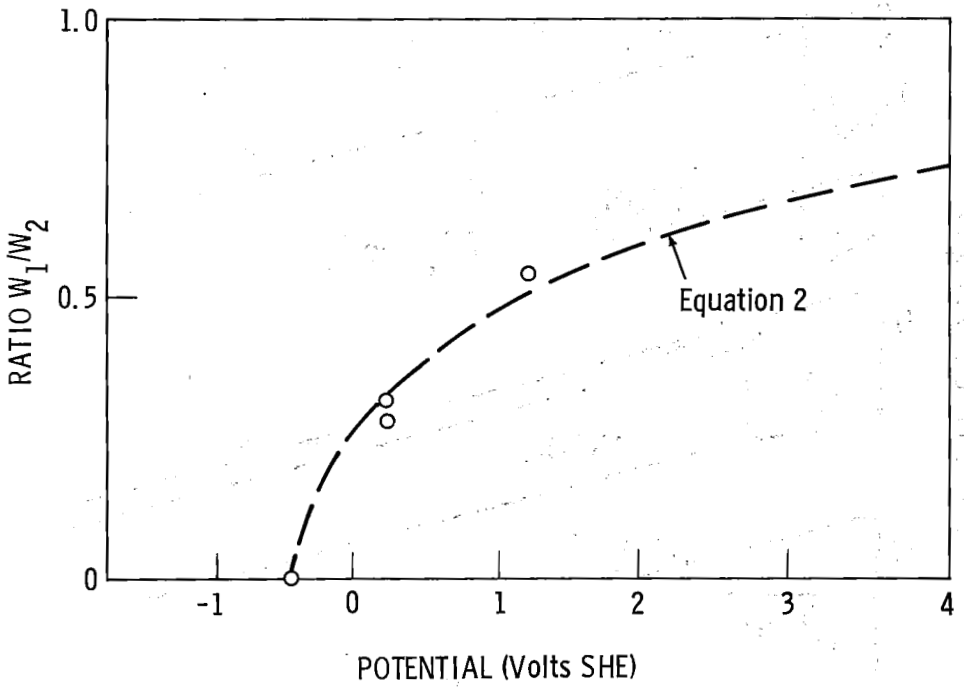


Figure 9

(Weight of Titanium in Solution from scraped Ti disk experiments (6M HCl, ∿ 1000 RPM)

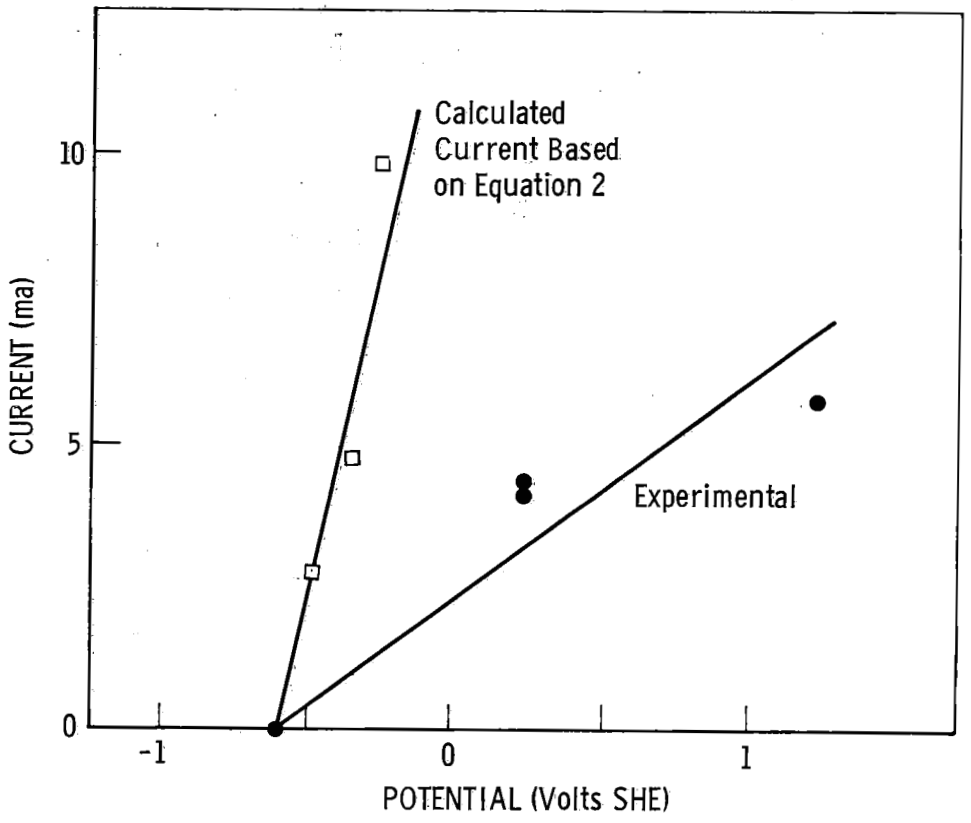


Figure 10

Current-Potential curve for scraped titanium disk experiment (6M HCl, ∿ 1000 RPM, tool advance rate ∿ 50 μ/min.)

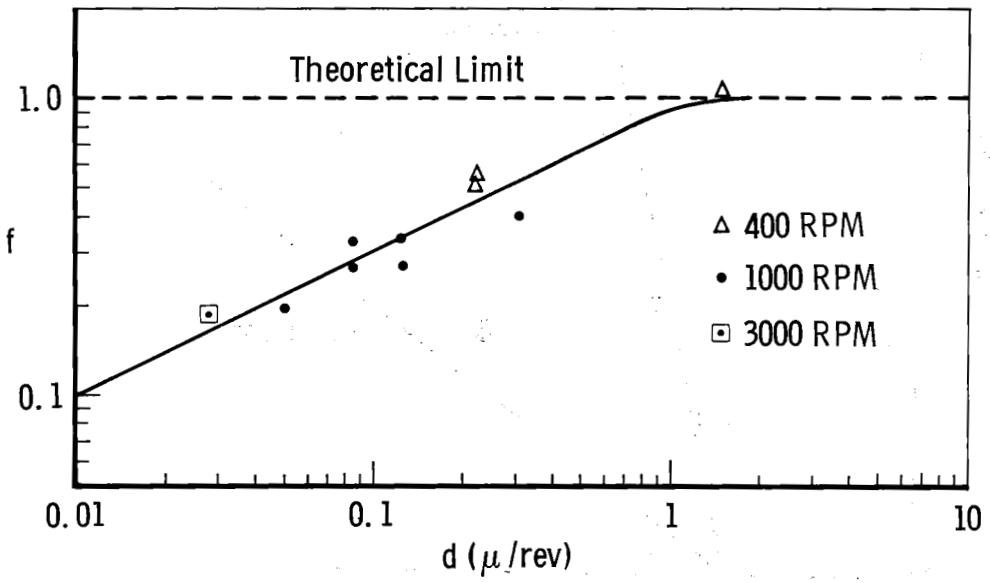


Figure 11

Effect of tool advance rate and RPM on f (6M HCl $\phi_D$ = 0.24V)

# 4.5 Electrochemistry of Freshly-Generated Titanium Surfaces, II Rapid Fracture Experiments

T. R. Beck
Boeing Scientific Research Laboratories
Seattle, Washington 98124

## ABSTRACT

Titanium specimens were rapidly fractured in solution under potentiostatic conditions and current density was measured as a function of time. Effects of alloy, potential, anions, pH, $TiCl_3$ concentration and solvent were studied. Results were interpreted in terms of simultaneous formation of hydride, oxide and $Ti^{3+}$ ion. Some preliminary kinetic parameters were determined assuming Tafel kinetics and patch growth of passivating oxide film.

## INTRODUCTION

In the preceding paper[1] it was shown that a large fraction of the anodic current to a scraped surface of titanium in acid solution goes to form $Ti^{3+}$ ion. In the present paper, current-density - time data for fast fracture of titanium in aqueous solutions are presented and interpreted on the basis of simultaneous dissolution, oxide formation and hydrogen ion reduction.

## EXPERIMENTAL

The fast-fracture technique was previously described and illustrated (Fig. 1, ref. 2). Notched metal specimens, 7.5 cm long, 0.32 cm wide and 0.152 cm thick were made of commercially-pure titanium and some alloys that were of interest in stress corrosion cracking. They were fractured by suddenly releasing a 45 kg weight connected through a 5:1 lever arm. Area of the two new surfaces generated was approximately 0.05 $cm^2$. Specimens were potentiostated in electrolyte in a Teflon cell using a Wenking Model 6379 TR. Most of the experiments were done in 3 M or 12 M HCl. Epoxy resin was applied to the specimens to avoid reaction on the preexisting metal surface. The resin was scored at the notch to facilitate and localize its fracture. Current transient displays were photographed on a Tektronix type 545 A oscilloscope screen. A saturated calomel reference electrode was used and all potentials were converted to the standard hydrogen electrode scale in this paper by adding 0.24 volts.

An analysis of the technique follows.

*Sequence of Events after Fracture.* The proposed sequence of events after a brittle fracture is summarized in Fig. 1. For a brittle fracture with a velocity of $\sim 10^5$ cm/sec (approx. 1/3 the speed of sound) across a $\sim 10^{-1}$ cm thick specimen, the fracture would be complete in $10^{-6}$ sec. It is assumed that under these conditions cavitation bubbles would form on the two fracture faces. Assuming a vapor pressure of ~20 Torr for $H_2O$ and $10^{-6}$ sec to form a monolayer at 1 Torr and unit sticking coefficient[3], the time to form an adsorbed monolayer of $H_2O$ would be $\sim 2 \times 10^{-5}$ sec.

The time for cavitation bubbles to collapse can be estimated from the Rayleigh equation[4]:

$$\tau = 0.9\ r \left(\frac{\rho}{P}\right)^{1/2} \qquad (1)$$

For $r \approx 0.05$ cm (1/2 specimen thickness), $\rho = 1$ gm/cm$^3$ and $P = 1.0 \times 10^6$ gm/cm sec$^2$ (one atmosphere), the collapse time is $\sim 5 \times 10^{-5}$ sec. The potentiostat rise time of $\sim 2 \times 10^{-5}$ sec added to the end of the collapse time gives a total time that is less than the resolution of $2 \times 10^{-4}$ sec attempted on the oscilloscope photographs. It is therefore concluded that cavitation and instrumentation should not impose a limit on the present interpretation of the data.

Charging of the electrical double layer should also be relatively rapid compared to the present resolution time. A cell resistance of ~10 ohm$^2$, a capacitance of 20 μfd/cm$^2$ and electrode area of 0.05 cm$^2$, give a time constant of $\sim 10^{-5}$ sec.

*Effect of Metal Ductility.* In a number of experiments a small current began to flow before the steep rise that signifies the fracture. This initial pre-rise current is attributed to cracking of the protective oxide layer by slight necking in the notched zone prior to fracture.

Fracture faces of brittle and ductile specimens are illustrated in Fig. 2 and current-time curves for those same specimens are respectively shown in Fig. 3. It may be noted that the most brittle specimen (a) showed no necking and a steep rise in current, while the most ductile specimen (b) showed a considerable necking and a considerable current before the steep rise. These specimens were Ti:14% Mo alloy: (a) heat treated at 850°C for 2 hours and water quenched followed by 450°C for 3 hours and air cooling, and (b) heat treated at 850°C for 2 hours and water quenched. The commercially-pure titanium (specimen c) that has been used for many of the kinetic experiments[11] showed a small amount of ductility and a small current prior to the fast fracture. Further embrittlement would be desirable for the kinetics experiments.

*Limitations of Technique*. Measurement and interpretation of current transients to freshly generated surfaces of an active metal such as titanium have some limitations that need be discussed.

The reversible potential for dissolution is so negative that hydrogen ion is simultaneously discharged, and as will be shown the current density for these coupled reactions exeeds 1 amp/cm$^2$ at the mixed potential. There is also a limit as to how close the tip of the Luggin capillary can be placed to the specimen because there is some induced vibration at fracture. The average spacing between the tip and the specimen was about 0.3 cm in the experiments reported here. The potential of the surface therefore tends to go to the mixed potential initially. As passivating films form, decreasing the current, the potential of the new surfaces moves toward the potential established by the potentiostat. The high and somewhat variable ohmic drop between Luggin capillary and specimen precluded ohmic compensation.

Another consequence of the high ohmic drop in solution is that current density will not initially be uniform over the surface. The current density will tend to be highest at the periphery of the fractured surfaces and lowest in the center of these surfaces. The effect is somewhat accentuated by the fact that the fracture faces are pulled about 0.1 to 0.2 cm apart thus the two specimen halves produce some mutual interference to current flow through the electrolyte. The lack of perfectly uniform current distribution will be considered as a second-order effect here, to be taken into account in a later, more rigorous, analysis.

The fracture process also produces disturbed surfaces on a macro- and micro-scale. Macroscopic roughness due to crystal facets, plastic yielding, etc., is observed in Fig. 2. This will be considered second-order effect here and current density will be based on projected area of the new surfaces only. The effects of high dislocation density, exo-electrons, etc., for the new surfaces will be considered outside the scope of the present investigation.

## RESULTS

*Effect of Potential.* Results of experiments conducted with Ti:8-1-1 alloy in 12 M HCl and with commercially-pure titanium in 3 M HCl are shown in Figs. 4 and 5. Conductivity of these two solutions is 0.64 and $\sim$0.5 $ohm^{-1}$ $cm^{-1}$ respectively[5] so that ohmic drops are roughly equivalent, although the activity of HCl is widely different.

In both cases, at anodic potentials ($\phi$ > -0.56V), the initially high anodic current density decayed rapidly and continued over several decades as observed earlier with 0.6 M KCl solutions[2]. In the 12 M HCl,

which was studied more extensively, there was a region of potential at $-0.68 < \phi < -0.56$ V at which the current was initially anodic but later cathodic. At more negative potentials the current was always cathodic and the behavior was somewhat more complex. Cathodic current went through a maximum which was greater and occurred earlier at more negative potentials. Following the maximum the current decayed by two patterns, one with decreasing slope and the second with increasing slope. After a period of about 60 ms the current density became relatively constant and characteristic of hydrogen ion reduction on an oxide covered titanium surface[2].

*Effect of Alloy.* Specimens of commercially-pure titanium, Ti:8-1-1 and Ti:14% Mo gave essentially the same initial current versus time relationship in 3M HCl at -0.26V as shown in Fig. 6. A similar behavior of the newly generated surface is not unreasonable for these alloys as the initial surface atoms would be predominantly titanium. The effect of saturating the solution with Al or Mo ions is yet to be determined.

The behavior of commercially pure aluminum is also compared to titanium in Fig. 6. The aluminum specimen with the same dimensions as the titanium specimens, was of sintered aluminum powder (SAP) and heavily deformed in order to embrittle it for clean fracture. The initial peak currents were essentially the same as expected from an IR limit but the decay in currents followed different laws. The current decay followed a -1/2 power law suggesting an unsteady-state mass-transport limit.

*Effect of Anions.* Results of kinetics experiments conducted in HCl, $H_2SO_4$, HI and HF solutions of the same normality are given in Fig. 7. At a potential of -0.26 V curves for HCl and $H_2SO_4$ were the same within experimental error. The current was lower in HI compared to HCl at -0.26 V

although the current in HI and HCl was virtually identical for experiments at 0.24 V.

In 3M HF, the current rose but did not decay with time as in 3M HCl. A second trace taken about one second after the break gave the same plateau current, showing that passivation did not occur. The current density could not be calculated accurately because the reaction occurred on an extended area where the epoxy resin had separated from the surface. Judging from the staining and etching the active reacting surface was at least seven times the size of the two new fracture surfaces. Conductivity of 3M HF is about 1/35 that of 3M HCl[5], thus explaining why the plateau current was lower in the HF solution in spite of the larger area. The difference in electrode geometry makes a quantitative comparison of current densities difficult. The current reached the plateau level in less than 4 milliseconds indicating that the air-formed titanium oxide film on the old surface is very rapidly removed by HF.

Several experiments were also conducted in 3M $HNO_3$. A cathodic current was observed at a potential of -0.26 V, which was presumed to be due to reduction of nitrate. The mixed potential obtained by extrapolation of peak current vs. potential appeared to be about 0 V.

*Effect of Solvent.* A methanol-HCl solution was prepared by bubbling into anhydrous methanol a stream of HCl gas produced by slowly dripping concentrated $H_2SO_4$ onto NaCl in a flask. HCl concentration in the methanol was determined by titration of an aliquot with standard NaOH solution. A current-density time curve for a new titanium surface in the methanol-HCl solution is shown in Fig. 8. The new titanium surface did not passivate rapidly as in aqueous solutions. In a repeat run with longer

sweep time at the same potential the current did not decay appreciably in over 200 ms.

Current density maxima for new titanium surfaces are plotted in Fig. 9 as a function of potential in various electrolytes. Current density did not decay within 100 ms in runs in methanol solutions except for a run at a potential of -0.66 V for which the peak current density was plotted. The current density was rather erratic in all of the runs in methanol solutions, however, in comparison to a uniformly varying current density in aqueous solutions. Whereas the 3N aqueous solutions had apparent mixed potentials at -0.51 to -0.56 V, the 1.3 N methanol - HCl solution had a mixed potential at about 0.04 V. This could be attributed to the considerably inhibited anodic dissolution but the cathodic kinetics are also inhibited as noted by the small slope on the cathodic slide. In Table 1 is seen that the apparent resistance of the cell on the anodic side is reasonably consistent between the aqueous and methanol solutions. The apparent resistance on the cathodic side is nearly a factor of 10 greater in methanol-HCl although the data suggest a limiting current density rather than a purely ohmic resistance.

*Effect of pH.* The effect of pH for experiments at the same potential is shown in Fig. 10. The surprising result was that from pH -0.5 to +13 the current-time curves appeared to be the same shape within experimental error, suggesting that soluble titanium species ($Ti^{3+}$ or $TiO^{++}$) are formed simultaneously with passivating oxide in this range of pH. In other words, the soluble titanium species appears to form metastably as well as the oxide[1]. The lower conductivity of the less-acid solutions may have been compensated by the increased driving force

to form oxide. The increased current in the solution with 1M KOH could be attributed to its increased conductivity combined with the increased driving force.

The effect of potential on the current-density - time curve for the 3M KCl + 1M KOH solution is similar to that in acid solutions as shown in Fig. 11. The anodic current increased with more positive potential and the peak current occurred at a longer time after fracture. The mixed potential in this solution was about -1.51 V.

*Effect of Added $TiCl_3$ and $TiCl_4$.* The observation[1] that a considerable fraction of the current flowing to a newly generated titanium surface results in formation of soluble $Ti^{3+}$ suggested that the solution near the tip of a stress corrosion crack may be saturated with $Ti^{3+}$. Experiments were therefore conducted in a solution saturated with $TiCl_3$ (and 3M in HCl to provide an adequate conductivity). Figure 12 shows that the peak current was decreased to about 25% of the value in 3M HCl, whereas conductivity of the solution was about 70% that of 3M HCl based on the slope of the peak-current versus potential curves. The mixed potential also shifted to about -0.16 V, i.e., in a direction closer to the reversible potential for hydrogen ion reduction. Therefore it appeared that an anodic reaction had been suppressed. The rate of current decay relative to the peak valve was lower in the $TiCl_3$ saturated solution indicating a slower passivation.

The $TiCl_3$ used to make the above solution contained some $TiCl_4$ (formed by disproportionation in the reagent bottle) because it fumed in contact with air. The question arose whether the Ti(IV) ion thus put into solution was being reduced to $Ti^{3+}$ and decreasing the net anodic current.

To test this hypothesis a solution was made containing considerably more Ti(IV) than would have been present in the saturated $Ti^{3+}$ solution. The Ti(IV) solution was made by adding $TiCl_4$ to concentrated HCl and diluting to 3M HCl + 1M Ti(IV). The peak current observed in Fig. 12 was 60% of that in 3M HCl and the mixed potential was about -0.36 V, while the conductivity of the solution was essentially the same as for 3M HCl. Some Ti(IV) reduction could therefore have occurred, although the smaller concentration of Ti(IV) in the prior experiment with saturated $Ti^{3+}$ solution suggests that presence of Ti(IV) only accounted for a small part of the smaller peak current and shift in mixed potential.

## DISCUSSION

*Reactions.* A minimum of three electrochemical reactions will be considered for newly generated surfaces of titanium[1]:

$$Ti \rightarrow Ti^{3+} + 3e \qquad \text{Reaction 1}$$

$$Ti + 2H_2O \rightarrow TiO_2 + 4H^+ + 4e \qquad \text{Reaction 2}$$

$$H^+ + e \rightarrow H \qquad \text{Reaction 3}$$

Other lower oxides may be formed [6] and at high anodic potentials $TiO^{++}$ may be formed, but at this state of development of the theory and experiments consideration of only the three above reactions appears justified. Reactions with dissolved oxygen were not considered significant at the high initial current densities. Tomashov and Vershinina[7] found no difference between deaerated and oxygen-saturated solutions in their abrasion experiments with titanium.

The hydrogen atoms from reaction 3 may combine with the surface atoms of titanium to form $TiH_2$ or combine to form hydrogen molecules. Formation of hydride is considered preferred because of its large negative

free energy of formation[8]. Otsuka[9] showed that visible hydride layers form on titanium at long exposure to HCl. Oxidation of a hydride surface layer at higher potentials might also occur.

The potential-pH diagrams given in the foregoing paper[1] will be used to interpret the kinetics experiments. Models are proposed to separate currents for the individual reactions from the total current.

*Analysis of Peak Current Densities.* Fig. 13 compares peak current densities observed in the kinetics experiments to a steady-state polarization curve of Ti:8-1-1 in 12M HCl. An ohmic drop correction was made to the peak current densities by

$$\Delta\phi_o = \frac{i\bar{\ell}}{\kappa} = i\bar{R} \qquad (2)$$

in which the average Luggin capillary to electrode spacing was 0.3 cm and the conductivity of 12M HCl was $\sim$0.5 $ohm^{-1}$ $cm^{-1}$. The dashed corrected anodic and cathodic Tafel lines were drawn with 120 mV slopes and represent lower-bounds for the new surfaces as the ohmic correction is rather approximate. The anodic current density in the steady-state active region is seen to be at least five orders of magnitude lower than the current density observed for freshly-generated surfaces, while as observed earlier[2], the steady-state cathodic current density is about one order of magnitude lower.

That the steady-state anodic rates are at least five orders of magnitude lower than those for new surface indicates that even in the active region dissolution is strongly inhibited. This passivation is attributed to oxide which apparently can exist metastably even in strongly acid solution. Steady-state dissolution of titanium in the active region

may proceed through oxide formation and dissolution steps if the surface is completely oxide covered. Steady-state rate of dissolution of pure titanium in the active region is very strongly dependent on HCl concentration as shown in Fig. 13 and as observed by Otsuka[9]. Steady-state was fairly quickly reached in 12M HCl but very slow to attain in 6M HCl. In contrast, the peak anodic current for Ti:8-1-1 fractured in 12M HCl (Fig. 4) and for commercially-pure titanium fractured in 3M HCl (Fig. 5) were very similar, both being limited by ohmic drop.

*Initial Mixed Potential.* Initial open-circuit potentials after fracture of titanium specimens were previously observed[10] to vary with pH with a slope of -59 mV/pH unit. In the present kinetics experiments conducted potentiostatically the initial mixed potential was about 180 mV more negative than the initial open-circuit potentials in 3M HCl and in 1M KOH and may be described by

$$\phi_m = -0.72 - 0.059\ \mathrm{pH}$$

The less-negative values of the earlier initial open-circuit potentials may be attributed to not reaching $\phi_m$ from a prebreak open-circuit potential about a volt more positive.

The significance of the -59 mV slope will now be considered. At the mixed potential

$$i_a = i_{oa} \exp[B(\phi_m - \phi_{ea})] \tag{3}$$

and

$$i_c = i_{oc} \exp[-B'(\phi_m - \phi_{ec})] \tag{4}$$

assuming that current density is uniform and high, that oxide coverage is negligible at $10^{-4}$ seconds from break and that mass transport is not

limiting. Letting $i_a = i_c$ and solving for $\phi_m$,

$$\phi_m = \frac{B\phi_{ea} + B'\phi_{ec}}{B + B'} + \frac{\ell n\left(\frac{i_{oc}}{i_{oa}}\right)}{B + B'} \tag{5}$$

Two obvious ways to account for a slope of -59 mV/pH unit are:

a) reversible potentials for anodic reaction 2 and cathodic reaction 3 both have a slope of -59 mV and the exchange current densities are independent of pH (or vary the same way with pH);

b) reversible potential of reaction 3 has -59 mV slope, reversible potential for reaction 1 independent of pH and one exchange current density (reaction 3) is proportional to hydrogen ion concentration with $B = B' = \frac{\frac{1}{2}F}{RT}$.

The first case was assumed previously[10] whereas the scraped rotating disk experiments[1] now suggest the second case to be more correct.

*Initial Partial Current Densities.* Initial partial anode and cathode current densities on oxide-free surfaces will be estimated here. The measured current density is

$$i = i_a - i_c \tag{6}$$

where the partial current densities may be described in terms of the mixed potential and mixed-potential current density by

$$i_a = i_m \exp[B(\phi_p - i\bar{R} - \phi_m)] \tag{7}$$

and

$$i_c = i_m \exp[-B'(\phi_p - i\bar{R} - \phi_m)] \tag{8}$$

Assuming for convenience that $B = B' = \frac{\frac{1}{2}F}{RT}$, it can be shown that

$$i_a = i_m \exp[\sinh^{-1}\left(\frac{i}{2i_m}\right)] \tag{9}$$

$$i_c = i_m \exp[-\sinh^{-1}\left(\frac{i}{2i_m}\right)] \tag{10}$$

and

$$\phi_p - \phi_m = \frac{1}{B} \sinh^{-1}\left(\frac{i}{2i_m} + i\bar{R}\right) \tag{11}$$

Calculated partial anodic and cathodic current densities are plotted as a function of potential in Fig. 14 for $i_m = 1$ amp/cm$^2$ (minimum value, Fig. 13) and $i_m = 10$ amp/cm$^2$. It is seen that the initial anodic and cathodic current densities are both appreciable for all of the potentials applied in the experiments. Therefore models for transient behavior should consider them simultaneously.

*Simultaneous Hydrogen Ion Discharge and Diffusion of Hydrogen into Metal.* The purpose here is to explore whether unsteady-state diffusion of hydrogen into the metal from the surface could significantly affect the surface concentration of hydrogen predicted from the partial cathodic current density. The analysis is based on the assumptions in Table 2.

In that titanium hydride has a negative free energy of formation[8] the hydrogen atoms formed by reaction 3 will be assumed to react with the metal to form a monolayer of hydride in preference to dissolution in the electrolyte. Simultaneous unsteady-state diffusion of hydrogen into the semi-infinite metal phase would be expected and the rate will be estimated. Nucleation of a bulk phase of $TiH_2$ is assumed to occur only after the first monolayer of $TiH_2$ is completed. As $TiH_2$ has metallic properties it will be assumed that hydrogen ion reduction can occur on the $TiH_2$ monolayer and the resulting H atoms can diffuse to adjacent bare metal sites to form $TiH_2$. This permits a monolayer of $TiH_2$ to form in a finite time.

These assumptions lead to

$$d\theta_H = \frac{i_H d\tau}{Q_H} - \frac{\theta_H c_H zF}{Q_H}\left(\frac{4}{\pi}\frac{D_H}{\tau}\right)^{1/2} d\tau \tag{12}$$

which has the solution

$$\theta_H = \frac{a}{2b^2}\left[2b\tau^{1/2} + e^{-2b\tau^{1/2}} - 1\right] \tag{13}$$

where

$$a = \frac{i_H}{Q_H}$$

$$b = \frac{(4/\pi)^{1/2} D_H^{1/2} c_H zF}{Q_H}$$

Equation (13) is plotted in Fig. 15 using the following constants:

$Q_H = 4 \times 10^{-4}$ coulomb/cm$^2$ for $TiH_2$, i.e., $H_2$ on each surface atom of Ti in basal plane;

$z = 2$ for $TiH_2$;

$D_H = 1.4 \times 10^{-11}$ cm$^2$/sec for $\alpha$ - Ti based on extrapolation of high temperature diffusion data[13] to room temperature ($D_H$ is greater $\beta$ - Ti).

It is seen that for the range of hydrogen ion discharge current densities that might be expected in Fig. 15 that diffusion into the metal could be important in influencing coverage based on the above assumption. Without diffusion, for example, $\theta_H$ would equal unity at 0.4 ms for $i_H = 1$ amp/cm$^2$. Therefore a rigorous analysis of coverage of the surface by $TiH_2$ must consider the simultaneous solid-state diffusion. Some of the qualitative ramifications will be considered in subsequent sections.

*Analysis of Current Density Transients.* Assumptions used in the analysis of transient current density behavior are listed in Table 3. Assumptions 1, 2, 3 and 6 are based on the preceding discussion. Growth of the passivating layer of oxide is assumed to occur by two-dimensional patch growth with instantaneous nucleation (assumption 4) because of the high resistivity of the oxide and the high overpotential for oxide formation at the mixed potential. Random dissolution of titanium to $Ti^{3+}$ is assumed to occur on the bare surface (assumption 5) because of the high overpotential associated with the mixed potential. Titanium hydride is assumed to inhibit because of thermodynamics (ref. 1, Fig. 8) and $TiO_2$ is assumed to inhibit for kinetic reasons in accordance with Fig. 13.

1. Reactions on Anodic Side of Mixed Potential

Fleischmann and Thirsk[11] present an analysis of nucleation and growth of electrode deposits. The various modes are one-, two- and three-dimensional growth with either instantaneous or progressive nucleation. Of these modes, two-dimensional growth of oxide film patches with instantaneous nucleation appears most appropriate to titanium. The two-dimensional film would be consistent with the known low conductivity of $TiO_2$ and the small amount of charge required for passivation. Instantaneous nucleation would be expected at the initial mixed potential which is about 0.3 V anodic to the oxide reversible potential. The equation for current density to the oxide patches may be written[11]:

$$i_{ox} = 2mQ_{ox}C\tau \exp[-C\tau^2] \qquad (14)$$

in which

$$C = \pi n\left(\frac{\delta_M i_2}{Q_{ox}}\right)^2 \tag{15}$$

Other sequences of reaction are perhaps possible such as dissolution by reaction 1 followed by an oxidation and precipitation. Alternately, formation of oxide such as by reaction 2 could be followed by dissolution. Such more-complicated reaction sequences will not be considered at the present time for the newly generated surfaces.

It is assumed that throughout the period of growth of the passivating layer the greater fraction of the current goes to form soluble $Ti^{3+}$, i.e.,

$$i_+ >> i_{ox} \tag{16}$$

and therefore

$$i \approx i_+ \tag{17}$$

It is further assumed that the value of $C$ in equation (15) is constant, independent of time or potential, so that integrating equation (14) in respect to time and dividing by $mQ_o$ gives coverage

$$\theta = 1 - \exp[-C\tau^2] \tag{18}$$

The current density for formation $Ti^{+3}$ is assumed to follow Tafel kinetics on the bare areas between oxide patches

$$i_+ = i_{o+}(1 - \theta)\ \exp[B(\phi - \phi_{e+}) \tag{19}$$

where

$$\phi = \phi_p - i\,\overline{R} \tag{20}$$

combining equations (17), (18), (19) and (20) gives

$$i = i_{o+}\ \exp[-C\tau^2]\ \exp[B(\phi_p - \phi_{e+} - i\,\overline{R})] \tag{21}$$

which may be solved explicitly for $\tau$ giving

$$\tau = C^{-\frac{1}{2}}\left[B(\phi_p - \phi_{e+}) - B\bar{R}i - 2.30 \log\left(\frac{i}{i_{o+}}\right)\right] \qquad (22)$$

Equation (22) gives a relation between current density and time containing only one adjustable parameter; C. The following values were used for a series of experiments with commercially-pure titanium conducted in 3M HCl:

$B = 19.5$ Volts$^{-1}$

$\bar{R} = 0.24$ Volts/(A/cm$^2$) (from peak current densities, Fig. 5)

$\phi_{e+} = -1.2$ Volts

$i_{o+} = 4 \times 10^{-5}$ A/cm$^2$ (Fig. 13)

Experimental data for pure titanium fractured in 3M HCl at a potential of 0.24 V are compared to equation (22) (using a value of $C^{-\frac{1}{2}} = 0.5 \times 10^{-3}$) in Fig. 16. The equation fits over a portion in the middle of the experimental data and the misfit at short and long time might be attributed to the simplifying assumptions.

At short times the current for formation of oxide cannot be negligible. For example, equation (14) is plotted in Fig. 16 assuming $m = 1$, $Q_{ox} = 4 \times 10^{-4}$ Coul/cm$^2$ and $C = 4 \times 10^6$ (from $C^{-\frac{1}{2}} = 0.5 \times 10^{-3}$ above). This oxide current density is not negligible, even for monolayer patches. Further, because even monolayer patches consume a fraction of the current, the patches cannot be many monolayers in thickness.

The lack of fit of equation (22) at about $\tau \gtrsim 1.5$ milliseconds from the break might be attributed to change in the value of C with potential of the surface as the $i\bar{R}$ component decreases (discussed later), or to the onset of oxide film thickening through the high field conduction mechanism.

2. Region of Mixed Potential

In the region of potential between -0.68 and -0.56 V in 12M HCl an initial anodic peak followed by a cathodic peak is observed (Fig. 4). An enlarged oscilloscope trace at a potential of -0.66 V is shown in Fig. 17. The measured current density is, of course, the difference between the actual anodic and cathodic currents (Eq. 6). A proposed resolution of the anodic and cathodic current densities is indicated in Fig. 17. It is assumed that after the cathodic peak the actual anodic component is a small fraction of the cathodic component. The decrease in cathodic current density is assumed as before[2] to be due to oxide coverage at a low current density. The initial slope of the cathodic current density after its peak is extrapolated back to zero time. The difference between measured current density before the cathodic peak and this extrapolated line is considered to be the initial anodic current density. It is recognized as the case in Fig. 13 that these initial anodic and cathodic current densities are lower-bound values.

Extrapolation of the initial rate of decay of anodic current density to the cathodic baseline in Fig. 17 gives a time, $\tau_o$, for inhibition of the anodic current density. Dividing $\tau_o$ into a charge density for passivating film gives a current density, i.e.,

$$i = \frac{Q}{\tau_o} \tag{23}$$

It is seen in Fig. 18 that the current density calculated from equation (23) increases with more negative potentials suggesting that hydride inhibited anodic dissolution. (A charge density of $4 \times 10^{-4}$ Coulomb/cm$^2$ for an inhibiting monolayer of $TiH_2$ was used in equation 23.) The equilibrium potentials in potential-pH diagrams[1] would allow a hydride layer to inhibit

dissolution of titanium to $Ti^{3+}$ at surface potentials more negative than -0.51 Volts which is possible for $\phi_m$ = -0.68 V. The cathodic current density based on equation (23) is higher than the peak cathodic current density (Fig. 6, ref. 2) consistent with an iR correction required for the latter. The calculated cathodic current density is also consistent as to order of magnitude and sign of the slope to values of $i_H$ for $i_m$ = 1 $A/cm^2$ replotted from Fig. 14. Diffusion of hydrogen into the metal would add a further correction to equation (23).

Values of i calculated from equation (23) continue to decrease with applied potential above the mixed potential as seen in Fig. 18. It is therefore possible that formation of hydride also plays a role in the initial current density decay on the anodic side of the mixed potential. The increasing time to reach peak current density as a function of increasing potential in Fig. 11 would be consistent with an initial hydride passivation. There is thus some ambiguity as to whether hydride or oxide is the initial passivating agent on the anodic side of $\phi_m$.

3. Reactions on Cathodic Side of Mixed Potential

Cathodic current densities in 12M HCl over a longer time span after the peak are plotted semilogarithmically from oscilloscope traces for four potentials in Fig. 19. There appear to be three distinct regions with different behavior of current density with time. In region III the current density becomes nearly constant with time and is interpreted as previously[2] to be hydrogen ion discharge on oxide covered titanium. Region II is characterized by abrupt changes in slope at each end and a generally slowly increasing slope in between. The transition time from region I and II appears to be independent of potential in the range available while the transition time from regions II to III decreases with increasing potential. The latter inidates an anodic film inhibiting hydrogen ion reduction and

the oxide patch growth model will be applied.

An analogous equation to (22) differing only in sign of some of the terms can be derived for hydrogen ion reduction inhibited by oxide patches. The ohmic term can as a first approximation be neglected at the smaller current densities on the cathodic side in Fig. 19. Therefore, plotting log $i$ versus $\tau^2$ should give a straight line for this model. The data for region II fall more nearly on a straight line by such a procedure as shown in Fig. 20. Values of the constant $C$ derived from the slopes are discussed below.

Region I data appear to be linear on the semilog plot but on linear coordinates the slope decreases with time. Previously[2] region I was assumed to hydrogen ion reduction inhibited by oxide film growth but its present interpretation is not clear.

*Value of* $C^{1/2}$. Equation (15) states that $C^{1/2}$ is proportional to the current density at the edge of the oxide patches, all other factors constant. In that the surface initially approaches the mixed potential irrespective of the applied potential, the number of oxide patches nucleated will be assumed constant. The values of $\delta_M$ and $Q_{ox}$ would also be expected to be constant and variation in $C^{1/2}$ will be taken as a measure of variation of $i_2$ in equation (15).

A Tafel plot of $C^{1/2}$ is presented in Fig. 21. Values on the cathodic side of the mixed potential were determined from the slopes in Fig. 19. Values on the anodic side were determined from initial slopes of log $i$ versus plots of the data for 12 and 3M HCl of Figs. 4 and 5. This technique can give approximate values of $C^{1/2}$ near the mixed potential where the second exponential term in equation (21) does not vary too rapidly with time. A numerical technique for evaluation of $C^{1/2}$ point by point as a

function of time and thus potential at the surface is based on

$$C^{\frac{1}{2}} \int_0^{\tau} C^{\frac{1}{2}} \, d\tau = -\tfrac{1}{2}\left[1 + B\bar{R}i\right] \frac{d \, \ell n i}{d\tau} \qquad (24)$$

which is developed in the appendix. Such a variation of $C^{\frac{1}{2}}$ with calculated potential at the surface for an applied potential of -0.26V is shown as the dashed curve to the right of the maximum in Fig. 21.

A variation of $C^{\frac{1}{2}}$ with potential would be expected if $i_2$ is kinetically controlled. On the cathodic side of the mixed potential the increase with potential may be due to Tafel kinetics for the oxidation reaction at the edges of the patches. An alternative is that the oxidation reaction is inhibited by a hydride layer at the more negative potentials. The decrease in $C^{\frac{1}{2}}$ on the positive side of the mixed potential could be attributed to a relative increase in competing dissolution at the edges of the patches. The decrease in $C^{\frac{1}{2}}$ with potential could explain the lack of fit of equation (22) using constant $C^{\frac{1}{2}}$ to the experimental data after 1½ ms in Fig. 16.

## CONCLUSIONS

The following conclusions are made for the behavior of freshly fractured surfaces of titanium in various electrolytes under potentiostatic conditions:

1. Freshly-generated titanium surfaces are rapidly passivated (in milliseconds) in aqueous HCl solutions even up to 12M concentration.
2. Current-density - time curves over the first 10 ms are not strongly influenced by alloy composition from commercially-pure to alloys with 8% Al or 14% Mo in 3M HCl.
3. Solutions of HCl and $H_2SO_4$ of same normality gave similar current-density -

time curves. No evidence of passivation occurred in 3M HF and air-formed oxide was apparently removed within 4 ms. In $HNO_3$ solution the mixed potential of the new surface was shifted in the positive direction apparently by nitrate reduction.

4. Passivation did not occur at times up to 200 ms in methanol - HCl solution although initial dissolution rate appeared to be lower than in aqueous HCl. There appeared to be a limiting current density for the reduction reaction.
5. The shape of the current density - time curve was similar in chloride solutions from 12M HCl to 3M KCl + 1M KOH indicating formation of metastable soluble species at all pH in this range as well as formation of metastable oxide in strong acid.
6. Saturated $TiCl_3$ in HCl inhibits the initial anodic reaction and shifts the mixed potential in the positive direction qualitatively consistent with expected effect on a dissolution reaction.
7. New surfaces of titanium are more active in HCl solutions than the steady-state oxide-covered surface; hydrogen ion reduction rate increased by a factor of about 10 and initial anodic dissolution rate up by a factor $>10^5$ in 12M HCl and $>10^7$ in 6M HCl.
8. A model is proposed which is semiquantitatively in agreement with the kinetics and has the following features:

   a) three simultaneous reactions occur

   $$Ti \rightarrow Ti^{3+} + 3e \qquad 1$$

   $$Ti + 2\,H_2O \rightarrow TiO_2 + 4H^+ + 4e \qquad 2$$

   $$H^+ + e \rightarrow H \qquad 3$$

   b) current density at mixed potential for 1 and 3 is high

($\geq$ 1 Amp/cm$^2$), therefore ohmic polarization tends to give an initial surface potential near the mixed potential;

c) titanium hydride monolayer resulting from 3 inhibits 1 although some H diffuses into bulk of metal;

c) $TiO_2$ monolayer which forms more slowly by patch growth model inhibits 1 and 3.

## NOMENCLATURE

$B$ = constant in Tafel equation, $\frac{\alpha nF}{RT}$, volts$^{-1}$

$c$ = concentration, mole/cm$^3$

$C$ = constant in equation 14, sec$^{-2}$

$D$ = diffusivity, cm$^2$/sec

$F$ = Faraday, Coul/equiv

$i$ = current density, A/cm$^2$

$i_2$ = current density at edge of oxide patches, A/cm$^2$, also number of electron, for rate determining step

$\ell$ = distance, cm

$m$ = number of monolayers

$n$ = number of oxide patches, cm$^{-2}$

$P$ = pressure, gm/cm sec$^2$

$Q$ = charge density, Coul/cm$^2$

$r$ = radius, cm

$R$ = resistance, ohm

$z$ = valence

$\alpha$ = transfer coefficient, dimensionless

$\theta$ = coverage, dimensionless

$\kappa$ = conductivity, ohm$^{-1}$ cm$^{-1}$

$\rho$ = density, gm/cm$^3$

$\tau$ = time, sec

$\phi$ = potential, Volts

subscripts

a = anodic

c = cathodic

e = equilibrium

H = Hydrogen

m = mixed potential

M = monolayer

o = exchange current density

ox = oxide

p = potentiostat

+ = metal cation

## REFERENCES


1. T. R. Beck, *this Journal*, I. Scraped Rotating-Disk Experiments.
2. T. R. Beck, *J. Electrochem. Soc.*, 890 (1968).
3. e.g., S. Dushman and J. M. Lafferty, "Scientific Foundations of Vacuum Technique," 2nd ed. John Wiley, New York, 1962.
4. Lord Rayleigh, *Phil. Mag.*, 34, 200 (1917).
5. International Critical Tables, McGraw Hill, New York, 1933.
6. N. D. Tomashov and P. M. Al'tovskii, "Corrosion and Protection of Titanium," Moscow, 1963.
7. N. D. Tomashov and L. P. Vershinina, *Electrochimica Acta*, 15, 501 (1970).
8. JANAF Interim Thermochemical Tables, Dow Chemical Co., Midland, Mich., 1960.
9. R. Otsuka, Scientific Papers of the Institute of Physical and Chemical Research, 54, 97 (1960).
10. T. R. Beck, *Proceedings of Conference Fundamentals Aspects of Stress Corrosion Cracking*, Ohio State University, Sept., 1967, p. 605, R. W. Staehle, ed., NACE, Houston, 1969.
11. M. Fleischmann and H. R. Thirsk, Advances in Electrochemistry and Electrochemical Engineering, 3, 123, P. Delahay and C. W. Tobias, eds., John Wiley, New York, 1963.
12. Craighead, et al., in Progress in Metal Physics, 7, Chalmers and King eds., Pergamon Press, New York, 1958.
13. R. J. Wasilewski and G. L. Kehl, *Metallurgia*, 225 (1954).

# APPENDIX

Equation for calculation of $C^{\frac{1}{2}}$

## A. Dissolution Current Density

Assume:

1. Dissolution occurs by Tafel kinetics on bare areas between oxide patches
2. An ohmic drop between Luggin capillary and specimen surface $\Delta\phi_o = i\rho\bar{\ell}$
3. Uniform macroscopic current density across face of specimen.
4. Avrami condition applies, i.e.,

$$1 - \theta = \exp(-\theta_{ex})$$

$$i_+ = i_{o+}(1 - \theta) \exp\left[\frac{\alpha nF}{RT} (\phi_p - \phi^e - i\rho\bar{\ell})\right]$$

$$= i_{o+} \exp( - \theta_{ex}) \exp\left[\frac{\alpha nF}{RT} (\phi_p - \phi^e - i\rho\bar{\ell})\right]$$

$$= i_{o+} \exp\left[\frac{\alpha nF}{RT} (\phi_p - \phi^e)\right] \exp\left[- \frac{\alpha nF\rho\bar{\ell}}{RT} i - \theta_{ex}\right]$$

Taking logarithms, $\ell n\, i_+ = \ell n i_{o+} + \frac{\alpha nF}{RT} (\phi_p - \phi^e) - \frac{\alpha nF\rho\bar{\ell}}{RT} i - \theta_{ex}$

Differentiating, $\frac{d\ell n\bar{i}_+}{d\tau} = - \frac{\alpha nF\rho\bar{\ell}}{RT} \frac{d\bar{i}}{d\tau} - \frac{d\theta_{ex}}{d\tau}$

B. Equation for Patch Growth

Assume:

1. Instantaneous nucleation of $n$ patches/cm$^2$
2. Two-dimensional patch growth
3. No thickening of patches until first layer complete

$$i_2 = \delta_m$$

$$d\theta_{ex} = n(2\pi r)dr$$

$$dr = i_2\left(\frac{\delta_m}{Q_o}\right)d\tau$$

$$r = \int_o^\tau i_2 \left(\frac{\delta_m}{Q_o}\right) d\tau$$

$$d\theta_{ex} = 2\pi n\left(\int_o^\tau i_2 \left(\frac{\delta_m}{Q_o}\right) d\tau\right) i_2\left(\frac{\delta_m}{Q_o}\right) d\tau$$

$$\frac{d\theta_{ex}}{d\tau} = 2C^{1/2} \int_o^\tau C^{1/2}\, d\tau$$

Where $C^{1/2} = (\pi n)^{1/2} \left(\frac{\delta_m}{Q_o}\right) i_2$

C. Equation to Evaluate $C^{1/2}$

Assume: Current to form patches is negligible compared current, $\therefore i_+ = i$

Combining final equation in parts A and B

$$\frac{d\ell ni}{d\tau} = - \frac{\alpha n F \rho \bar{\ell}}{RT} \frac{di}{d\tau} - 2C^{\frac{1}{2}} \int_o^\tau C^{\frac{1}{2}} \, d\tau$$

or

$$C^{\frac{1}{2}} \int_o^\tau C^{\frac{1}{2}} \, d\tau = - {}^1/2 \left[ 1 + \left( \frac{\alpha n F \rho \bar{\ell}}{RT} \right) i \right] \frac{d\ell ni}{d\tau}$$

ACKNOWLEDGMENT

The many helpful discussions with Dr. M. J. Blackburn and Dr. W. H. Smyrl are gratefully acknowledged. Mr. Robert L. Lee conducted many of the experiments. This work was supported by NASA Headquarters contract NAS 7-489.

Table 1 Comparison of Apparent Cell Resistance at Current Peak to Calculated Value

| Solution | $\kappa$ ($ohm^{-1}cm^{-1}$) | $R_a$ (ohm) (exp.) | $R_c$ (ohm) (exp.) | $R_{calc}$* (ohm) | $\frac{R_a}{R_{calc}}$ | $\frac{R_c}{R_{calc}}$ |
|---|---|---|---|---|---|---|
| 3N HCl | 0.65 | 4.6 | - | 1.9 | 2.4 | - |
| 0.6N KCl | 0.066 | 51 | - | 19 | 2.7 | - |
| 3N $H_2SO_4$ | 0.50 | 5.3 | 5.3 | 2.5 | 2.1 | 2.1 |
| 1.3 N HCl in MeOH | 0.37** | 8.3 | 70 | 3.4 | 2.4 | 20 |

* $R_{calc} = \frac{1}{2\kappa\sqrt{\pi A}}$ $^2$.

** Valve of $\kappa$ for aqueous solution - no data for methanol solution.

Table 2. Assumptions used in calculation of Surface Coverage of Hydride

1 Hydrogen ion discharge occurs uniformly and randomly molecule by molecule on bare surface and on $TiH_2$ molecules already present.

2 At least a monolayer of $TiH_2$ is formed on the surface before a new solid phase of $TiH_2$ is nucleated.

3 The average concentration of hydrogen on the surface is coverage, $\theta_H$, times concentration of hydrogen in $TiH_2$. The equilibrium solubility of hydrogen in titanium in contact with bulk $TiH_2$ phase is $1.5 \times 10^{-4}$ atom wght/cm$^3$ [12] compared to about $1.5 \times 10^{-1}$ atom wght/cm$^3$ in $TiH_2$. It is assumed that the concentration will drop from the latter supersaturation level to the lower equilibrium level after bulk $TiH_2$ phase is nucleated.

4 Transport of hydrogen into the metal is by unsteady-state diffusion into a continuum semi-infinite medium, i.e., grain-boundary, grain-composition and grain-orientation effects are ignored.

Table 3. Assumptions Used in Analysis of Current Density Transients

1 Potential of surface initially approaches $\phi_m$ i.e., @ $i_m > 1$ A/cm$^2$, $\phi_p - \phi_m \approx i\bar{R}$.

2 Reactions 1, 2, and 3 occur simultaneously initially.

3 Reaction 3 occurs randomly, molecule by molecule on bare surface and is not inhibited by $TiH_2$ monolayer but is inhibited by $TiO_2$ layer in accordance with Fig. 13.

4 Reaction 2 occurs by 2-dimensional patch growth on bare surface and by displacement of or growth on surface of hydride monolayer.

5 Reaction 1 occurs randomly on bare surface and is inhibited by $TiH_2$ and by $TiO_2$.

6 Surface potential goes in direction of $\phi_p$ after peak current and reactions and rates are altered accordingly.

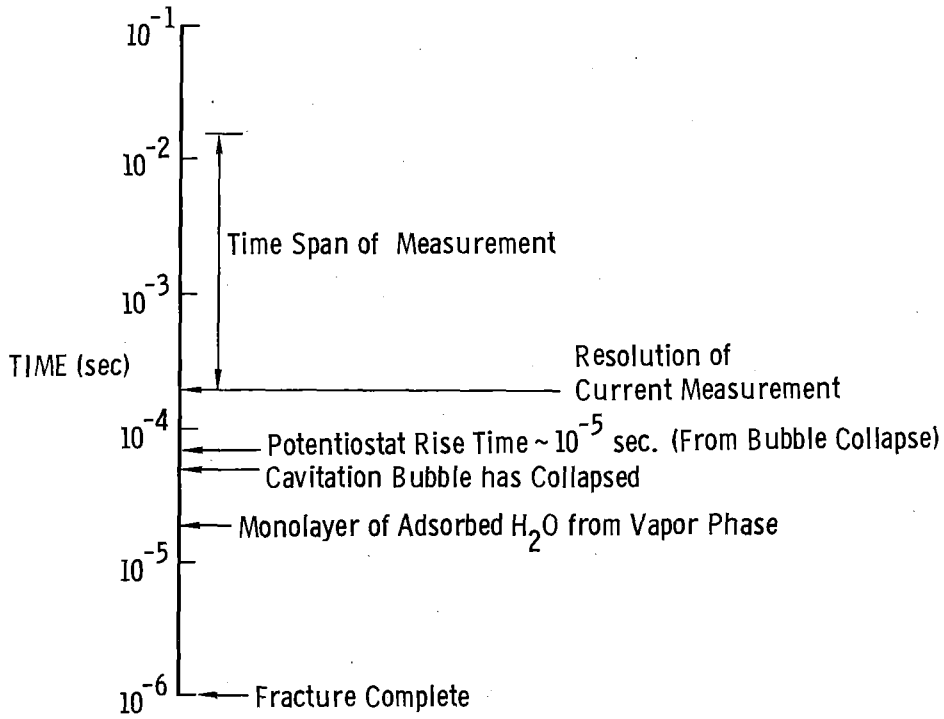


Fig. 1 - Sequence of events after fracture.

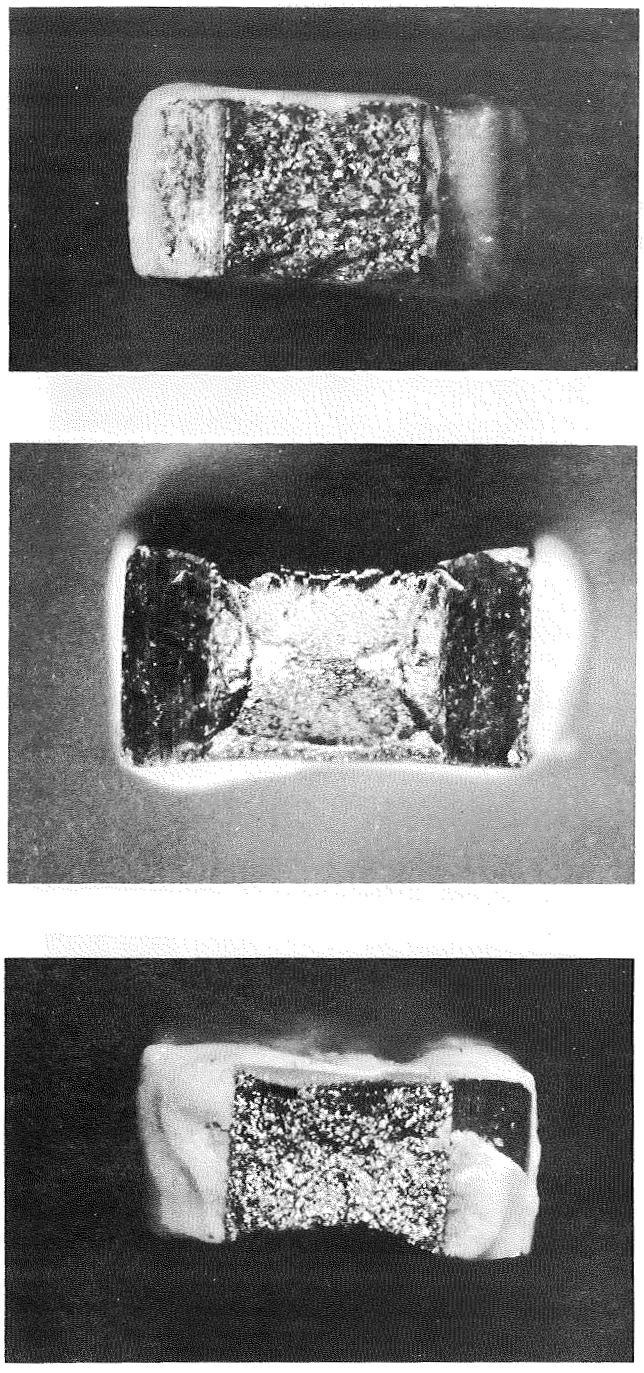


Fig. 2 - Appearance of fracture surfaces

a. Ti:14% Mo brittle
b. Ti:14% Mo ductile
c. Commercially pure Ti.

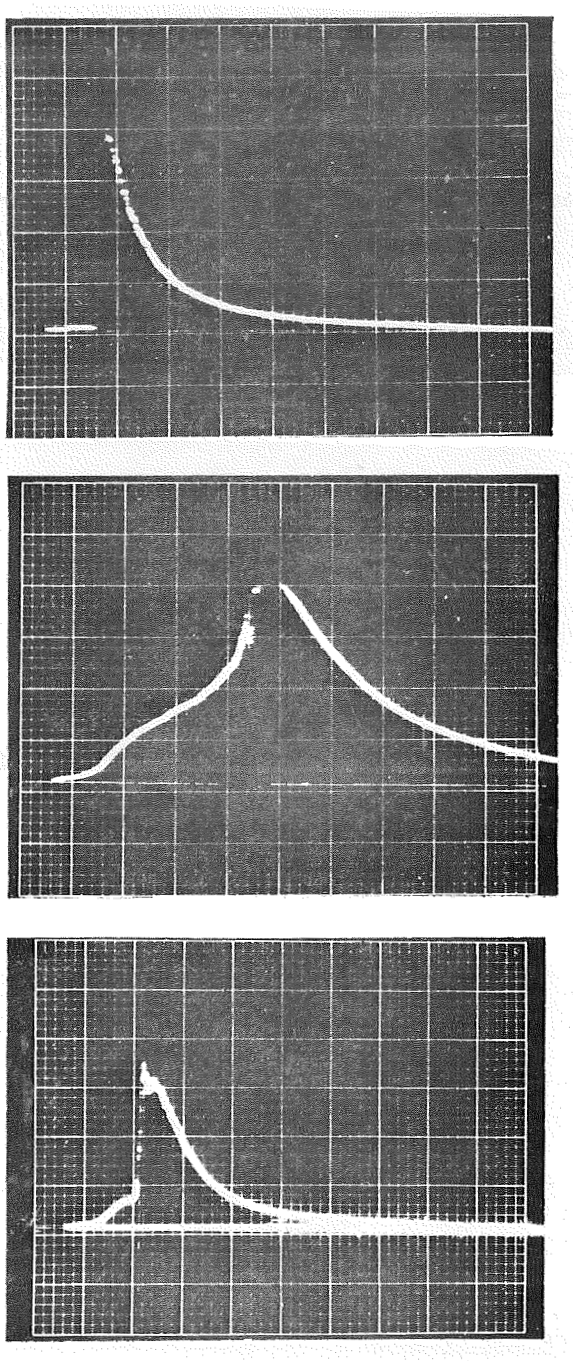


Fig. 3 - Oscilloscope traces for specimens fractured in 3.0 M HCl at -0.26 V (A $\approx$ 0.05 $cm^2$) horizontal - 2 ms/cm, vertical - 20 mA/cm

a. Ti:14% Mo brittle
b. Ti:14% Mo ductile
c. Commercially pure Ti.

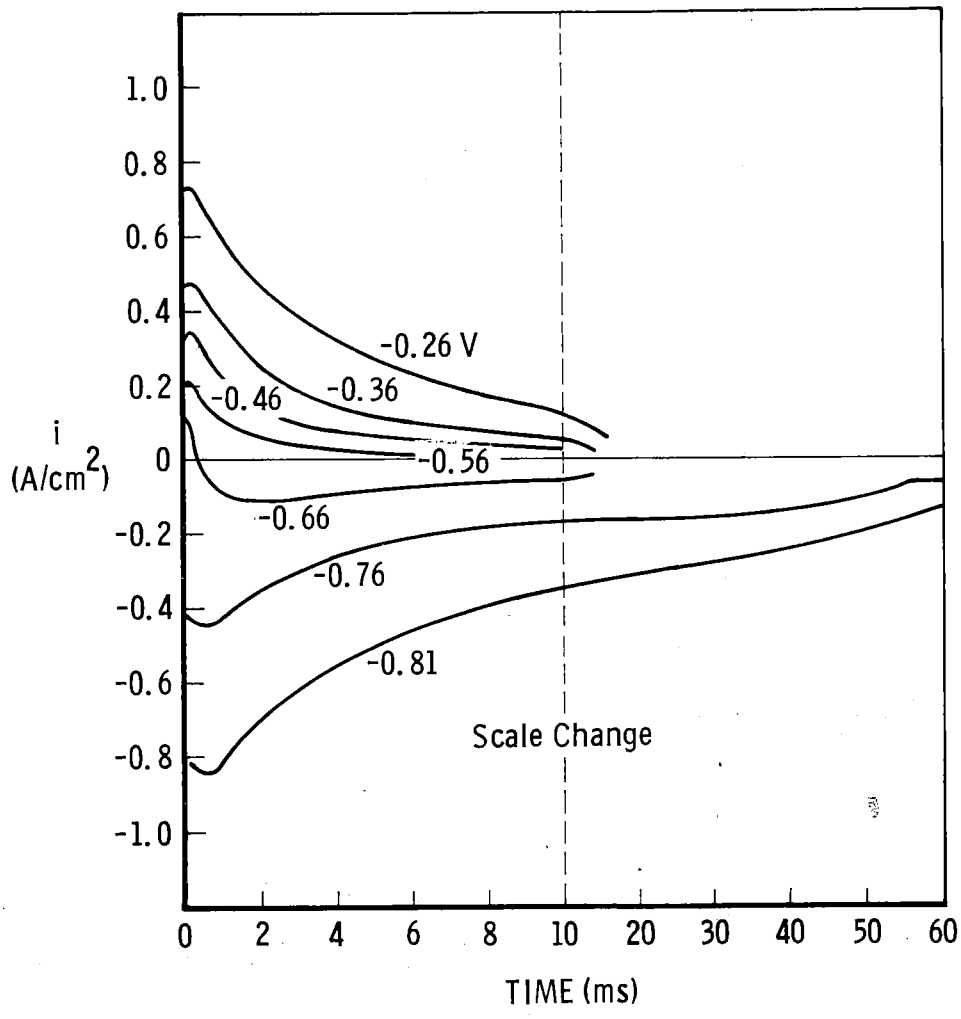


Fig. 4 - Current density-time curves for new surfaces of Ti:8-1-1 in 12M HCl.

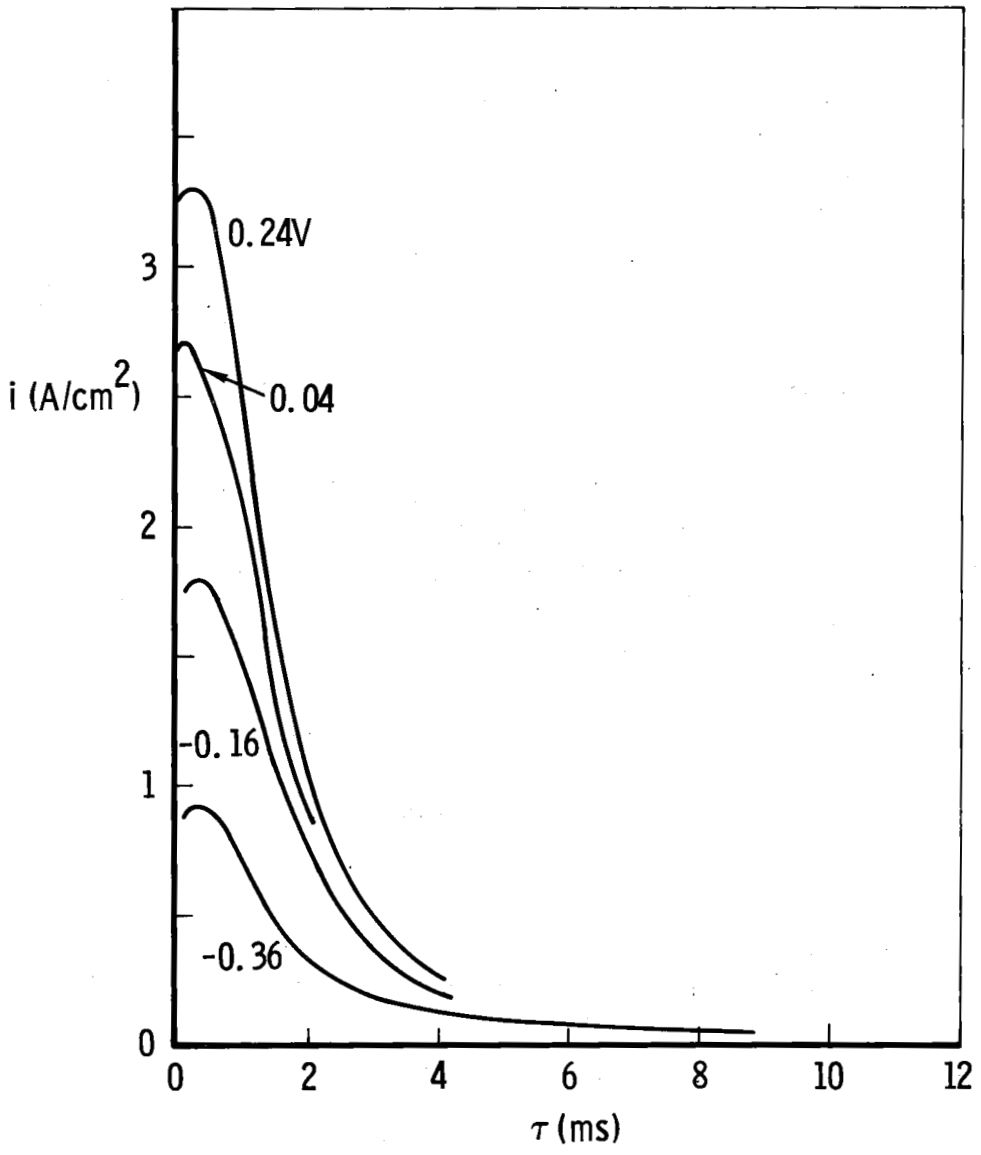


Fig. 5 - Current density-time curves for new surfaces of commercially-pure titanium in 3M HCl.

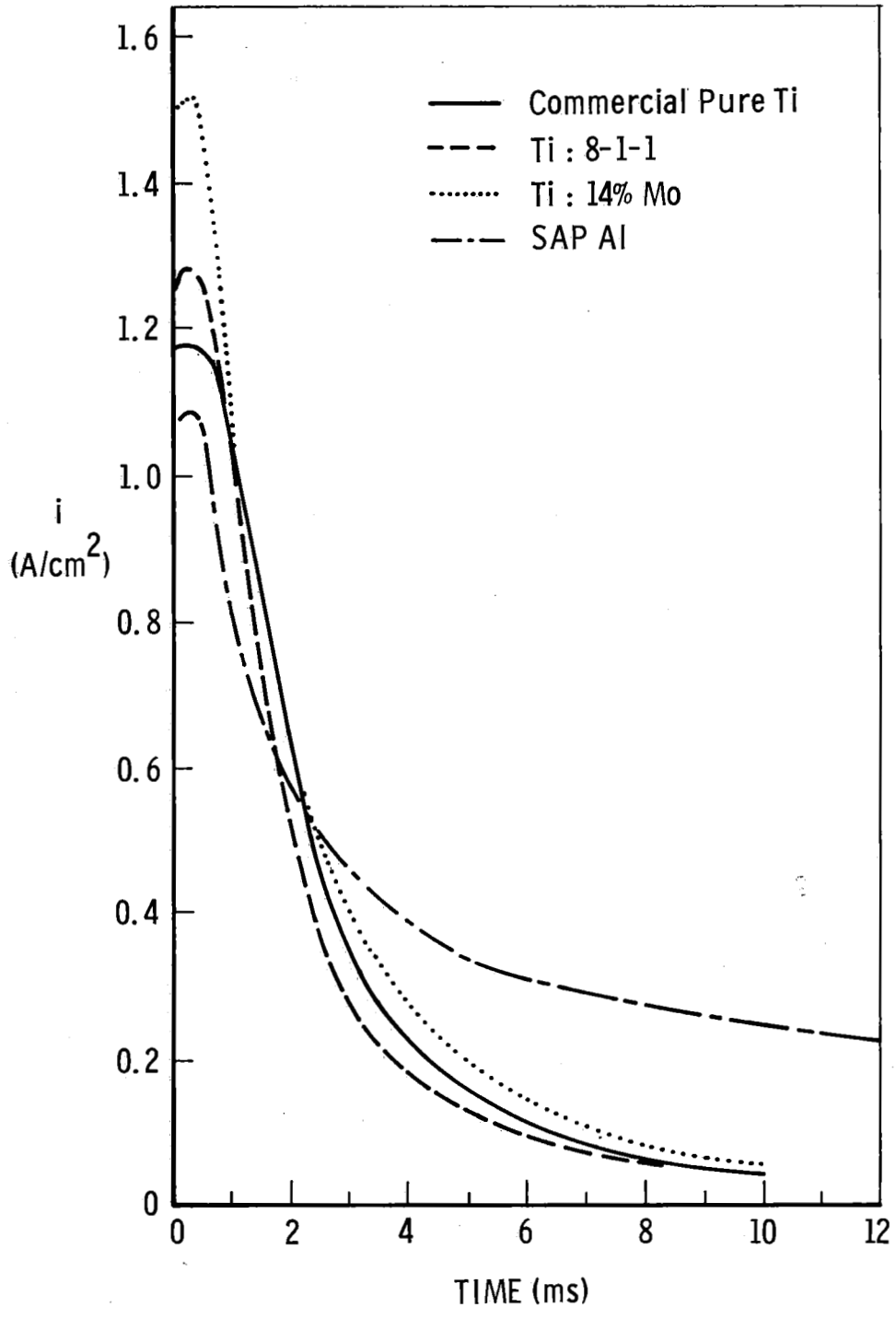


Fig. 6 - Current density-time curves for new surfaces of Ti alloys and SAP Al in 3M HCl at -0.26 V.

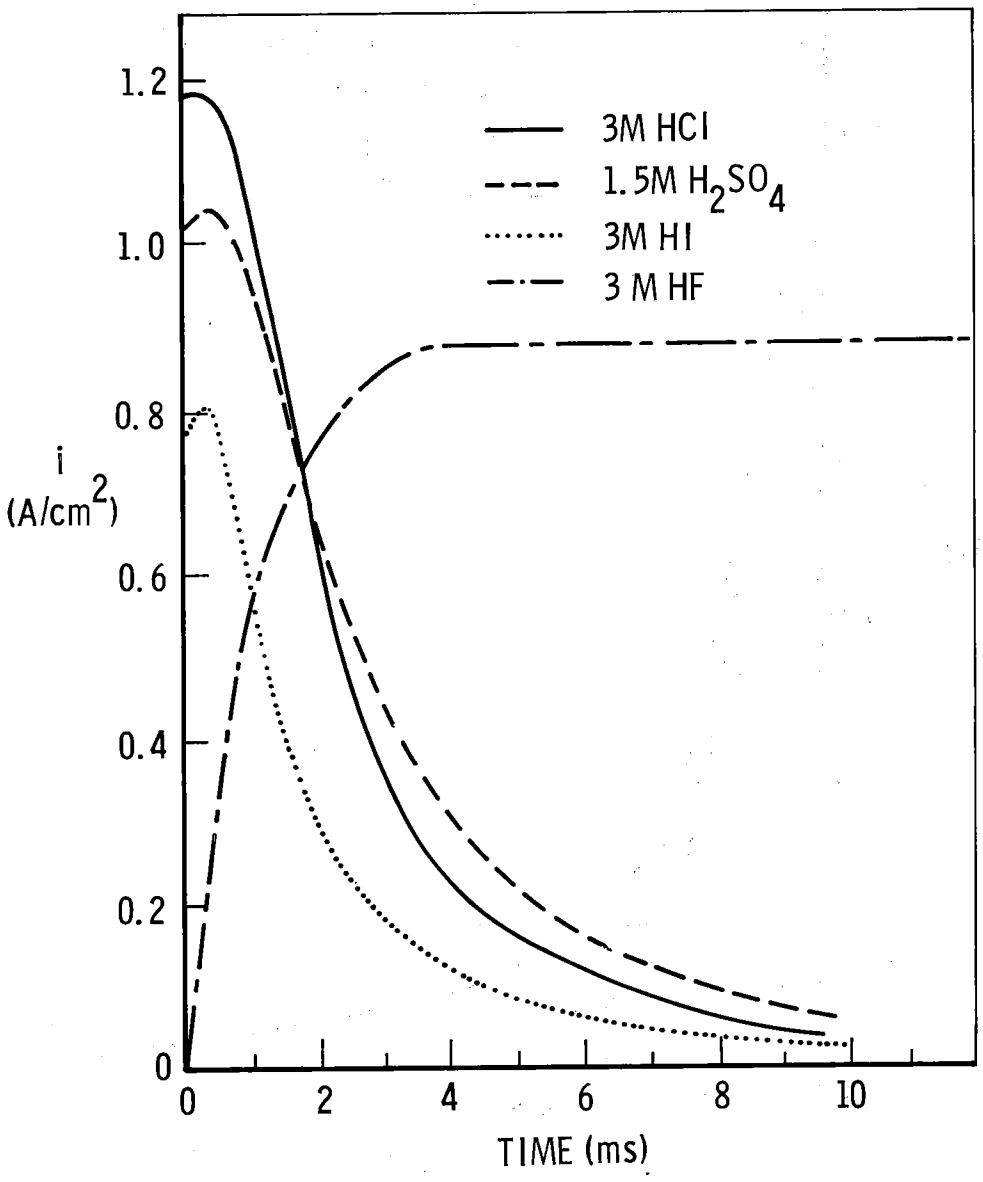


Fig. 7 - Current density-time curves for new surfaces of commercially pure Ti in four acids at a potential of -0.26 V.

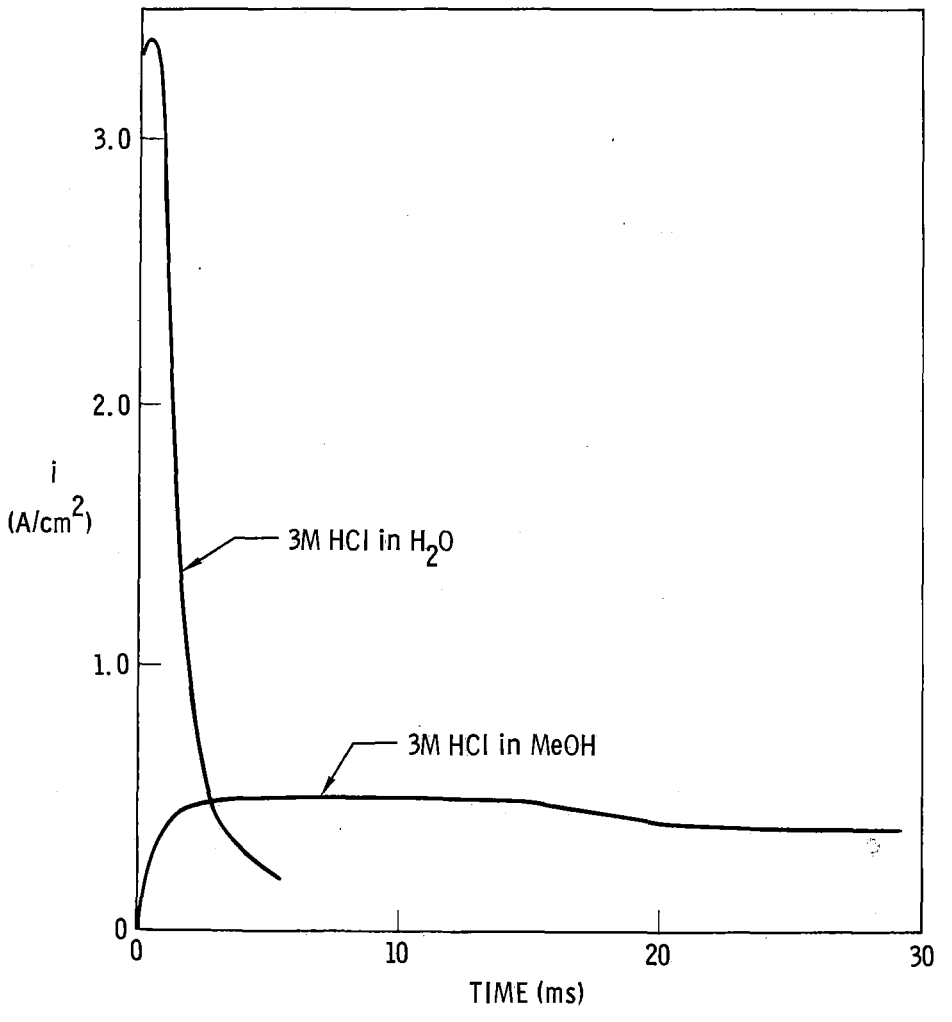


Fig. 8 - Current density-time curves for new surfaces of commercially-pure Ti in aqueous and methanolic solutions of HCl at a potential of 0.24 V.

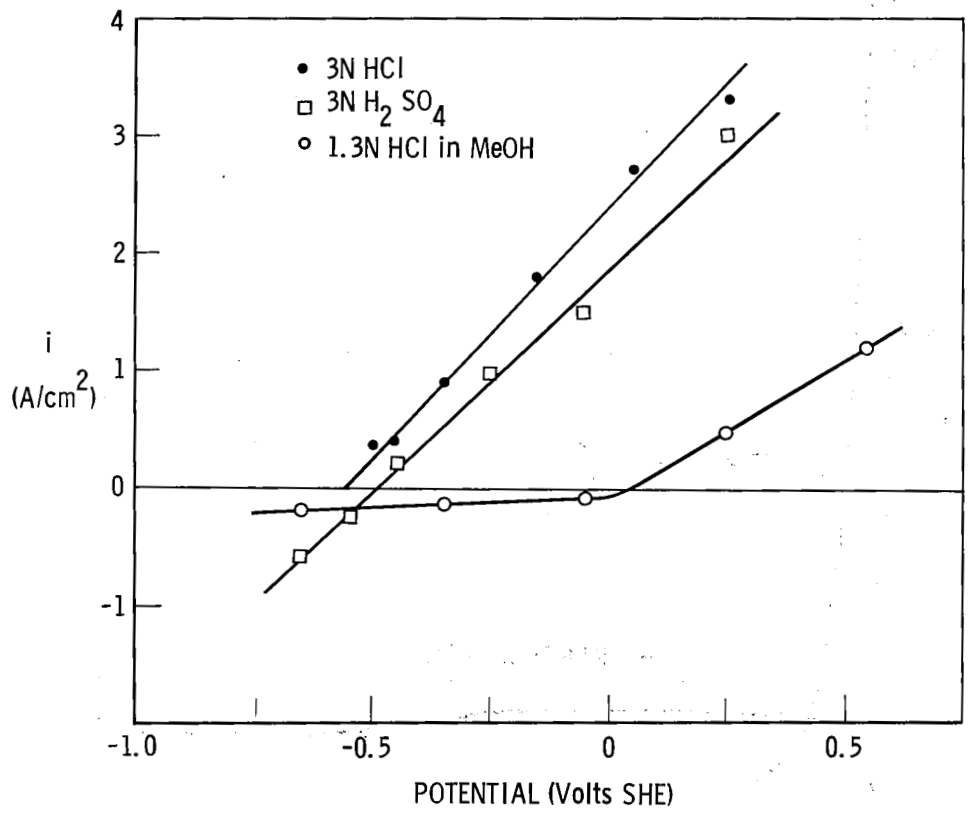


Fig. 9 - Peak current density for new titanium surfaces as a function of potential in aqueous and methanol solvents.

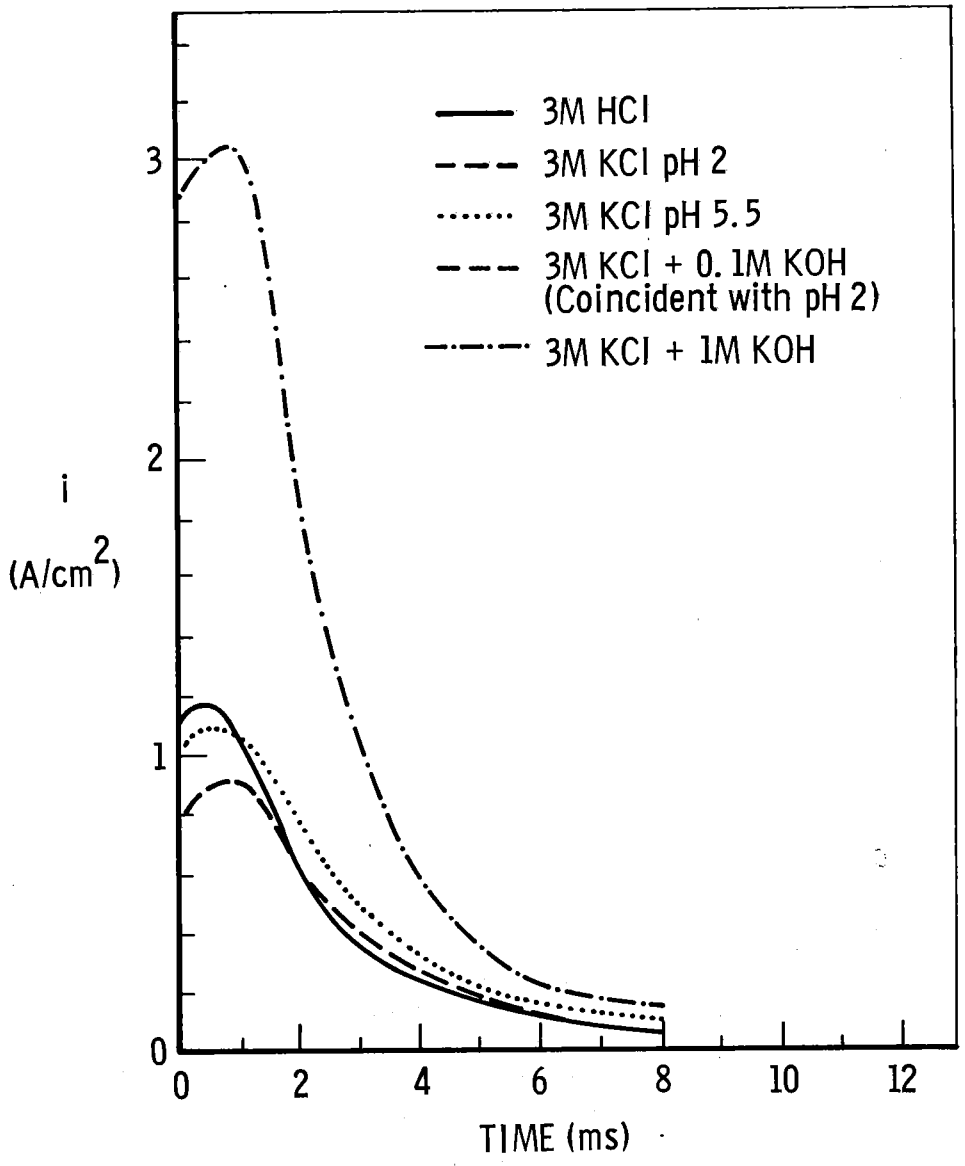


Fig. 10 - Effect of pH on current density-time curves for new surfaces of commercially-pure Ti in 3M chloride solutions at a potential of -0.26 V.

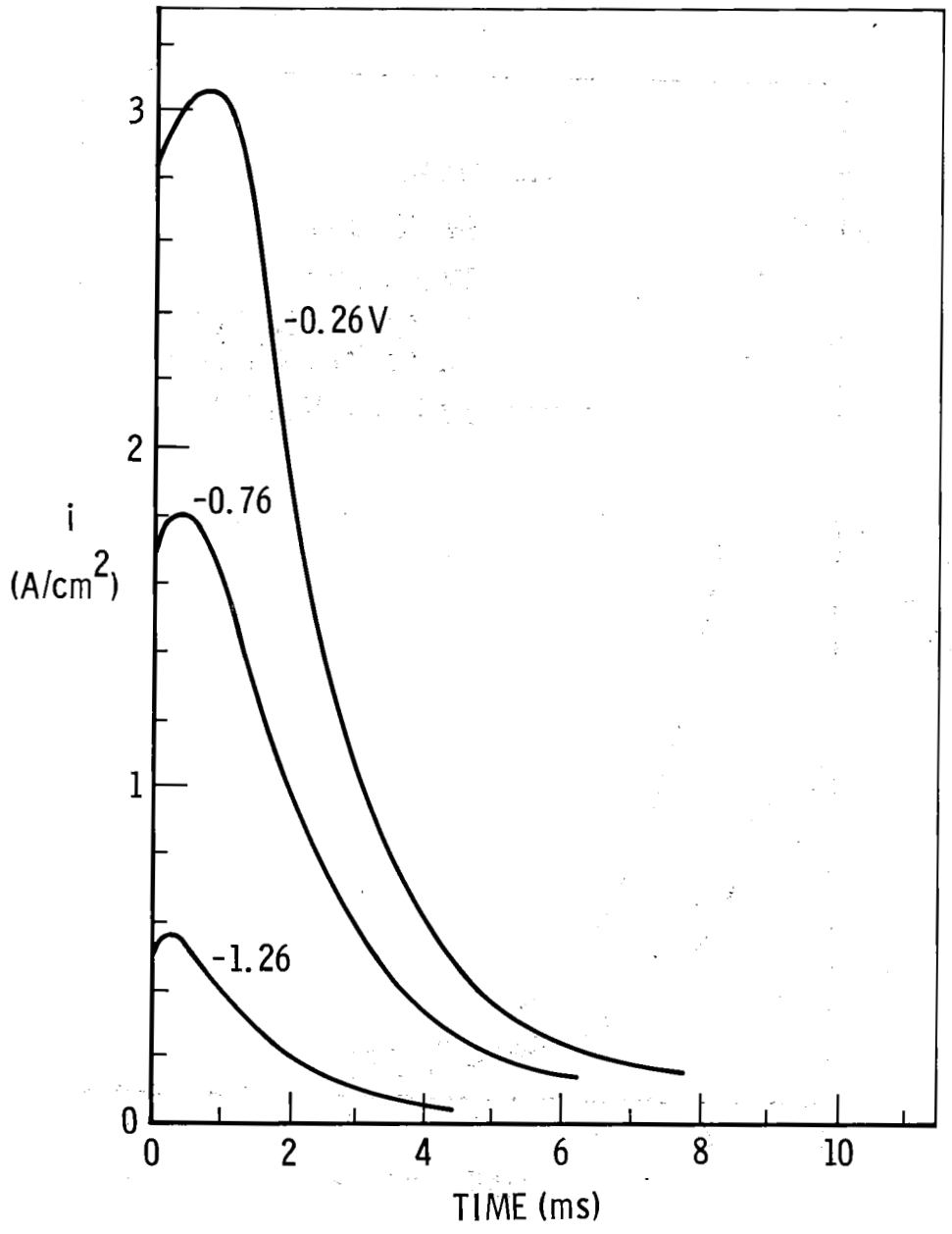


Fig. 11 - Effect of potential on current density-time curves for new surfaces of commercially-pure Ti in 3M KCl + 1M KOH.

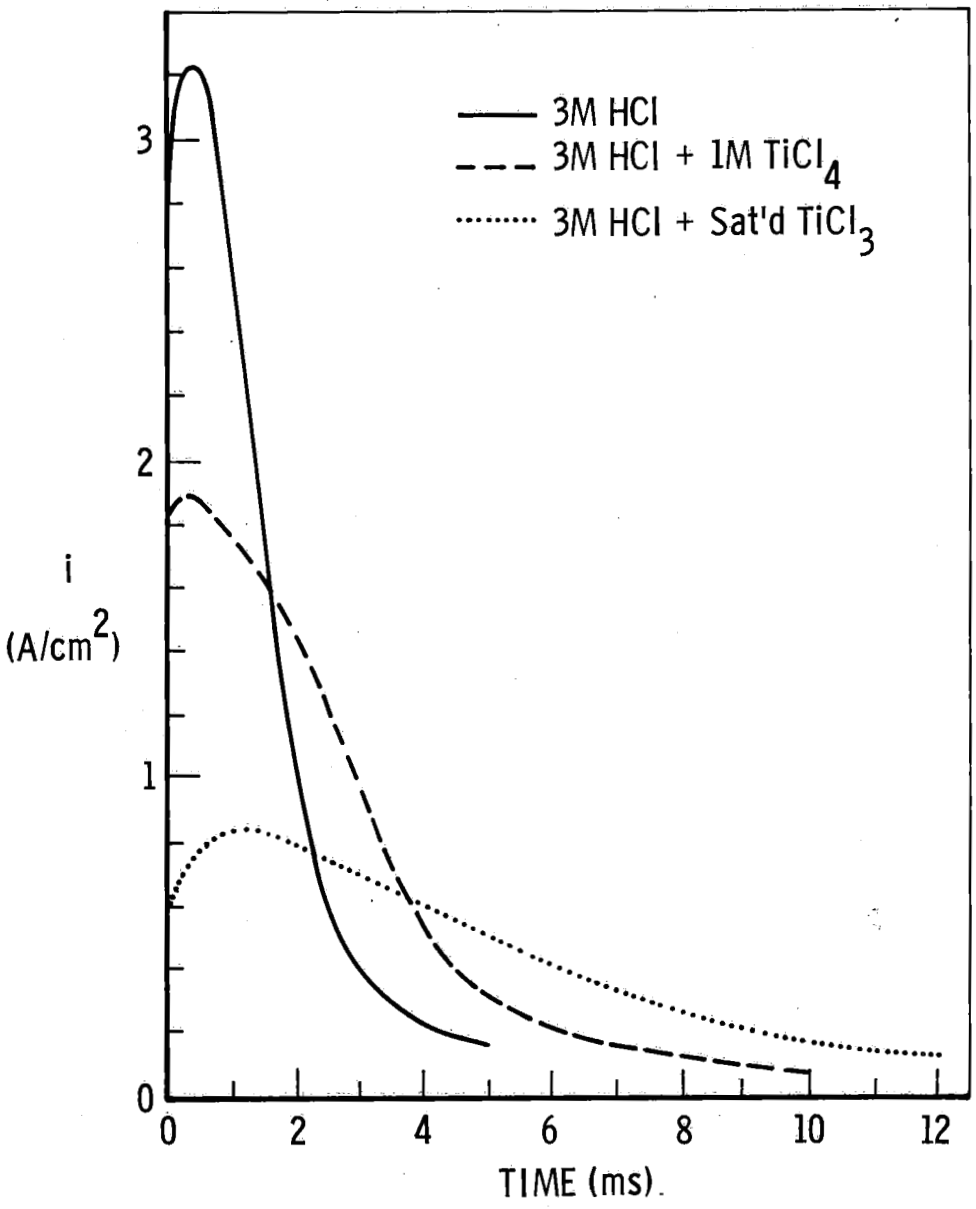


Fig. 12 - Effect of added $TiCl_3$ and $TiCl_4$ on current density-time curves for new surfaces of commercially-pure Ti in 3M HCl at potential of 0.24 V.

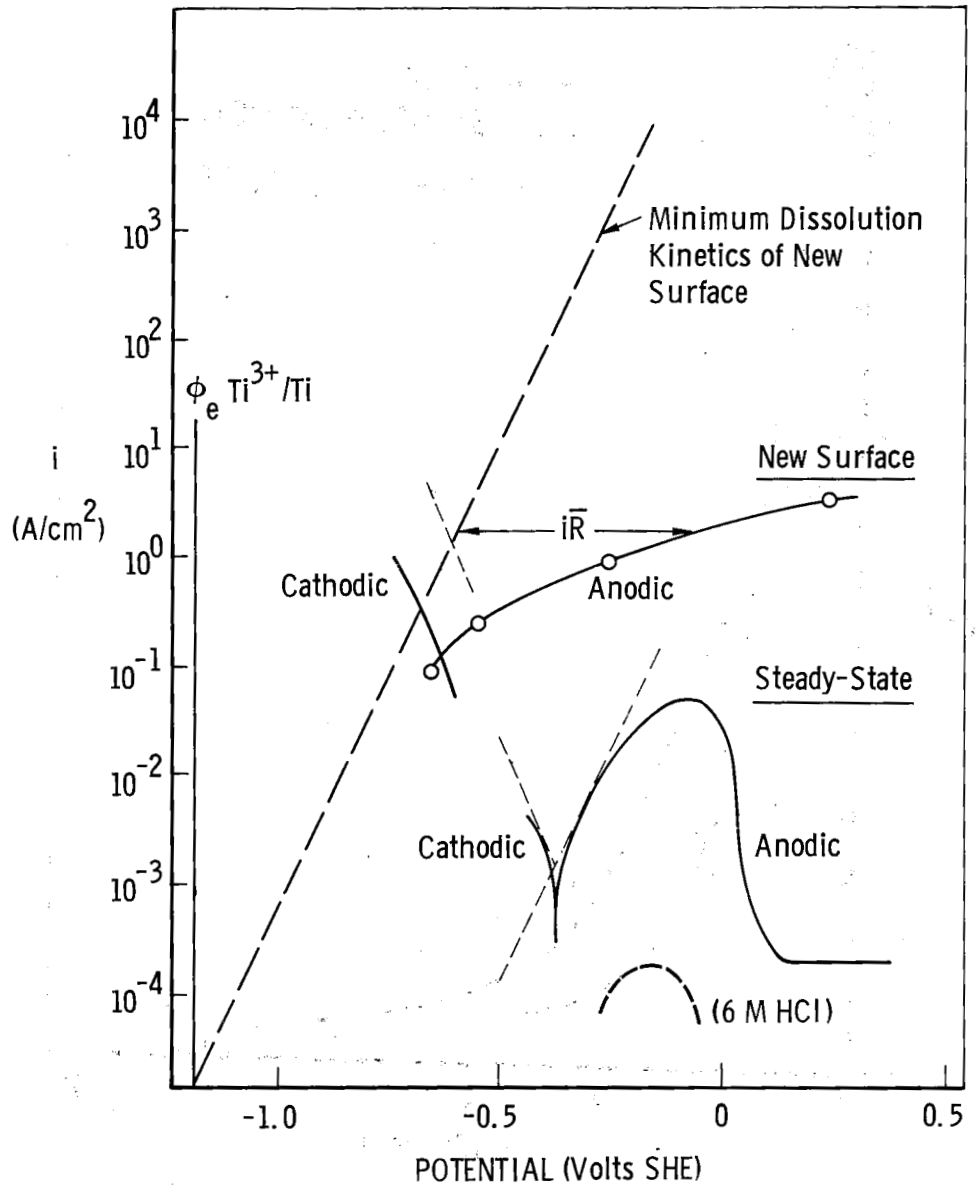


Fig. 13 - Kinetic data for new titanium surface and steady-state kinetics in 12M HCl.

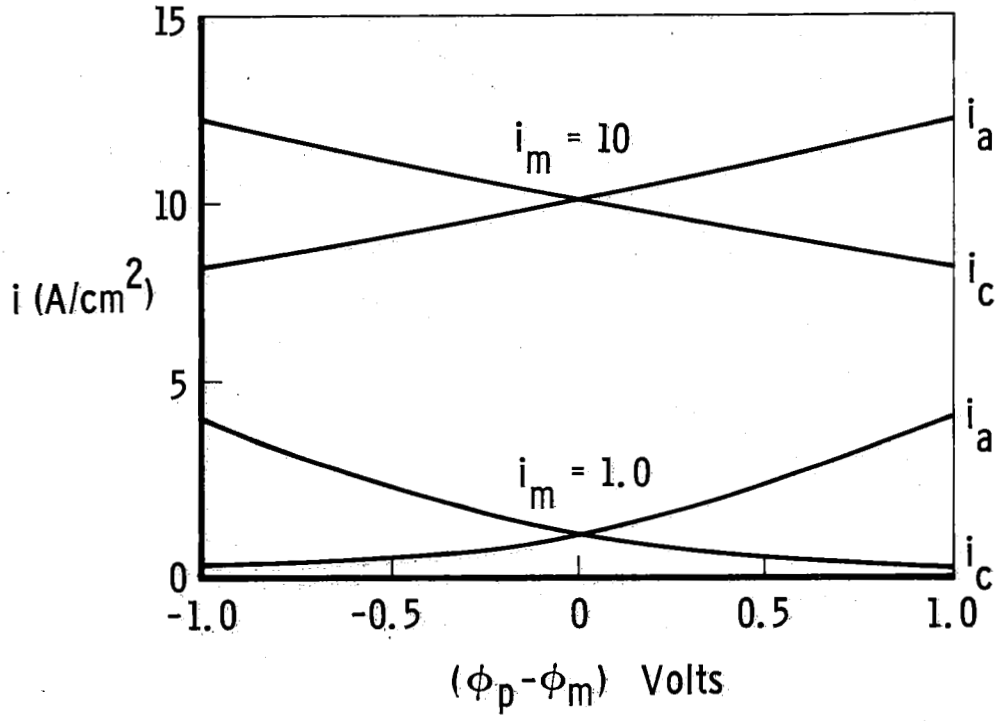


Fig. 14 - Initial actual anodic and cathodic current densities for two values of mixed-potential current density.

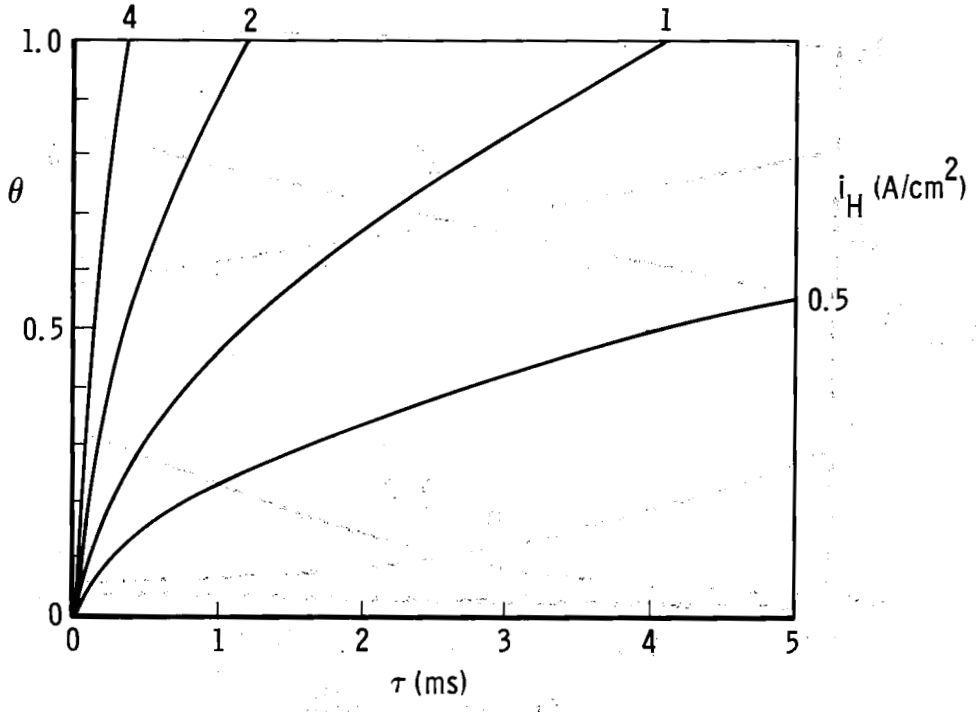


Fig. 15 - Hydride coverage as a function of time for simultaneous diffusion into metal; current density parameter.

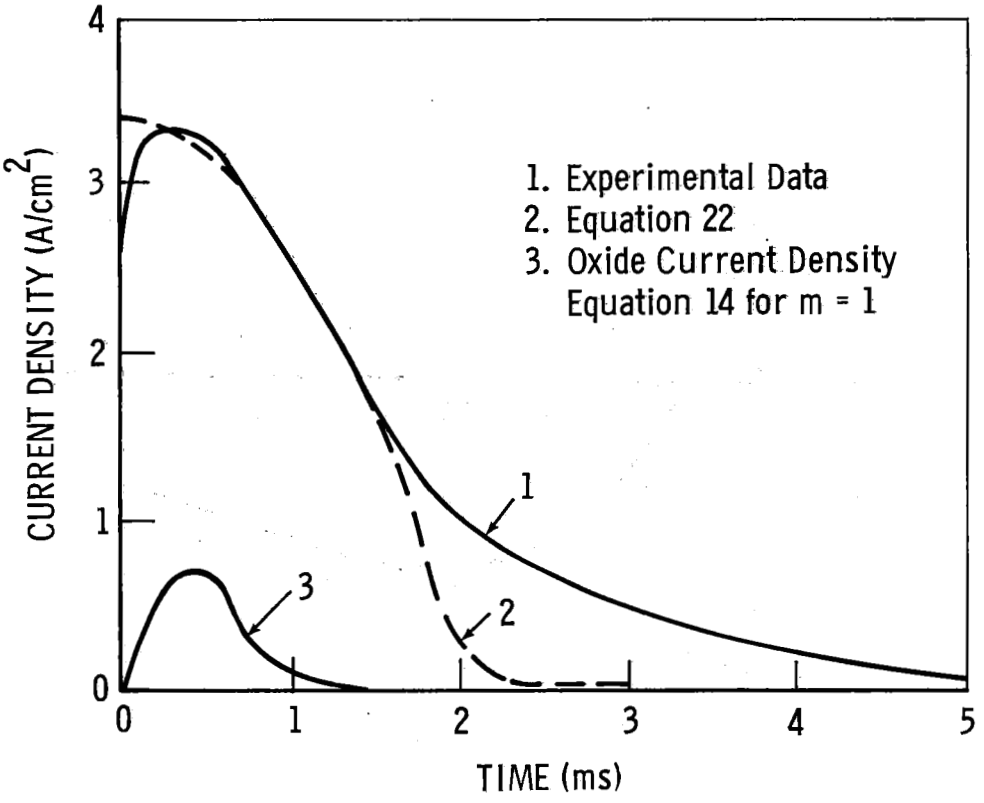


Fig. 16 - Comparison of equation with experimental data for fracture of titanium in 3M HCl at a potential of 0.24 V.

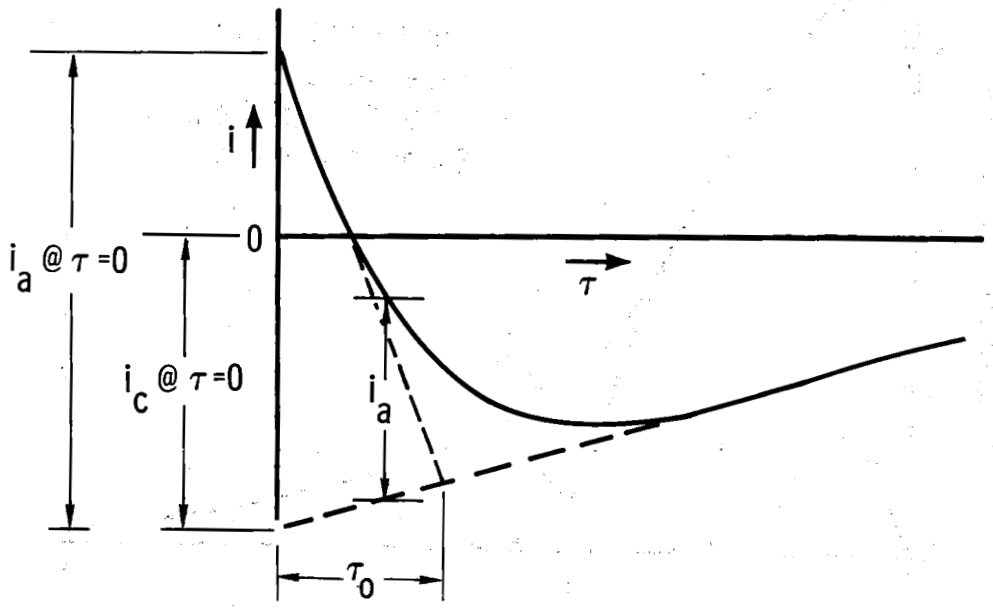


Fig. 17 - Data for fracture of Ti:8-1-1 in 12M HCl at -0.66 V and definition of $i_c$ @ $\tau = 0$, $i_a$ and $\tau_o$ on expanded scale.

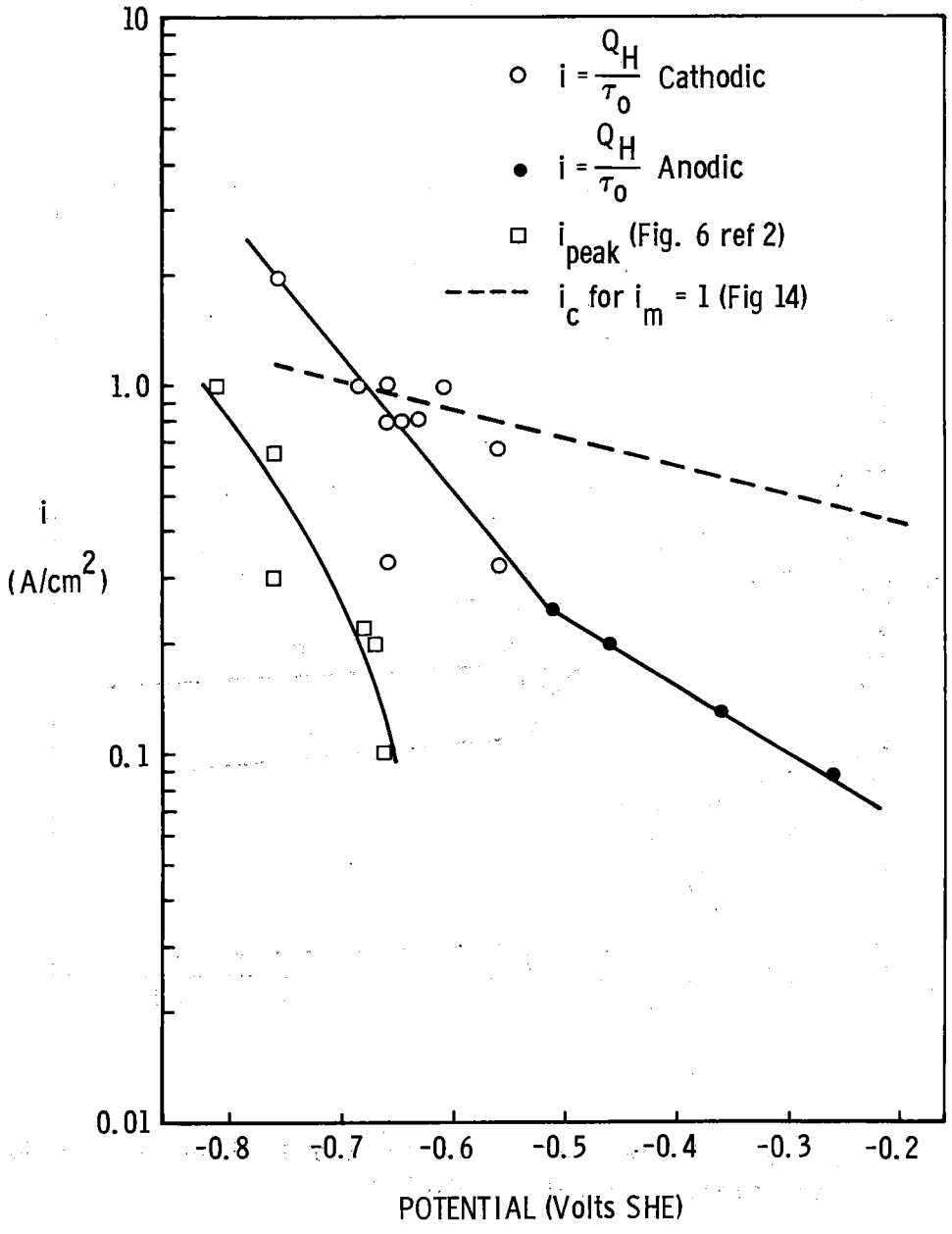


Fig. 18 - Comparison of $Q_H/\tau_o$ to cathodic current densities.

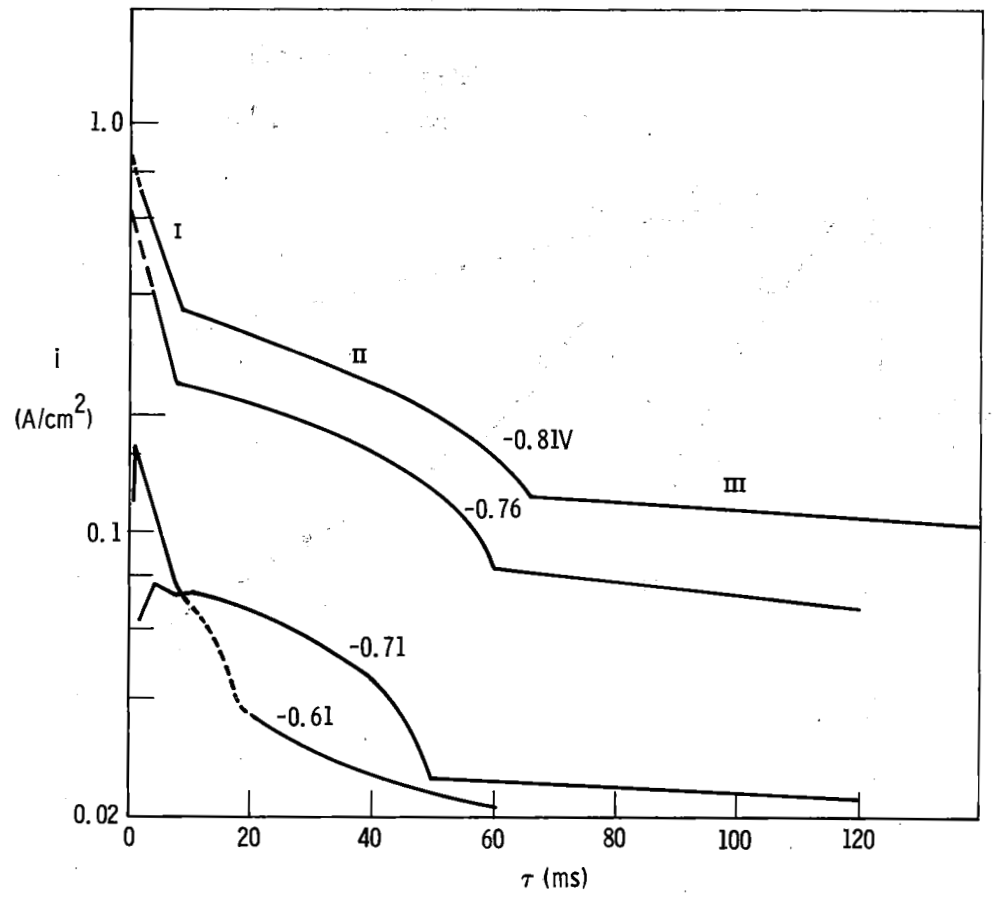


Fig. 19 - Decay of cathodic current density for Ti:8-1-1 in 12M HCl at potentials of -0.81 to -0.61 V.

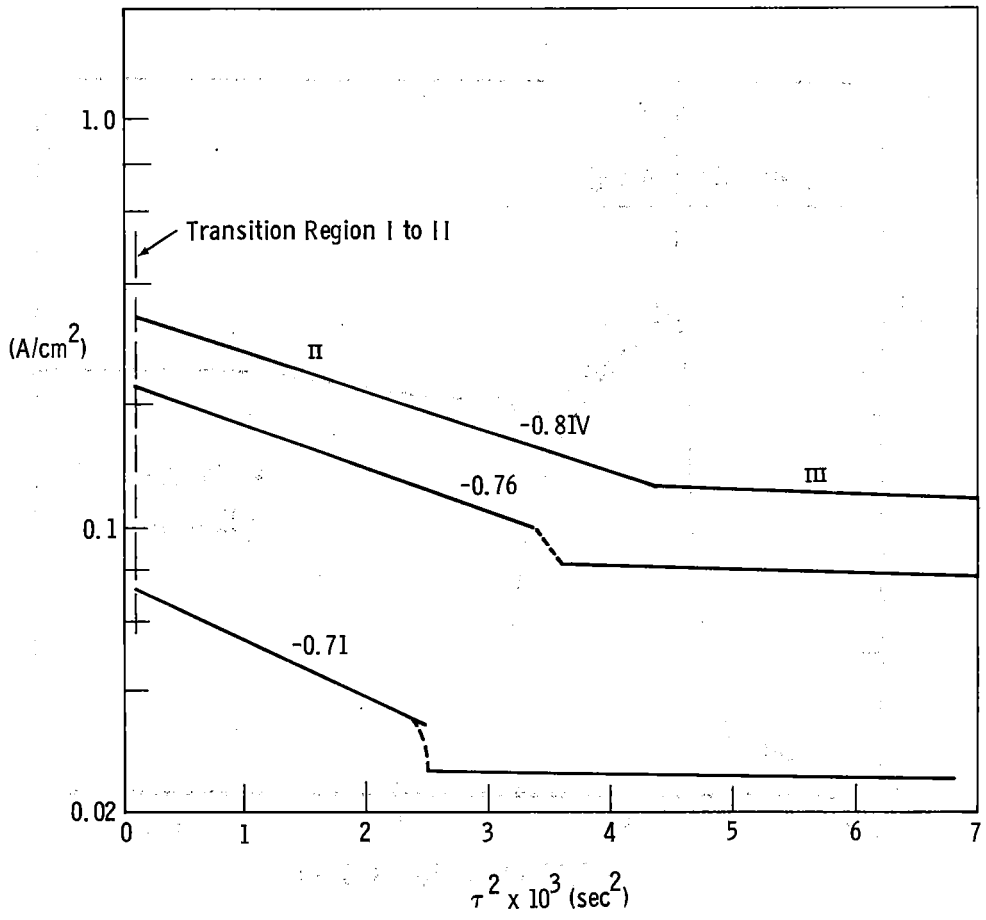


Fig. 20 - Replot of region II and III data from Fig. 19 vs $\tau^2$.

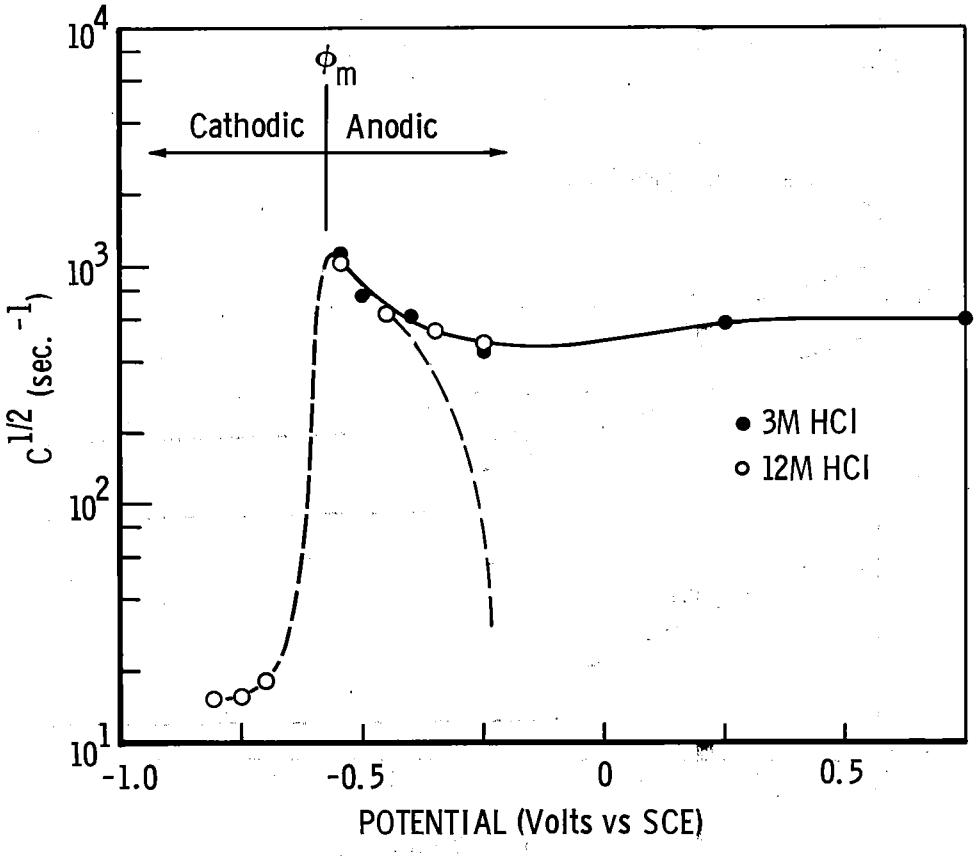


Fig. 21 - Tafel plot of $C^{\frac{1}{2}}$.